



Technische Universität München
Fakultät für Physik

Technische Universität München
Fakultät für Elektrotechnik und Informationstechnik
Lehrstuhl für Nanoelektronik
Prof. Paolo Lugli, Ph.D.

Position sensing using a fiber-optic Fabry-Pérot interferometer

Klaus Thurner

Vollständiger Abdruck der von der Fakultät für Physik der Technischen Universität München zur Erlangung des akademischen Grades eines

Doktors der Naturwissenschaften (Dr. rer. nat.)

genehmigten Dissertation.

Vorsitzende: Prof. Dr. Nora Brambilla

Prüfer der Dissertation:

1. Prof. Paolo Lugli, Ph.D.
2. Prof. Dr. Khaled Karrai

Die Dissertation wurde am 21.06.2016 bei der Technischen Universität München eingereicht und durch die Fakultät für Physik am 25.01.2018 angenommen.

Contents

Contents	i
1 Introduction	3
1.1 Distinction from existing interferometers	5
1.2 Distinction from linear scales	6
1.3 Scope of the thesis	8
2 Theory	11
2.1 Electromagnetic waves	11
2.2 Two beam interference	12
2.3 Fiber optics	16
2.4 Quadrature detection	17
2.4.1 Principles of Lock-in Detection	19
2.4.2 Demodulation schemes	21
2.4.3 Corrections for long cavities	23
2.4.3.1 Phase delay	23
2.4.3.2 Interference of the wavelength modulation frequency	24
2.4.3.3 Modulation depth	26
2.5 Reflectivity of the fiber-coupled Fabry-Pérot cavity	26
2.5.1 Calculation of the Fabry-Pérot formula	27
2.5.2 Interference intensities in relation to the reflectivity	31
2.5.3 Interference intensities in relation to the coupling efficiency . .	32
2.5.4 Nonlinearities	33
2.6 Summary	34
3 Measuring system	37
3.1 Sensor specification	38
3.2 Principle of operation	39

CONTENTS

3.2.1	Fiber optics	43
3.2.1.1	Laser	44
3.2.1.2	Detector	45
3.2.1.3	Noise sources	45
3.2.2	Interferometer initialization	47
3.2.3	Wavelength stabilization	48
3.3	Real-time interfacing	50
3.3.1	Serial interface (HSSL)	51
3.3.2	Quadrature interface (A-quad-B)	52
3.3.3	Analog Sine/Cosine	53
3.4	Measuring systems	53
3.4.1	attoFPSensor	53
3.4.2	FPS3010	54
3.4.3	IDS3010	56
3.5	System performance	57
3.5.1	Stability	57
3.5.2	Phase dependency of the position noise	58
3.5.3	Bandwidth dependence of the position noise	58
3.5.4	Noise spectral density	59
3.5.5	Fiber circuit noise	60
3.6	Nonlinearities	61
3.7	Velocity and vibration tracking	62
3.8	Ambient environment compensation	64
3.8.1	Weather station	66
3.8.2	Refractometer	70
3.9	Reference cavities	71
3.9.1	Low temperature cavity	72
3.9.2	Room temperature cavity	74
3.10	Summary	75
4	Sensor head configurations	77
4.1	Instrumentation	78
4.2	Coupling efficiency simulation	81
4.3	Position sensing with a bare fiber	82

CONTENTS

4.4	Towards increasing the measurement range	84
4.5	Position sensing using a confocal double pass arrangement	87
4.5.1	Measurements and simulations	90
4.5.2	Nonlinearities	92
4.5.2.1	Geometrical nonlinearities	92
4.5.2.2	Double modulation	94
4.6	Position sensing with focusing optics	94
4.6.1	Target with low reflectivity	95
4.6.2	Target with high reflectivity	97
4.6.3	Target with curved surface	99
4.7	Summary	100
5	Absolute distance sensing	103
5.1	Principle of measuring absolute distances	104
5.1.1	Synthetic Wavelength Approach	104
5.1.1.1	Frequency tuning interferometry	105
5.1.1.2	Synthetic wavelength	106
5.1.1.3	Fringe number assignment	107
5.1.2	Combinatory Fringe Number Approach	108
5.1.2.1	Determining fractional phases	108
5.1.2.2	Laser wavelength sweep	109
5.1.2.3	Computation of a coarse absolute distance	109
5.1.2.4	Computation of an accurate absolute distance	110
5.1.2.5	Consistency check	112
5.2	Instrumentation	113
5.2.1	Quadrature detection	114
5.2.2	Correction of periodic nonlinearities	118
5.2.3	Wavelength control	120
5.3	Computation of absolute distance	123
5.4	Summary	127
6	Applications	129
6.1	Low temperature applications	129
6.2	Differential interferometer	132
6.2.1	Vibrometer setup	132

CONTENTS

6.2.2	Long range measurements	134
6.2.3	Short range measurements	135
7	Conclusion and Outlook	139
8	List of publications	143
	Bibliography	145

Abstract

This work presents a novel fiber-optic interferometric displacement sensor which is based on a low-finesse Fabry-Pérot cavity. The Fabry-Pérot cavity is formed between the cleaved, semitransparent end face of a single mode fiber and a movable target. The sensor uses a quadrature detection scheme based on the wavelength modulation of a distributed feedback laser operating in the telecom wavelength range around 1550 nm. The use of telecom wavelength parts makes the interferometer cost-efficient and enables its miniaturization. The sensor enables measuring position changes over a range of 1 m with a digital resolution of 1 pm and tracks velocities up to 2 m/s. It is well suited to work in extreme environments such as ultrahigh vacuum, cryogenic temperatures, or high magnetic fields and supports multichannel applications. The interferometer achieves a position repeatability of $3\sigma = 0.45$ nm and an accuracy of up to 1 nm. For operation in ambient conditions, this work provides equations for the correction of the refractive index of air using a weather station and a refractometer. A position uncertainty of 0.3 ppm was demonstrated using a weather station.

The interferometer is suitable for displacement sensing in a wide range of applications by using different configurations of the low-finesse Fabry-Pérot sensing cavity. Depending on the configuration of the cavity, the interferometer allows measuring on a variety of target materials which differ in their reflectivity and surface roughness. Different configurations of the cavity, which differ in the beam shape and the target material, are investigated with respect to the possible working ranges and angular alignment tolerances using the interference contrast, which is a measure for the signal quality. The use of a confocal double pass arrangement, which is formed when using a collimated beam and a high reflective mirror, enables a measurement range of 100 mm with a large angular alignment tolerance of up to $\pm 1^\circ$. In contrast, using a focused beam allows measuring also on low reflective or rough targets, but with reduced measurement range. In order to predict the optical response of arbitrary configurations of the Fabry-Pérot interferometer, a simulation method based on the

Airy formula and the fiber optic coupling efficiency is introduced.

Furthermore, a new method for absolute distance sensing in the sub-meter range by two laser optical interferometry is established. A particularity of this technique is that a target distance is determined in absolute and is no longer limited to within an ambiguity range affecting usually multiple wavelength interferometers. The ambiguity of the single wavelength interferometer was eliminated by combining frequency tuning interferometry with dual wavelength interferometry. The technique uses two diode lasers, both operating in the telecom wavelength range. The wavelength difference is chosen to create a 25 μm long periodic beating interferometric pattern allowing a nanometer precise position measurement limited to within an ambiguity range of 25 μm . The ambiguity is then eliminated by scanning one of the wavelengths over a small range (3.4 nm). We measured absolute distances in the sub-meter range and this with just few nanometer repeatability.

1 Introduction

Today's nanopositioning control applications more and more call for position sensors with picometer resolution and an accuracy in the double-digit nanometer range, or even less. Beside these very well known specifications, properties like compactness, robustness, usability, industry scalability, measurement speed or the ability to compensate for environmental influences are gaining increasing importance. There is also an increasing need for position sensors operating in harsh environments like ultra-high vacuum, cryogenic temperatures, high magnetic fields, ionizing radiation, or turbulent air. Technology drivers for sensors compatible with such specifications are synchrotrons, the semiconductor industry for wafer manufacturing and quality control, machine engineering, in particular tool making, for qualification of machine tools and parts, and scanning probe microscopy.

There is a large variety of position and displacement sensors available on the market, including interferometers, linear scale encoders, linear variable differential transformers (LVDT), capacitive and resistive sensors.[1, 2] A coarse overview over measurement range and resolution of these sensors is shown in figure 1.1. Resistive sensors provide only low resolution ($> 1 \mu\text{m}$) and accuracy, but they are suited to work at low temperature and ultra-high vacuum. Capacitive sensors are very limited in the measurement range, which is typically between $10 \mu\text{m}$ to 10mm , but provide a high resolution of typically 2.4nm . LVDTs usually provide a longer measurement range of up to about 500mm and are well suited to work under extreme environments, but the accuracy is only in the order of 10^{-3} . The most common position sensor is probably the linear scale encoder. It provides several meters of measurement range with a resolution down to about 6nm , and this with an accuracy of 5ppm . Among the position sensors, interferometry typically provides the highest resolution, accuracy and the longest measurement range, and is therefore best suited for position control on the nanometer level. Unlike the other sensors, interferometers allow measuring in close vicinity to the measurement object, i.e. on the sample level, thus making the

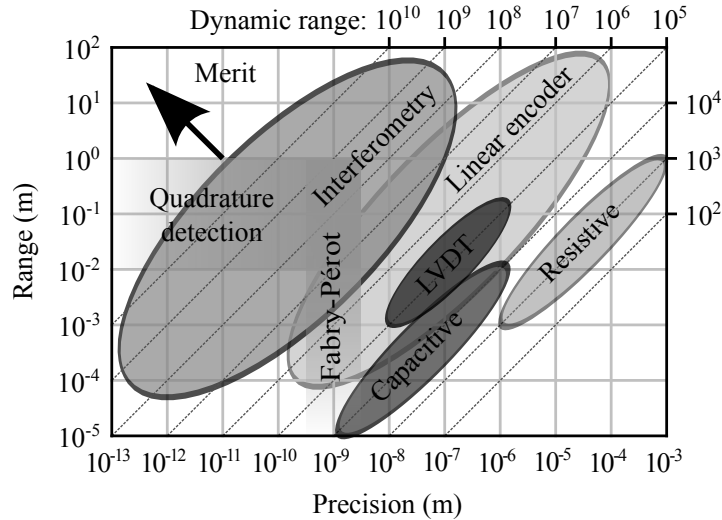


Figure 1.1: Overview over range and precision of different position and displacement sensors. The horizontally and vertically shaded area classifies the presented Fabry-Pérot interferometer which uses a quadrature detection scheme to achieve measurement ranges of up to 1 m.

position readout independent from the moving stage.

However, current interferometric systems imply several limitations. For example, interferometry is exclusively used in calibration processes due to the comparably high costs. The considerably high costs furthermore prevent a real competition with linear encoders, although interferometers are typically easier to integrate into existing setups as they are not bound to a scale. Common interferometers are, so far, often not suited for operation in harsh environments, are limited in their measurement bandwidth and suffer from large sensor heads. They also do not provide the possibility to determine the absolute position of the target reflector, a feature which is already available in linear scale encoders.

In the course of this work, a novel interferometer has been developed based on the previous attocube patents [3, 4] and its performance was characterized. This interferometer is able to overcome the limitations of today's laser interferometers by taking an approach that differs from existing interferometer technique. The approach makes use of the advantages of a fiber-optic Fabry-Pérot interferometer operating in the telecom wavelength range. In particular, short wavelengths (S-band, 1460 to 1530 nm) and conventional wavelengths (C-band, 1530 to 1565 nm) are used in the present approach. The use of components supporting the telecom wavelength range

enables both the miniaturization and cost reduction of the interferometer, thus allowing to compete with the linear scale encoder technique in order to satisfy the current most demanding nanopositioning needs. A huge advantage of the presented interferometer manifests itself in its compatibility with extreme environments like ultra-high vacuum, cryogenic temperatures or high magnetic fields, where most of the sensors would fail.

1.1 Distinction from existing interferometers

Most of the commercially available interferometers are based on a Michelson interferometer. This type of interferometer suffers from a number of substantial disadvantages. For clarification, figure 1.2 compares the basic design of the Fabry-Pérot inter-

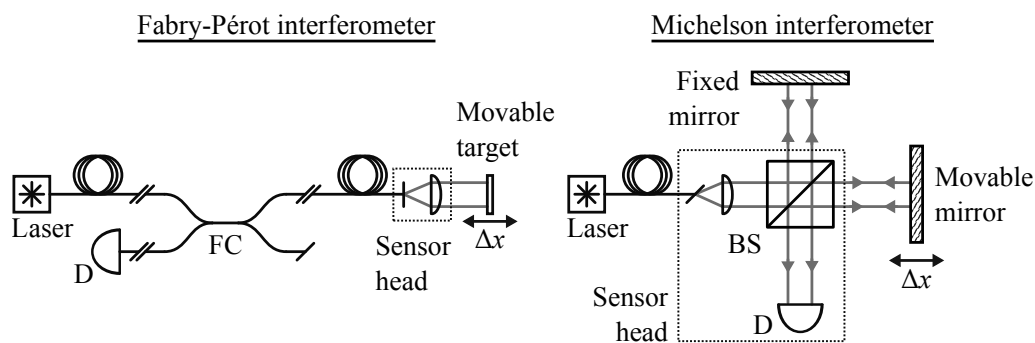


Figure 1.2: Comparison between Fabry-Pérot interferometer (left) and Michelson interferometer (right). Both interferometers comprise a fiber-coupled laser and a photo detector D. In the Michelson interferometer, a beam splitter BS splits the light into a reference beam and a measurement beam. A displacement of the movable mirror in the measurement arm by an amount Δx produces a phase shift between the two beams. In the Fabry-Pérot interferometer, the beam splitter is replaced by a semitransparent reference plane which is formed by the interface between the fiber and air. The light from the laser is routed to the interface via a fiber coupler FC.

ferometer (left) and Michelson interferometer (right). In the Michelson interferometer, the light from a laser is routed to a collimating lens. Then, a beam splitter splits the light into a reference beam and a measurement beam and directs them to the interferometer reference and measurement arm. The light beams are reflected by the mirrors and recombine at the beam splitter. The interference signal is detected at with a photo diode. A displacement of the movable target mirror in the measurement arm by an amount Δx produces a phase shift $\Delta\Phi$ between the two light paths. In

the Fabry-Pérot interferometer, the light from the laser is routed to a fiber coupler where it is split into equal parts. The beam splitter is replaced by a semitransparent reference plane which is formed by the interface between the fiber and air. The light which is routed to the sensor head is partially reflected by this interface and forms the reference beam. The rest of the light is reflected by the movable mirror and recombines with the light of the reference beam. The interference signal is routed through the same fiber coupler and is detected at a remote photo diode.

From a physical point of view, the existing Michelson interferometers are not suited to work under extreme environments such as ultra-high vacuum, cryogenic temperatures, high magnetic fields or ionizing radiation. This is due to the design of the interferometer head, comprising electronic parts which are sensitive to temperature, magnetic field or ionizing radiation. The reference arm might further be sensitive to changes of the environmental conditions, causing thermal position drifts or refractive index changes which limit the accuracy of the position measurement. A mechanical aspect that limits the field of applications of the Michelson interferometer is the large size of the sensor head, which is limited by large optical parts such as beam splitters and wave plates.[5]

Both the size of the sensor head and its robustness against external influences benefit from the use of a Fabry-Pérot interferometer. The reason for this lies in the structural difference of the Fabry-Pérot interferometer. The use of a semi-transparent reference plane makes the reference arm, which is required in the Michelson interferometer, redundant, and the path difference is precisely defined by the distance between reference plane and target.[6] The Fabry-Pérot interferometer is therefore also referred to as common path interferometer.[7] This improves the stability of the interferometer because, firstly, no beam splitters are required, secondly, no drifts can falsify the result from the actual measurement, and thirdly because there are no refractive index changes induced between measurement and reference arm. It further offers the possibility to separate all electronic parts from the experiment because the optical fiber remotely collects the interference signal created at the fiber end face.[6]

1.2 Distinction from linear scales

A special strategic objective of this work is the replacement of linear scales by laser interferometry. Apart from the original idea to create a position sensor for extreme en-

1.2. DISTINCTION FROM LINEAR SCALES

vironments in research applications, favorable feedback from industry encouraged the development of an industrial version of the interferometer (referred to as IDS3010), which has the potential to replace linear scale encoders due to the reasons which are discussed in this section.

The accurate and precise control of positioning stages at the nanometer level counts among the key technologies in precision engineering because it allows the accurate control of production processes over wide ranges, which in turn enables, for example, increasing the density of structures in semiconductor industry or the precision of tools in tool manufacturing. This requires three dimensional position sensing at the sample level at various environmental conditions. In this context it becomes more and more attractive to replace linear scale encoders by laser interferometry. The reasons for these developments are manifold. Firstly, interferometers profit from an intrinsic high accuracy.[2] While the accuracy of linear scale encoders is typically in the order of 5 ppm, the accuracy of the IDS3010 is 50 ppb in a vacuum and 0.14 ppm at ambient conditions. Similarly, the resolution of interferometers surpasses that of linear encoders. This is due to the different pitch length of both techniques. In linear scales encoders, the pitch length is given by the pitch of the scale grating, which is typically in the order of 20 μm . The pitch of an interferometer is naturally given by half of the laser wavelength, which is 0.8 μm in the present interferometer. Interferometry is therefore also referred to as primary reference measurement procedure, because it does not rely on the relation to a measurement standard.[8] Interferometers moreover allow position sensing at the sample level. This provides information about the real movement of the sample and about target vibrations, which are often invisible for linear scale encoders. The simultaneous measurement of three channels in the IDS3010 moreover gives access to erratic pitch and yaw movements of the stage. The type of interferometer presented here is also ultra compact (sensor heads with a diameter down to 1 mm are already possible), easy to integrate, and there is also no need for calibration since the interferometric measurement procedure counts among the primary reference measurement procedures.[8] Linear scale encoders, however, are rather bulky and require much more time for construction engineering in order to integrate them into a setup. Very often, these encoders have to be calibrated by means of an independent interferometric measurement in order to achieve the required accuracy. In this calibration process, look-up tables are created and applied to the measured values of the encoder. Linear scale encoders also suffer from a tedious alignment pro-

cess which takes longer the higher the requirements for the accuracy are. Another difference is the sensitivity to different environments. While the presented interferometer is compatible with almost all extreme environments, the operation of linear scales is restricted to measurements at ambient conditions. However, in interferometry, air turbulence and spatial variations of the refractive index can degrade the measurement accuracy, while linear scale encoders are insensitive to the composition of air. The only problem they encounter in air are temperature changes which lead to a thermal expansion of the linear scale and consequently to a degradation of the measurement accuracy. Getting rid of this disadvantage is the biggest challenge for industrial interferometry in these days. A possible solution approach will certainly rely on the interferometric measurement of the refractive index, and this along the actual measurement beam.

1.3 Scope of the thesis

This thesis describes a novel low-finesse Fabry-Pérot miniature fiber based interferometer for displacement measurements.

The theoretical principles of Fabry-Pérot interferometry are presented in chapter 2. It considers the question of whether this type of interferometer is a Doppler interferometer. The question seems to be trivial, but this chapter will show that this is not the case and clears up with a common misunderstanding. Furthermore, two different quadrature detection schemes and the associated limitations with respect to accuracy and measurement range will be presented. This chapter further provides formulas allowing to predict the interference intensities created in the fiber. Partial results of this chapter have been published in advance in the journal publication [9].

In chapter 3, the interferometer setup and its operational principle will be described and the interferometer performance will be demonstrated experimentally. The chapter also comprises details about the real-time interface which allows transmitting measurement values of the position and about the environmental compensation of the refractive index, which limits the measurement accuracy in air. Partial results of this chapter have been published in advance in the journal publication [9].

The proper combination of sensor head design and target reflector can cover a variety of different position tracking applications. Depending on the design, the sensor head can provide different beam geometries, in particular collimated and convergent

laser beams. In the end, the proper beam geometry depends on the target reflectivity and on the surface morphology. In chapter 4, different configurations of the Fabry-Pérot cavity are investigated and characterized with respect to their ability to increase the measurement range of the interferometer and to their tolerance against angular misalignment. In order to predict the optical response of arbitrary configurations of the Fabry-Pérot interferometer, a simulation method based on the Airy formula and the fiber optic coupling efficiency is introduced and evaluated. Partial results of this chapter have been published in advance in the journal publication [10].

An interruption during the laser interferometer displacement measurement leads to the loss of position in case that the target drifts away more than half of the pitch length. In many instances, the loss of position and displacement information is very detrimental, in particular in systems where accessibility is much reduced and fine alignment is critical. Therefore, a method for absolute distance sensing by two laser optical interferometry was developed, which is described in chapter 5. A particularity of this technique is that a target distance is determined in absolute and is no longer limited to within an ambiguity range affecting usually multiple wavelength interferometers. The heart of the system consists of two tunable diode lasers, both operating in the telecom wavelength range. Partial results of this chapter have been published in advance in the journal publication [11] and in the patent application [12].

Different applications of the interferometer are presented in chapter 6. In particular, the operation of the interferometer at cryogenic temperatures is demonstrated. Furthermore, the differential measurement of the expansion of a piezoelectric stack is demonstrated. Partial results of this chapter have been published in advance in the journal publication [9].

2 Theory

This chapter provides a theoretical description of the interference signal created at the fiber end face, which is fundamental for the understanding of the whole sensor. It helps understanding the fundamental limitations of the sensor and allows building models which can predict the performance of the sensor without the need for testing.

As there is still confusion about how to take into account Doppler shift corrections in the interference signal of a moving target, the chapter begins with the derivation of the fundamental wave equation needed for the understanding of how these corrections are applied correctly to the two beam interference. It further provides some fundamentals on fiber optics, comprising the derivation of the numerical aperture which is relevant for fiber coupling efficiency calculations. As the pure interference signal provides no information about the direction of displacement and only limited information about the amount of displacement, a special quadrature detection scheme will be introduced and characterized with respect to its limitations. The end of this chapter deals with the reflectivity of the fiber coupled Fabry-Pérot cavity, contrary to the two beam interference in the Michelson interferometer, and provides a formula for the interference intensity as a function of the phase angle.

2.1 Electromagnetic waves

The interference pattern created in an interferometer is described by the superposition of plane electromagnetic waves. These plane waves are solutions of the fundamental Maxwell equations in an uniform optical medium with homogenous permeability $\mu = \mu_r \mu_0$ and permittivity $\epsilon = \epsilon_r \epsilon_0$. The vacuum permeability μ_0 and vacuum permittivity ϵ_0 are linked to the the speed of light c_0 in a vacuum according to

$$c_0 = \frac{1}{\sqrt{\epsilon_0 \mu_0}}. \quad (2.1)$$

The refractive index n of electromagnetic radiation in a medium is linked to the relative permeability μ_r and relative permittivity ϵ_r by

$$n = \sqrt{\epsilon_r \mu_r}. \quad (2.2)$$

The Maxwell equations[13, 14, 15] in a charge and current free medium are given by

$$\nabla \cdot \mathbf{E} = 0 \quad \nabla \times \mathbf{E} = -\frac{\partial \mathbf{B}}{\partial t} \quad (2.3)$$

$$\nabla \cdot \mathbf{B} = 0 \quad \nabla \times \mathbf{B} = \epsilon\mu \frac{\partial \mathbf{E}}{\partial t}, \quad (2.4)$$

where t is the time, \mathbf{E} is the electric field vector, and \mathbf{B} is the magnetic field vector. By further applying the curl operator ($\nabla \times$) to the curl equations yields the wave equation for \mathbf{E} and \mathbf{B} ,

$$\nabla^2 \mathbf{B} - \epsilon\mu \frac{\partial^2 \mathbf{B}}{\partial t^2} = 0 \quad (2.5)$$

$$\nabla^2 \mathbf{E} - \epsilon\mu \frac{\partial^2 \mathbf{E}}{\partial t^2} = 0. \quad (2.6)$$

The solution of these equations are plane waves of the form

$$\mathbf{E}(\mathbf{r}, t) = \mathbf{A}_1 e^{i(\mathbf{k}\mathbf{r} - \omega t)} + \mathbf{A}_2 e^{i(-\mathbf{k}\mathbf{r} - \omega t)}, \quad (2.7)$$

where \mathbf{k} is the wave vector, \mathbf{r} is the position vector and ω is the angular frequency of the electric field. In a more generalized approach, the wave functions are of the form

$$\nabla^2 \psi - \frac{n^2}{c_0^2} \frac{\partial^2 \psi}{\partial t^2} = 0, \quad (2.8)$$

and the solutions are the functions [16]

$$\psi(\mathbf{r}, t) = f_-(\mathbf{k} \cdot \mathbf{r} - \omega t) + f_+(\mathbf{k} \cdot \mathbf{r} + \omega t), \quad (2.9)$$

which can be rewritten as $f(\xi) = f(x - ct)$ in one dimension.

2.2 Two beam interference

In an optical interferometer, such as the Michelson interferometer shown in figure 2.1, a monochromatic light beam is split in two channels, a reference beam with field amplitude E_r , and a sample beam of field amplitude E_s . The sample beam is made

2.2. TWO BEAM INTERFERENCE

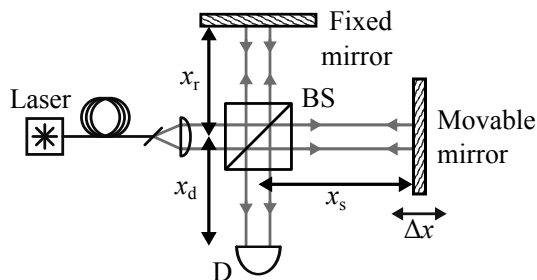


Figure 2.1: Two beam interference illustrated by means of the Michelson interferometer. In the Michelson interferometer, a beam splitter (BS) splits the light into a reference beam E_r and a sample beam E_s and directs the beams to the interferometer reference and sample arm with a length of x_r and x_s , respectively. After being reflected, both beams recombine at the BS and hit the detector D after a distance x_d .

to experience an optical path x_s that differs in length from that of the reference beam x_r . All optical interferometers (Michelson, Mach-Zehnder, Sagnac, Lloyd, Fizeau, Fabry-Pérot, Nomarski, Fresnel, Zernike, ...) are arranged in such a way that both the reference and sample beams are recombined and made to beat at the location of a photo detector.[17] At the location of the detector $x = x_d$, which is assumed to be fixed in the laboratory frame, the total field is given as

$$E_s + E_r = A_s \exp(ik_s(x_d + x_s) - i\omega_s t) + A_r \exp(ik_r(x_d + x_r) - i\omega_r t), \quad (2.10)$$

assuming a most general situation for which the wave vector k_s and cyclic frequency ω_s returning from the sample channel might differ from the wave vector k_r and cyclic frequency ω_r of the reference channel. This is in principle possible in the specific situation in which the sample beam is reflecting off a moving target. In such a situation the sample beam undergoes a Doppler shift both in field frequency as well as in wave vector. The power generated by the interfering waves at the photo-detector is proportional to the square modulus of the sum of the fields, which is

$$A_r^2 + A_s^2 + 2A_r A_s \cos\{(k_r x_r - k_s x_s) - (\omega_r - \omega_s)t\}. \quad (2.11)$$

A more convenient form is expressed as

$$I(x, t) = (1 + C \cos \Phi) I_0/2, \quad (2.12)$$

in which

$$C = \frac{I_{\max} - I_{\min}}{I_{\max} + I_{\min}} \quad (2.13)$$

is the contrast of the interference given by the maxima and minima of the measured intensity of fringes, I_{\min} and I_{\max} , which are related to the middle intensity $I_0/2$ by

$$I_0 = I_{\max} + I_{\min} = 2(A_1^2 + A_2^2). \quad (2.14)$$

Φ is the interference phase

$$\Phi = (k_r x_r - k_s x_s) - (\omega_r - \omega_s)t. \quad (2.15)$$

The phase is in fact the most relevant quantity resulting from interferometry since it holds all information about the sample beam in relation to the reference beam. In the obvious situation for which both the reference beam and sample beam have $k_s = k_r = k$ and $\omega_s = \omega_r = \omega$, the phase is simply given by $\Phi = k(x_r - x_s) = -kx$ and is essentially informative of the optical path difference x which makes interferometry so attractive in optical distance sensing.

In the case of a constantly moving target, Doppler shift corrections must be taken into account. This often creates difficulties which are addressed in the following. When the sample beam is reflected off a moving target, the optical path difference $x(t)$ becomes a function of time and it would be tempting to use simply the expression derived above, namely $\Phi(t) = kx(t)$ in order to extract $x(t)$ from the measured phase. In the particular case of a constant velocity displacement of the target, the path difference increases as $x(t) = 2vt$ and, according to the expression of Φ above, the phase would vary as $\Phi(t) = 2kvt$. This is indeed the time dependency which is actually measured and verified in the experiment and the discussion could stop here. However, in displacement sensing the reference beam is Doppler shifted because the target is moving at finite velocity and from this point of view corrections should be in principle considered. For illustration, the case of a constant velocity displacement v of the target is considered, where the sample beam coming back to the detector is red shifted (or blue shifted) such that [13]

$$k_s = (1 - 2v/c)k_r \quad \text{and} \quad \omega_s = (1 - 2v/c)\omega_r. \quad (2.16)$$

At the location x_d of the detector both the reference and sample beam are beating with a phase

$$\Phi = kx + 2kvt - 2k(x_d + x)(v/c), \quad (2.17)$$

where the relations $x = x_r - x_s$ and $\omega/c = k$ were used. At this point one would be tempted to replace x with the time varying expression $x(t) = 2vt$. It will be shown in

2.2. TWO BEAM INTERFERENCE

the following that this is strictly not allowed. If one would continue nevertheless, one would get from the equation above the time dependency $\Phi(t) = 4kvt - 2k(x_d + vt)v/c$. This expression is in stark contradiction with the experimental observation which shows in fact that the phase varies as $2kvt$. [18] In summary, ignoring the Doppler shift corrections would lead to the correct expression for the temporal behavior of the phase. Instead, including the Doppler corrections in the way shown above leads to an absurdly incorrect description of reality.

The mistake is based on a misuse of equation 2.17 above at the very moment it was attempted to introduce a time dependency to the path difference x . The expression of the plane wave field in equation 2.10 is only a solution of the Maxwell equations if there is a strict separation between the temporal and spatial components x and t , so the path difference cannot be made to be a function of time in this formalism. This becomes clear when considering that both plane waves E_r and E_s are solutions of the wave equation

$$\nabla^2 \psi - \frac{n^2}{c_0^2} \frac{\partial^2 \psi}{\partial t^2} = 0, \quad (2.18)$$

which is derived from the Maxwell equations. The solutions of the wave equation are of the form $f(\xi) = f(x - ct)$. When replacing x by $x(t)$, f is no longer a solution of the wave equation. This can be easily seen when building the partial derivations of f according to

$$\frac{\partial^2 f}{\partial x^2} = \partial_\xi^2 f \quad \text{and} \quad \frac{\partial^2 f}{\partial t^2} = c^2 \partial_\xi^2 f \quad (2.19)$$

and inputting them into the wave equation 2.18, resulting in

$$\begin{aligned} \frac{\partial^2 f(x - ct)}{\partial t^2} - \frac{1}{c^2} \frac{\partial^2 f(x - ct)}{\partial t^2} &= \\ = \partial_\xi^2 f(x - ct) - \frac{1}{c^2} c^2 \partial_\xi^2 f(x - ct) &= 0. \end{aligned} \quad (2.20)$$

Replacing x by $x(t)$ obviously does not fulfill this equation. Plane waves of the form $E(x(t), t)$ consequently are not solutions of the wave equation, meaning that the assumption $x = x(t)$ was inadmissible. However, equation 2.17 for the phase, derived in the limit of targets moving at constant velocity, is in fact correct when considering that the value of the path difference x is frozen at the moment of the target movement. The time dependency seen in the phase is solely due to the Doppler shift which results in a heterodyne beating between the reference and sample beam with a temporally

periodic frequency of $2kv$, exactly as measured. Equation 2.17 is to be used with the value of x being frozen. It is interesting to note that there is a Doppler correction to be made in the form of a time independent, constant phase shift and that this correction, which is in v/c , depends on the location of the detector x_d . Interferometers with very long distances to the detector introduce a constant shift in the phase during uniform motion of the target. Here, for illustration, the phase shift is 2π when the target displaces at 1 m/s and the optical path distance to the detector is 232 m at telecom wavelength (this is about 150 m of fiber length). An error of a full period can be obtained under such condition compared to a measurement performed at much lower velocity.

2.3 Fiber optics

In a classical approach, the guidance of light in an optical fiber is achieved by total reflection of the light at the boundary between the fiber core and cladding, which differ in their refractive index.[19, 20] Figure 2.2 shows a light ray passing from the

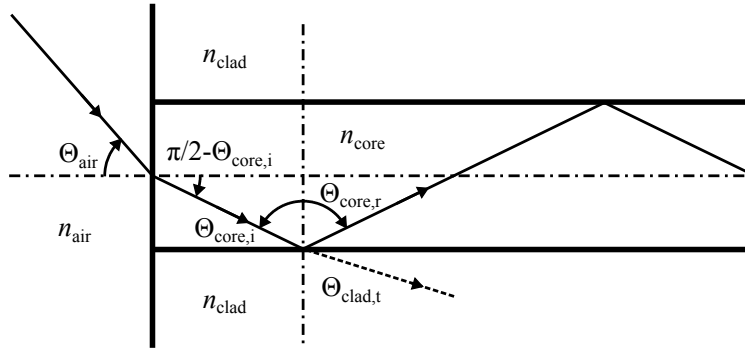


Figure 2.2: Light guidance through an optical fiber consisting of the fiber core with a refractive index n_{core} and the cladding with the refractive index n_{clad} , where $n_{\text{core}} > n_{\text{clad}}$.

fiber core with the refractive index n_{core} at the incidence angle $\Theta_{\text{core},i}$ to the cladding with the refractive index n_{clad} at the transmission angle $\Theta_{\text{clad},t}$, where $n_{\text{core}} > n_{\text{clad}}$. According to Snell's law,

$$n_{\text{clad}} \sin \Theta_{\text{clad},t} = n_{\text{core}} \sin \Theta_{\text{core},i}. \quad (2.21)$$

When increasing the angle $\Theta_{\text{core},r}$, the transmitted light reaches an angle of $\Theta_{\text{clad},t} = 90^\circ$ and $\sin \Theta_{\text{clad},t} = 1$. This angle is referred to as critical angle Θ_c , given by

$$\sin \Theta_c = n_{\text{clad}}/n_{\text{core}}. \quad (2.22)$$

2.4. QUADRATURE DETECTION

In case of an optical single mode fiber (SMF-28), $\Theta_c = \arcsin(n_{\text{clad}}/n_{\text{core}}) = 85.1^\circ$, where $n_{\text{core}} = 1.4682$ and $n_{\text{clad}} = 1.4629$. Above this angle, the light is totally reflected at the reflection angle $\Theta_{\text{core,r}} = \Theta_{\text{core,i}}$. Light rays entering the fiber from the surrounding ambient air with refractive index n_{air} at the angle of incidence Θ_{air} are refracted according to Snell's law,

$$\begin{aligned} n_{\text{air}} \sin \Theta_{\text{air}} &= n_{\text{core}} \sin(\pi/2 - \Theta_{\text{core,i}}) \\ &= n_{\text{core}} \cos(\Theta_{\text{core,i}}) \end{aligned} \quad (2.23)$$

Guidance of the light requires that $\Theta_{\text{core,i}} > \Theta_c$ or

$$\begin{aligned} \sin \Theta_{\text{core,i}} &> \frac{n_{\text{clad}}}{n_{\text{core}}} \\ \cos \Theta_{\text{core,i}} &< \sqrt{1 - \left(\frac{n_{\text{clad}}}{n_{\text{core}}}\right)^2}. \end{aligned} \quad (2.24)$$

Substituting the light guidance criterion of equation 2.24 into equation 2.23 yields an expression for the acceptance angle Θ_{air} ,

$$\sin \Theta_{\text{air}} < \frac{1}{n_{\text{air}}} \sqrt{n_{\text{core}}^2 - n_{\text{clad}}^2} \quad (2.25)$$

Equation 2.25 defines an angular range in which the fiber can accept or emit light and is therefore equal to the numerical aperture (NA) of the fiber, which is defined by

$$\text{NA} = \sqrt{n_{\text{core}}^2 - n_{\text{clad}}^2}, \quad (2.26)$$

where n_{air} is assumed to be 1.

2.4 Quadrature detection

Fabry-Pérot interferometers are usually used to measure small displacements in the nanometer range and are employed, for example, in atomic force microscopes.[21] Information of the position is then obtained by calibrating the detector signal around the maximum slope of the interference pattern.[22] However, this is only possible for displacements not exceeding the range between two interference extrema, $\Delta x < \lambda/4p$, where p denotes the folding order of the cavity. For larger displacements, the amount of displacement and its direction can no longer be determined unambiguously. To overcome this limitation, there are several quadrature detection methods capable of

recovering the phase change $\Delta\Phi$ with constant sensitivity. Quadrature detection, in general, requires two sinusoidal signals which are phase shifted by 90° in order to produce a circular Lissajous figure. The angle of each point in the Lissajous figure represents the phase angle Φ modulo 2π . In this work, the 90° phase shift is produced by locally deriving the original interference signal. This is experimentally achieved by applying a small modulation with the modulation frequency $\Omega = 2\pi f$ to either the target position, denoted as modulated position δx , or the laser wavelength, denoted as modulated wavelength $\delta\lambda = -\delta k\lambda^2/2\pi$. Both effects result in a local variation of the interference intensity according to

$$\delta I = -I_0 C p n \sin(\Phi)(k\delta x + x\delta k), \quad (2.27)$$

where $k = 2\pi/\lambda$ is the wave number of the laser light and $\Phi = 2kpnx$ is the interference phase already considering the refractive index n . This leads to a superposition of the interference signal with the modulation according to

$$I(\Phi, t) = \frac{I_0}{2} + \frac{I_0}{2} C \cos(\Phi + \delta\Phi \sin \Omega t), \quad (2.28)$$

where $\delta\Phi$ is the modulation depth. This is illustrated in figure 2.3. It shows the superimposed interference detector signal as a function of the target displacement. In this example, the laser wavelength was modulated with the frequency $f = 75$ kHz. This can be seen in the magnification of the signal around its maximum slope, where the sensitivity of the interference signal to changes of the wavelength is highest. The inset shows the intensity modulation as a function of time. The maximum intensity modulation δI occurs on the slopes of the interference pattern, whereas the effect of modulation is suppressed on the maxima and minima of the interference signal. In case of wavelength modulation, the modulation depth is defined by

$$\delta\Phi = -\frac{4p\pi n x}{\lambda^2} \delta\lambda \quad (2.29)$$

and is consequently proportional to the working distance. In order to realize dynamic travel ranges in excess of 1 m, this means that the modulation amplitude needs to be adjusted dynamically by scaling it linearly with the target distance. The superimposed signal can be used to deduce two 90° phase shifted signals I_{DC} and I_Ω , which are exemplary shown in figure 2.4 (a) and (b), respectively, as a function of the target displacement Δx . These signals are generated by splitting the superimposed signal in two signal paths. The first path low-pass filters the raw signal in order to remove the

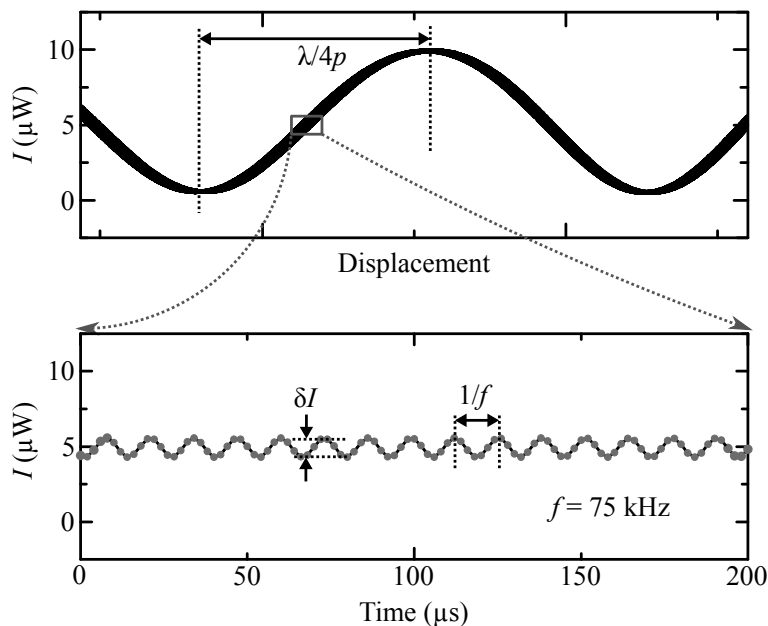


Figure 2.3: Illustration of the effect of wavelength modulation. Top: Interference intensity signal I and superimposed wavelength modulation signal δI as a function of the displacement. The distance between minimum and maximum corresponds to $\lambda/4p$, where λ is the laser wavelength and p is the folding order of the cavity. Bottom: Intensity modulation as a function of time. The wavelength is modulated according to $\lambda(t) = \lambda + \delta\lambda \sin \Omega t$, where $\Omega = 2\pi f t$. The maximum intensity modulation occurs on the slopes of the interference pattern, whereas the effect of modulation is suppressed on the maxima and minima of the interference signal.

high frequency carrier frequency, resulting in the direct signal I_{DC} . The second path uses a lock-in amplifier to detect the amplitude of the carrier frequency, resulting in the demodulated signal I_{Ω} . At those points where the direct signal has blind spots, i.e. where the sensitivity of the signal to displacements of the target is zero, the demodulated signal has its maximum sensitivity. This allows reproducing the phase angle with constant sensitivity.

2.4.1 Principles of Lock-in Detection

The demodulated signal I_{Ω} is recovered from the detector signal by means of a lock-in amplifier demodulating at the frequency Ω . [23, 24] The function of a lock-in amplifier can be described by a multiplication of a test signal U_{T} with a known reference signal U_{R} , followed by a low-pass filtering and an integration over a specified time. The test

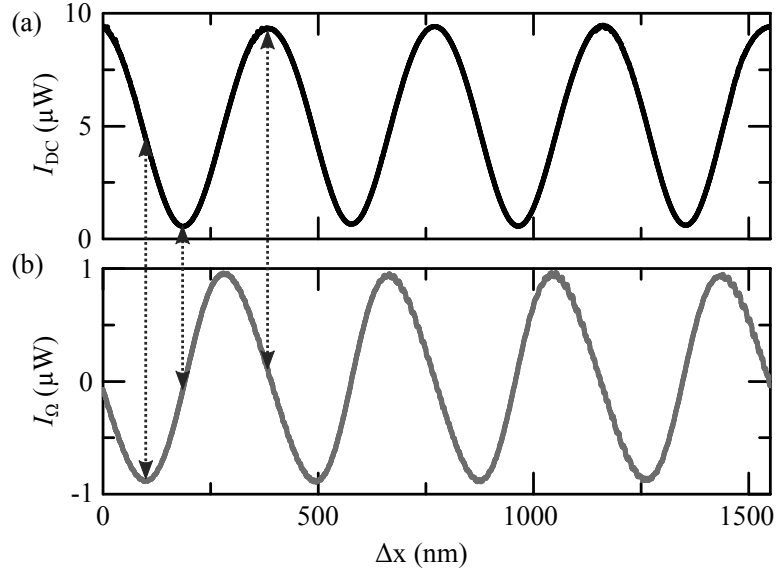


Figure 2.4: Low-pass Filtered reflected light intensity I_{DC} (a) and demodulated amplitude I_{Ω} (b) as a function of target displacement Δx . The maximum position sensitivity of the interference signal appears on the slopes of the interference, leading to a maximum demodulation amplitude δI in case of wavelength modulation. On the extrema of the interference signal, the effect of intensity modulation disappears and δI becomes zero.

and reference signals are represented by

$$U_T = U_T \cos(\Omega t + \phi_T) \quad (2.30)$$

$$U_R = U_R \cos(\Omega t + \phi_R), \quad (2.31)$$

where ϕ_T is the phase shift of the test signal and ϕ_R is the phase shift of the reference oscillator with respect to the original oscillator phase. A phase shift might originate from the response times of detector, laser and electronics, from the signal path length between modulator and laser and between detector and demodulator, and from the path difference in the Fabry-Pérot cavity. The voltage U_R is coupled to the laser current source, resulting in a wavelength modulation of the laser output. The same voltage U_R is also used as a reference for the demodulation process in the lock-in amplifier. Multiplication of both terms U_R and U_T yields the mixed signal

$$U_M = \frac{1}{2} U_R U_T \{ \cos(\phi_T - \phi_R) + \cos(2\Omega t + \phi_T + \phi_R) \}. \quad (2.32)$$

The mixed signal is then low-pass filtered in order to remove the 2Ω component, resulting in the output signal

$$U_{\text{out},X} = \frac{1}{2} U_R U_T \cos(\phi_T - \phi_R) \quad (2.33)$$

2.4. QUADRATURE DETECTION

The low-pass filtering must be realized in such a way that also high target velocities can be tracked. For example, a displacement velocity of $v = 2$ m/s would cause an oscillation of the interference pattern with a frequency of $f = v/x = 2.6$ MHz. The demodulation process can also be described by the integral

$$\delta I = \frac{1}{T} \int_0^T \sin(\Omega t + \delta\phi) U_T. \quad (2.34)$$

The whole process described above only recovers the component which is in phase with the modulator and is therefore also referred to as phase-sensitive detection. As a consequence, a test signal that has a phase shift of 90° with respect to the reference signal wouldn't produce any output. For this reason, the lock-in amplifiers in this work are using two digital phase-sensitive detectors (PSD) in order to recover also the current phase value of the PSD. The phase value is used in the initialization process of the interferometer for zeroing the phase of one PSD. In this way, the output of this PSD is maximized and directly provides the demodulation signal. The second PSD uses a reference which is 90° phase shifted with respect to the first detector. It produces the output

$$U_{\text{out},Y} = \frac{1}{2} U_R U_T \sin(\phi_T - \phi_R). \quad (2.35)$$

Division of both PDSs by the reference oscillator voltage and multiplication by $\sqrt{8}$ yields the output of the lock-in amplifier in V_{rms}

$$X = \sqrt{2} U_T \cos(\phi_{\text{PSD}}) \quad (2.36)$$

$$Y = \sqrt{2} U_T \sin(\phi_{\text{PSD}}), \quad (2.37)$$

where ϕ_{PSD} is the phase difference $\phi_T - \phi_R$. Note that this principle only works if the test signal has no offset. For this reason, the test signal first has to pass a high-pass filter.

2.4.2 Demodulation schemes

The detector signal is a superposition of signals which can be distinguished by their modulation frequency. These signals are given by

$$I(\Phi) = I_{\text{DC}}(\Phi) + I_{\Omega}(\Phi) + I_{2\Omega}(\Phi) + \dots \quad (2.38)$$

Decomposition of equation 2.28 in terms of Bessel functions $J_\nu(\delta\Phi)$ reveals the modulation amplitudes at different harmonics of the modulation frequency.[25] The first three terms are

$$I_{\text{DC}} = \frac{I_0}{2} + \frac{I_0}{2}C J_0(\delta\Phi) \cos(\Phi) \quad (2.39)$$

$$I_\Omega = -I_0C J_1(\delta\Phi) \sin(\Omega t) \sin(\Phi) \quad (2.40)$$

$$I_{2\Omega} = I_0C J_2(\delta\Phi) \cos(2\Omega t) \cos(\Phi). \quad (2.41)$$

Figure 2.5 shows the first three Bessel functions $J_\nu(\delta\Phi)$ as a function of the modulation depth $\delta\Phi$. Lock-in demodulation of the interference signal at the frequency Ω

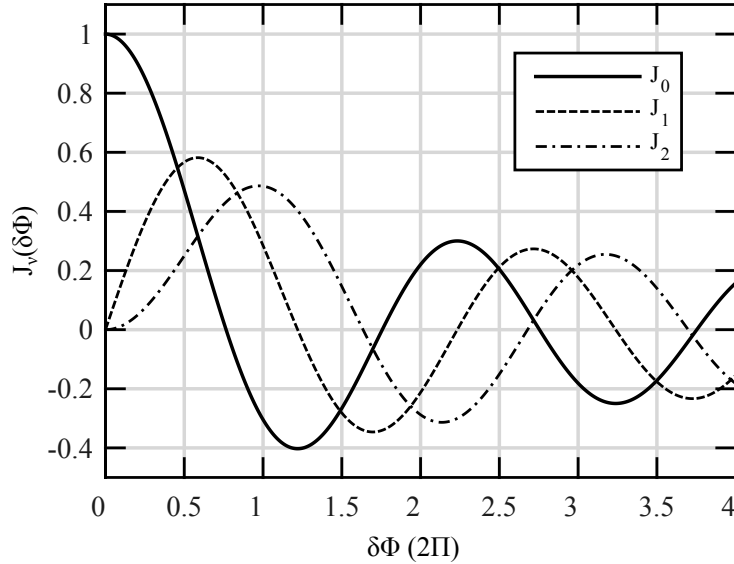


Figure 2.5: First three Bessel functions $J_\nu(\delta\Phi)$ as a function of the modulation depth $\delta\Phi$. J_1 and J_2 intersect at $\delta\Phi = 2.6$ rad.

yields the time-independent signal $I_{\Omega,\text{rms}} = -I_0C J_1(\delta\Phi) \sin(\Phi)/\sqrt{2}$, which is proportional to the derivative of the fundamental interference signal I_{DC} . In the same way, the derivative of $I_{\Omega,\text{rms}}$ is gained through lock-in demodulation of the interference signal at the frequency 2Ω , yielding $I_{2\Omega,\text{rms}} = I_0C J_2(\delta\Phi) \cos(\Phi)/\sqrt{2}$.

The 90° phase shift between the signals I_{DC} and $I_{\Omega,\text{rms}}$ (DC/ Ω quadrature scheme) and the signals $I_{\Omega,\text{rms}}$ and $I_{2\Omega,\text{rms}}$ ($\Omega/2\Omega$ quadrature scheme) allows recovering the fractional part of the interference phase Φ in two different ways.[3, 26] In both methods, a Lissajous figure is formed by two normalized 90° phase shifted sinusoidal signals. The angle in the Lissajous figure representation directly defines the fractional part of the

2.4. QUADRATURE DETECTION

interference phase Φ . In both methods, the phase angle Φ is recovered by calculating the arc tangent between the normalized signals according to

$$\Phi_{\Omega,2\Omega} = \arctan \left(-\frac{I_{\Omega,\text{rms}}}{I_{2\Omega,\text{rms}}} \cdot \frac{J_2(\delta\Phi)}{J_1(\delta\Phi)} \right) \quad (2.42)$$

$$\Phi_{\text{DC},\Omega} = \arctan \left(\frac{I_{\Omega,\text{rms}}}{I_{\text{DC}} - \frac{I_0}{2}} \cdot \frac{\frac{I_0}{2} C J_0(\delta\Phi)}{J_1(\delta\Phi)} \right) \quad (2.43)$$

The position difference Δx between two stationary positions x_1 and x_2 in a vacuum is then recovered using the phase difference $\Delta\Phi$ and the relation

$$\Delta x = \frac{\lambda}{4p\pi} \Delta\Phi. \quad (2.44)$$

The measurement range achievable with both demodulation schemes is limited to small and large cavity lengths when using a constant modulation depth. At small lengths, the range is limited by the demodulator's ability to resolve small modulation amplitudes. For large distances, the modulation amplitude can go to zero as a consequence of the increasing modulation depth (cf. zero point of equation 2.40). Technically, the measurement range can be increased by a dynamic adaptation of the modulation amplitude. This means, according to equation 2.29, that the modulation amplitude must be decreased linearly with increasing cavity length in order to maintain a constant modulation depth. This can be realized, for example, by an open-loop controller using the absolute distance information gained from an independent measurement in order to act on the laser modulation current.

2.4.3 Corrections for long cavities

Extending the measurement range of the interferometer beyond 1 m is associated with several electronic adaptations which have to be considered. It concerns the demodulator phase, the modulation frequency and the modulation amplitude respectively the modulation depth. This section provides some background concerning these adaptations.

2.4.3.1 Phase delay

The cavity length induces a phase delay between the reference oscillator and the reflected wavelength modulated wave. For a phase delay of 90° , the demodulated signal

becomes zero. Assuming a modulation frequency of $f_{\text{mod}} = 12.5$ MHz, corresponding to a periodic time of $T = 1/f = 80$ ns, the 90° phase delay is reached after 20 ns. The wave travels with a speed of $c/n \approx 3 \cdot 10^8$ m/s through the cavity and covers during the time of 20 ns a cavity length of $x = ct/2n = 3$ m. It is for this reason that the phase delay has to be adjusted dynamically when measuring over a range of more than 3 m. In practice, this can be realized by shifting the phase according to the current displacement by means of an open-loop control algorithm acting on the demodulator phase, which is implemented in the processor electronics allowing for real-time operation. The phase is zeroed upon initialization so that oscillator and reflected wave are in phase.

2.4.3.2 Interference of the wavelength modulation frequency

When tracking the position of a target which is displaced by several meters, it can be observed that the demodulation signal goes against zero at around 7 m ($f_{\text{mod}} = 12.5$ MHz), even if the of wavelength modulation amplitude and the demodulator phase is dynamically adapted. In order to understand this phenomenon, the equations for the interference signal have to be extended by the sinusoidal chirp (or frequency modulation) of the laser frequency. An optical field $E(x, t)$, which is weakly wavelength modulated by an amount $\Omega = c \cdot \delta k = 2\pi f_{\text{mod}}$, can be expressed by the fundamental wave field with the photon frequency ω and two sidebands with the photon frequencies[27]

$$\omega^\pm = \omega \pm \Omega \quad (2.45)$$

The chirp frequency Ω is much lower than the photon frequency ω , $\Omega \ll \omega$, and much higher than the laser line width, $\Omega \gg \text{laserlinewidth}$. In an interferometric measurement a probe field is made to interfere with a reference field. The half path difference between both fields is denoted by x . The probe field is delayed with respect to the reference field, adding a phase for the carrier wave and for the two side bands. Here, the wave vectors k^\pm of the two side bands and of the carrier k are given by

$$k^\pm = \omega^\pm/c \quad \text{and} \quad k = \omega/c \quad (2.46)$$

and the differential wave vector δk is given by

$$\delta k = k^+ - k = k - k^- = \Omega/c. \quad (2.47)$$

2.4. QUADRATURE DETECTION

In this way, the laser field can be decomposed into Fourier components according to

$$E_{\lambda\text{mod}}(x, t) = E_0(x, t) + E^+(x, t) + E^-(x, t), \quad (2.48)$$

where

$$E_0(x, t) = Ae^{i(2kx - \omega t)} \quad (2.49)$$

and

$$E^\pm(x, t) = Me^{i(2k^\pm x - \omega^\pm t)}. \quad (2.50)$$

Assuming that half of the laser field is used as probe field (sample beam), the probe field becomes

$$E_{\text{probe}}(x, t) = \frac{1}{2} \left\{ Ae^{i(2kx - \omega t)} + Me^{i(2k^+ x - \omega^+ t)} - Me^{i(2k^- x - \omega^- t)} \right\}. \quad (2.51)$$

The field $E_{\text{probe}}(x, t)$ is made to interfere with the reference field

$$E_{\text{ref}}(x, t) = \frac{1}{2} \left\{ Ae^{(-i\omega t)} + Me^{(-i\omega^+ t)} - Me^{(-i\omega^- t)} \right\}. \quad (2.52)$$

At the detector, a power intensity proportional to the square modulus of the sum of both fields

$$I = (E_{\text{probe}} + E_{\text{ref}}) \cdot (E_{\text{probe}} + E_{\text{ref}})^* \quad (2.53)$$

is detected. Expanding this product produces terms that are proportional to M , M^2 and terms that do not depend on M . The terms independent of M yield the interference pattern in absence of modulation,

$$I_{\text{DC}} \propto \frac{1}{2} \{1 + \cos(2kx)\}. \quad (2.54)$$

After some lengthy calculations, the optical signal proportional to $M/4$ yields a periodic function of Ωt ,

$$I_\Omega = -M \sin(2kx) \{ \sin(\Omega \cdot t) - \sin(\Omega t - 2\delta kx) \}. \quad (2.55)$$

Further separation of both terms in $\sin(\Omega t)$ and $\cos(\Omega t)$ yields

$$I_\Omega = -M \sin(2kx) \{ \sin(2\delta kx) \cos(\Omega \cdot t) + [1 - \cos(2\delta kx)] \sin(\Omega \cdot t) \}, \quad (2.56)$$

or equivalently

$$I_\Omega = -M \sin(2kx) \{ \sin(2\Omega x/c) \cos(\Omega \cdot t) + [1 - \cos(2\Omega x/c)] \sin(\Omega \cdot t) \}. \quad (2.57)$$

Equation 2.56 shows that the interferogram is strictly a function of $\sin(2kx)$ and, thus, in quadrature with the DC signal of equation 2.54. This feature is fundamental to the quadrature detection scheme used for position tracking. Equation 2.56 is further a function of Ωt which allows for demodulation.

For small values of δkx ($\delta kx \ll 1$), equation 2.56 develops into

$$I_{\Omega} = -M \sin(2kx) \cos(\Omega t), \quad (2.58)$$

which is the form that was used so far for short enough cavities or slow enough modulation frequencies (cf. equation 2.40). For larger cavities, when the path difference becomes $2\delta kx = 2\pi N$, where N is a positive integer, or equivalently for the condition $x = \pi cN/\Omega$, the demodulation signal becomes zero. In case of modulating at $\Omega = 2\pi f_{\text{mod}} = 2\pi \cdot 12.5$ MHz, the point of zero demodulation signal is at $x = 12$ m, which constitutes a fundamental limit for the possible measurement range. Increasing the measurement range is only possible at the expense of measurement speed by decreasing the modulation frequency. For example, wavelength modulation at 3 MHz would result in a maximum measurement range of 48 m.

2.4.3.3 Modulation depth

As already mentioned, longer measurement ranges require a dynamic adaptation of the modulation amplitude in order to prevent excess modulation. Theoretically, this means that the modulation amplitude must be decreased linearly with increasing cavity length. However, the experiment shows that things are more complex. In order to maintain a constant modulation depth, the modulation amplitude as a function of the target distance equals an exponential decay rather than a linear decay. After a few meters, the modulation amplitude goes, contrary to what is expected by theory, through a minimum and even starts raising again. The reason for this behavior lies in the interference of the field generated by the wavelength modulation frequency with itself, causing a reduction of the modulation depth for increasing cavity length.

2.5 Reflectivity of the fiber-coupled Fabry-Pérot cavity

So far, calculations only considered two beam interference, which is a valid assumption for the Michelson interferometer. The interferometer presented in this work, however,

2.5. REFLECTIVITY OF THE FIBER-COUPLED FABRY-PÉROT CAVITY

is based on a Fabry-Pérot cavity which is formed between the cleaved, semitransparent end face of a single mode fiber and a movable target, as shown in figure 2.6. An

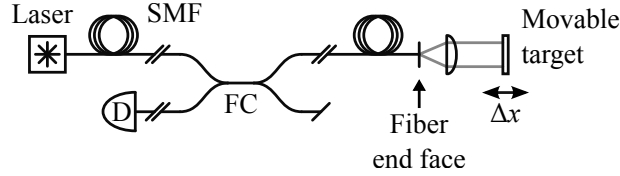


Figure 2.6: Schematic of the fiber coupled Fabry-Pérot interferometer. The laser light is routed to the fiber end face by means of optical single mode fibers (SMF) and a fiber coupler (FC). The Fabry-Pérot cavity is formed between the fiber end face and the target. The interference created in the cavity is detected at the photo detector (D).

optical cavity is an resonator in which the light circulates between reflecting surfaces. A Fabry-Pérot cavity or etalon is also an optical resonator which is set up between two parallel reflecting mirrors, of which at least one is semi-transparent. The Fabry-Pérot interferometer goes back to the year 1899, where of Charles Fabry and Alfred Pérot published their work about the interference obtained from thin films.[28, 29] Most applications involving Fabry-Pérot etalons rely on a high reflectivity of the mirrors and are widely used, for example, in telecommunications for laser wavelength stabilization and wavelength filtering.

In this section, a model for the calculation of the interference signal created in a Fabry-Pérot cavity will be deduced and used in a later chapter to calculate the angular alignment tolerance and the position range of different kinds of sensor heads. The formula will be used in this section to describe the dependence of the interference signal on the target reflectivity and on the power coupling efficiency of the fiber. Furthermore, the nonlinearities which are characteristic for the Fabry-Pérot interferometer will be described.

2.5.1 Calculation of the Fabry-Pérot formula

The model, which describes the reflectivity of the Fabry-Pérot interferometer, is based on the Airy formula [30]. It takes into account different reflectivities of the cavity surfaces as well as the fiber coupling efficiency η of the system, which denotes the percentage of power transmitted from the cavity into the fiber with respect to the total power emitted from the fiber.[31, 32] In this way, the interference created at the fiber end face can be determined analytically. The cavity, which behaves like an optical

resonator, is formed between the cleaved end face of an optical single mode fiber with reflectivity R_1 and a tiltable target with reflectivity R_2 , as shown schematically in figure 2.7. The linear polarized laser light emitted from the laser is expressed by the

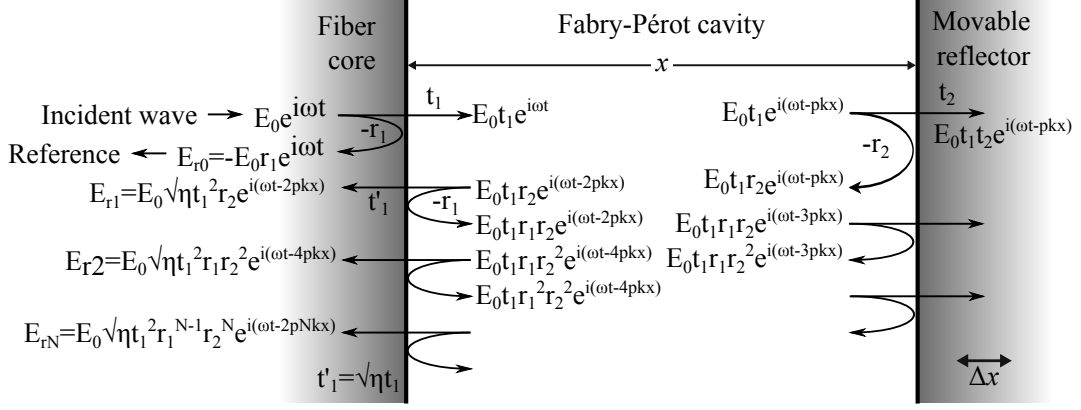


Figure 2.7: Sketch of the Fabry-Pérot cavity illustrating the different electric fields $E(x, t)$ which occur at different interfaces. r_1 and r_2 denote the amplitude reflection coefficient of the interface between the fiber and cavity and of the movable mirror, respectively. The transmission from the cavity to the fiber is represented by the amplitude transmission coefficient $t'_1 = \sqrt{\eta} t_1$, where η denotes the fiber coupling efficiency. x denotes the distance between the fiber and mirror, k denotes the wave number of the light, ω denotes the angular frequency of the light, and p denotes the folding order of the cavity.

electromagnetic wave $E = E_0 e^{i\omega t}$. It is routed to the fiber end face, where part of the light is reflected by the interface between glass and air with the amplitude reflection coefficient r_1 , thus forming the reference beam E_{r0} . The wave traveling from the fiber to the cavity experiences a phase shift of π upon reflection by the interface, indicated by the negative sign of r_1 in figure 2.7. The remaining part of the light exits the fiber with the amplitude transmission coefficient t_1 under a specific cone angle $2 \cdot \Theta_{\text{air}}$ which is defined by the numerical aperture of the fiber. In the cavity, the light can take different paths depending on the used lenses and the target tilt. Along this path, the light resonates between the Fabry-Pérot mirrors with the amplitude reflection coefficients r_1 and r_2 , given by $r_1 r_1^* = R_1$ and $r_2 r_2^* = R_2$. After each cycle (the number of cycles is denoted as N), part of the light is transmitted into the fiber where it interferes with the reference beam. The light is transmitted with the amplitude transmission coefficient $t'_1 = \sqrt{\eta} t_1$ and the phase shift $\Delta\varphi = \delta = -2pkx = -2kl$, where l denotes the cavity length, x denotes the distance between the fiber and mirror, and k denotes the wave number of the light. p denotes the folding order of

2.5. REFLECTIVITY OF THE FIBER-COUPLED FABRY-PÉROT CAVITY

the cavity, which indicates whether the beam passes the cavity only once ($p = 1$, single pass) or twice ($p = 2$, double pass). Since the light transmission into the fiber also depends on the angle of incidence, which can vary with the target tilt, the model also has to consider the power-coupling efficiency of the fiber. When taking the square root of η , the power-coupling efficiency can be applied to electromagnetic fields using the relation $t'_1 = \sqrt{\eta}t_1$. Summing over all portions which are coupled back into the fiber yields an expression for the reflected electromagnetic wave E_r . The light reflected by the cavity is thus the superposition of the reference wave with the sum of all waves which are coupled back into the fiber. The total electric field E_r is therefore

$$\begin{aligned}
E_r &= E_0 r_1 e^{i\omega t} e^{i\pi} + E_0 t_1 r_2 t'_1 e^{i\omega t} e^{-i2kl} + E_0 t_1 r_2 r_1 r_2 t'_1 e^{i\omega t} e^{-i4kl} + \dots = \\
&= -E_0 r_1 e^{i\omega t} + E_0 \sqrt{\eta} t_1^2 e^{i\omega t} \sum_{N=1}^s r_1^{N-1} r_2^N e^{-i2pNkl} = \\
&= -E_0 r_1 e^{i\omega t} + E_0 \sqrt{\eta} \frac{t_1^2}{r_1} e^{i\omega t} \sum_{N=1}^s r_1^N r_2^N e^{-iN\delta} = \\
&= E_0 e^{i\omega t} \left(\sqrt{\eta} \frac{t_1^2}{r_1} \sum_{n=0}^{s-1} (r_1 r_2 e^{-i\delta})^{n+1} - r_1 \right) \\
&= E_0 e^{i\omega t} \left(\sqrt{\eta} t_1^2 r_2 e^{-i\delta} \sum_{n=0}^{s-1} (r_1 r_2 e^{-i\delta})^n - r_1 \right). \tag{2.59}
\end{aligned}$$

The sum term can be rewritten by the geometric series

$$\sum_{k=0}^n z^k = \frac{1 - z^{n+1}}{1 - z}. \tag{2.60}$$

In the limit of $n \rightarrow \infty$ and if $|z| < 1$, the geometric series becomes

$$\lim_{n \rightarrow \infty} \frac{1 - z^{n+1}}{1 - z} = \frac{1}{1 - z}. \tag{2.61}$$

In this way, the reflected wave can be rewritten as

$$\begin{aligned}
E_r &= E_0 e^{i\omega t} \left(r_1 - \frac{\sqrt{\eta} t_1^2 r_2 e^{-i\delta}}{1 - r_1 r_2 e^{-i\delta}} \right) = \\
&= E_0 e^{i\omega t} \left(\frac{r_1 - r_2 (r_1^2 + \sqrt{\eta} t_1^2) e^{-i\delta}}{1 - r_1 r_2 e^{-i\delta}} \right) = \\
&= E_0 e^{i\omega t} \left(\frac{r_1 - r_2 f e^{-i\delta}}{1 - r_1 r_2 e^{-i\delta}} \right). \tag{2.62}
\end{aligned}$$

In the last set of equations, the concept of an effective reflection coefficient $r_{2,\text{eff}} = fr_2 = (r_1^2 + \sqrt{\eta}t_1^2)r_2$ was introduced. The product $E_r \cdot E_r^*$ finally is proportional to the reflected intensity I_r , according to

$$\begin{aligned} I_r &= E_r E_r^* = \\ &= E_0^2 \left(\frac{r_1 - r_2 f e^{-i\delta}}{1 - r_1 r_2 e^{-i\delta}} \right) \left(\frac{r_1 - r_2 f e^{i\delta}}{1 - r_1 r_2 e^{i\delta}} \right) = \\ &= E_0^2 \left(\frac{r_1^2 + (fr_2)^2 - 2r_1 fr_2 \cos \delta}{1 + (r_1 r_2)^2 - 2r_1 r_2 \cos \delta} \right), \end{aligned} \quad (2.63)$$

where the identity $e^{i\delta} + e^{-i\delta} = 2 \cos \delta$ was used. The intensity reflected by a Fabry-Pérot cavity is consequently given by

$$I_{\text{FP}} = I_0 \frac{r_1^2 + (fr_2)^2 - 2r_1 fr_2 \cos \Phi}{1 + (r_1 r_2)^2 - 2r_1 r_2 \cos \Phi}, \quad (2.64)$$

where

$$f = r_1^2 + \sqrt{\eta}t_1^2. \quad (2.65)$$

and Φ is the interference phase. Equation 2.64 takes already into account the phase

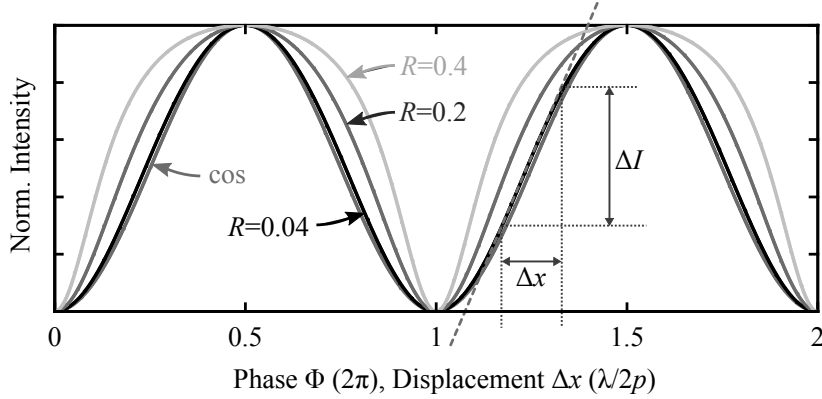


Figure 2.8: Normalized interference signal for different values of the cavity finesse. In this example, the Fabry-Pérot mirrors have equal reflectivities $R_1 = R_2 = R$. In the past, the Fabry-Pérot interferometer was typically used in the linear range of the interference pattern, where the intensity change ΔI is proportional to the displacement Δx . A higher finesse leads to a higher slope and consequently to a higher sensitivity, but affects negatively the linearity when used with the quadrature detection scheme.

shift which occurs between reflections within the cavity. The amplitude transmission coefficients t_1 and t_1' for the waves traveling from the fiber to the cavity and vice versa, respectively, are related to the reflectivity R_1 and the transmissivity T_1 of the

glass/air interface by $t_1 t_1^* = T_1 = 1 - R_1$.

The quality of the interferometric signal is quantified by the fringe contrast or visibility C (cf. equation 2.13) and by the finesse of the cavity \mathcal{F} . The finesse of the cavity is given by [33]

$$\mathcal{F} = \frac{\pi \sqrt{r_1 r_{2,\text{eff}}}}{1 - r_1 r_{2,\text{eff}}}, \quad (2.66)$$

where the concept of an effective reflection coefficient $r_{2,\text{eff}}$, given by $r_{2,\text{eff}} = f r_2$, was introduced. The cavity finesse can be seen as a measure for how close the interference pattern is to a sinusoidal shape.

The quadrature detection scheme is based on a sinusoidal shape of the interference pattern, which is ensured by a low-finesse of the sensing cavity. Deviations from the sinusoidal shape would degrade the accuracy of the displacement measurement when one of the quadrature schemes is applied. Figure 2.8 shows the normalized interference signal for different values of the cavity finesse. The lower the reflectivity of the Fabry-Pérot mirrors is, the more similar is the interference pattern to a sinusoidal shape. This explains why it is an advantage in Fabry-Pérot displacement interferometry to have a low reflectivity of the Fabry-Pérot mirrors rather than a high reflectivity known from usual etalons, where a high reflectivity relates to a high quality of the etalon. In this work, the low reflectivity of the fiber and the low effective reflectivity of the movable mirror ensures a high displacement accuracy.

2.5.2 Interference intensities in relation to the reflectivity

Equation 2.64 shows that the interference contrast crucially depends on the reflectivity of the movable target. This is demonstrated in figure 2.9, which shows the constructive and destructive interference intensities (a) and corresponding interference contrast (b) as a function of the target reflectivity R_2 , assuming $\eta = 1$. The contrast is maximum if the target reflectivity R_2 equals the reflectivity of the fiber core $R_1 = 0.0359$. For both higher and lower reflectivities, the contrast decreases as a result of the unbalanced reflected light intensities. In case of higher reflectivities, the contrast could be increased by reducing the coupling efficiency, since $r_{2,\text{eff}}$ also depends on the coupling efficiency according to equation 2.64. In order to achieve a higher interference contrast, high target reflectivities can generally be compensated by reducing the coupling efficiency.

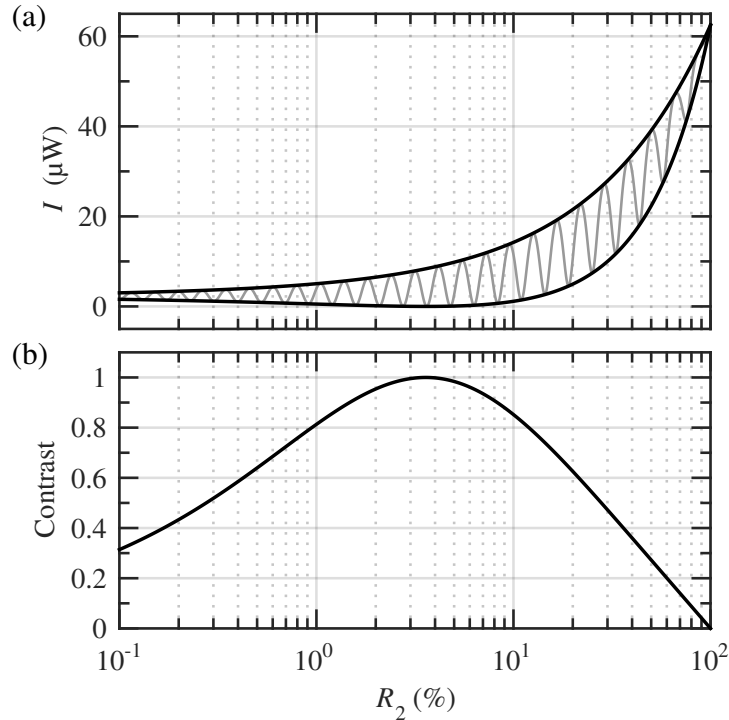


Figure 2.9: Calculated constructive (upper curve) and destructive (lower curve) interference intensities I (a) and corresponding contrast (b) as a function of the target reflectivity R_2 . Maximum contrast is achieved for equal reflectivity of target and fiber core (here about 4%). The 4% reflection from a flat polished fiber end is defined to create a $2.5 \mu\text{W}$ signal at the detector. The interference pattern in between the constructive and destructive interference are shown for illustration purposes only.

2.5.3 Interference intensities in relation to the coupling efficiency

Equation 2.66 shows that the Finesse of the cavity not only depends on the reflectivities of the Fabry-Pérot mirrors, but also on the coupling efficiency η . Figure 2.10 shows the constructive and destructive interference intensities (a) and corresponding interference contrast (b) as a function of the coupling efficiency η , assuming $R_2 = 1$. Maximum contrast is achieved if $\eta = 2.78\%$. The coupling efficiency can practically be reduced by, e.g. increasing the target angular misalignment or by using a sensor head configured to provide a convergent or divergent beam. In case of a focused beam, the coupling efficiency can be reduced by defocusing of the target.

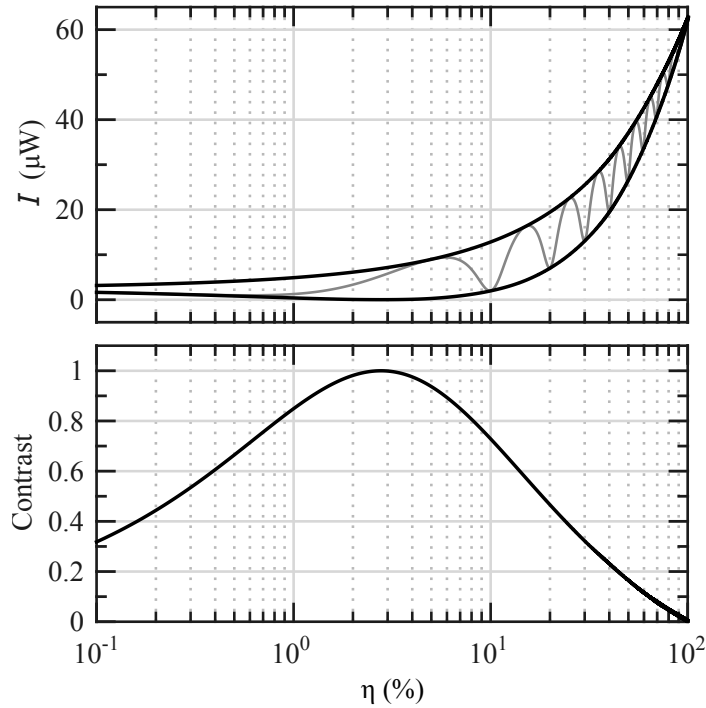


Figure 2.10: Calculated constructive (upper curve) and destructive (lower curve) interference intensities I (a) and corresponding contrast (b) as a function of the coupling efficiency η for a target reflectivity $R_2 = 1$. Maximum contrast is achieved for $\eta = 2.78\%$. The interference pattern in between the constructive and destructive interference are shown for illustration purposes only.

2.5.4 Nonlinearities

Plotting the displacement values measured with one of the two quadrature schemes against the real displacement results in a line which is superimposed by periodic oscillations. These oscillations are due to deviations of the measured interference phase from reality and arise from multiple reflections in the Fabry-Pérot cavity. This is illustrated in figure 2.11 for both quadrature detection schemes. Figure 2.11 (a) and (c) represent the calculated Lissajous figures of quadrature schemes $0/\Omega$ and $\Omega/2\Omega$, respectively. The calculations of the nonlinearities are based on equation 2.64 and its first and second numeric derivations, which reproduce the first and second harmonic demodulation signals, respectively. All signals are normalized in such a way that their maximum absolute values are 1. Figure 2.11 (b) and (d) represent the deduced nonlinearities of quadrature schemes $0/\Omega$ and $\Omega/2\Omega$, respectively. The theoretical nonlinearities of the $0/\Omega$ quadrature scheme are within ± 4.9 nm and

within ± 17.0 nm in the $\Omega/2\Omega$ quadrature scheme. In the calculations, a coupling efficiency of $\eta = 1$ was assumed. When η decreases, e.g. when increasing the target tilt angle, also the nonlinearities decrease.

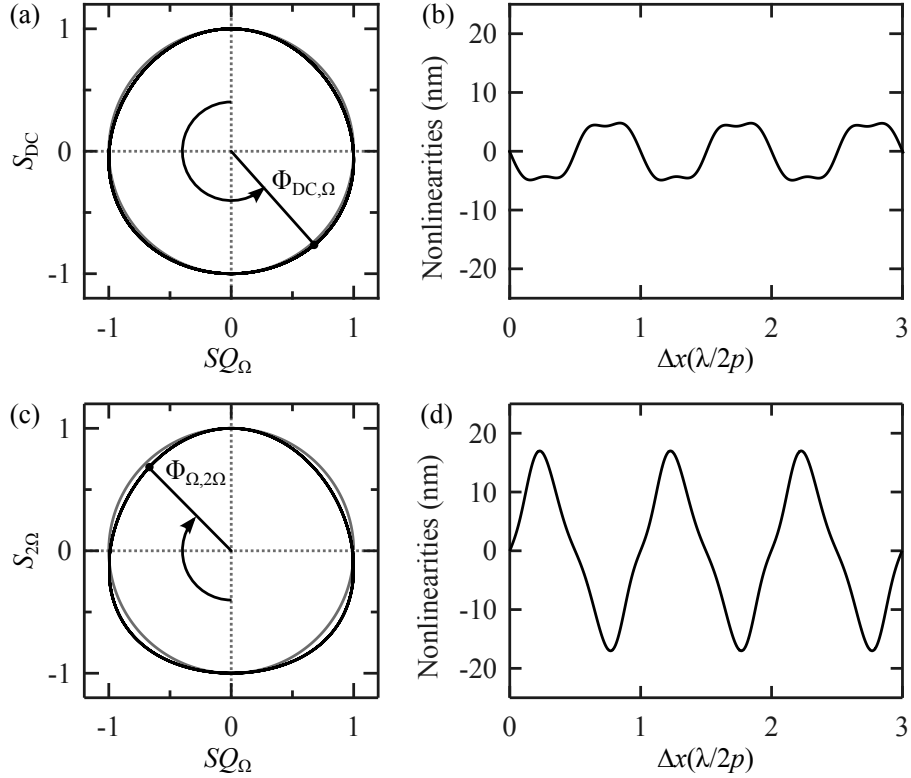


Figure 2.11: Calculation of the normalized Lissajous figure (left) and corresponding nonlinearities (right) for two quadrature detection schemes $0/\Omega$ (top) and $\Omega/2\Omega$ (bottom). Quadrature scheme $0/\Omega$ is based on the normalized direct signal S_{DC} and the normalized demodulated quadrature signal SQ_{Ω} . Quadrature scheme $\Omega/2\Omega$ is based on the normalized demodulated signal $S_{2\Omega}$ and the normalized demodulated quadrature signal SQ_{Ω} .

As the nonlinearities are based on equation 2.64, their magnitude depends on the target reflectivity and on the coupling efficiency. This is demonstrated in figure 2.12, which shows the nonlinearities for a target reflectivity of 2%, 4%, 6%, 8% and 10%.

2.6 Summary

In this chapter, the theoretical principle of operation of the interferometer was described. The theoretical considerations allow drawing several fundamental conclusions. For instance, it was demonstrated that the phase shift measured with this type

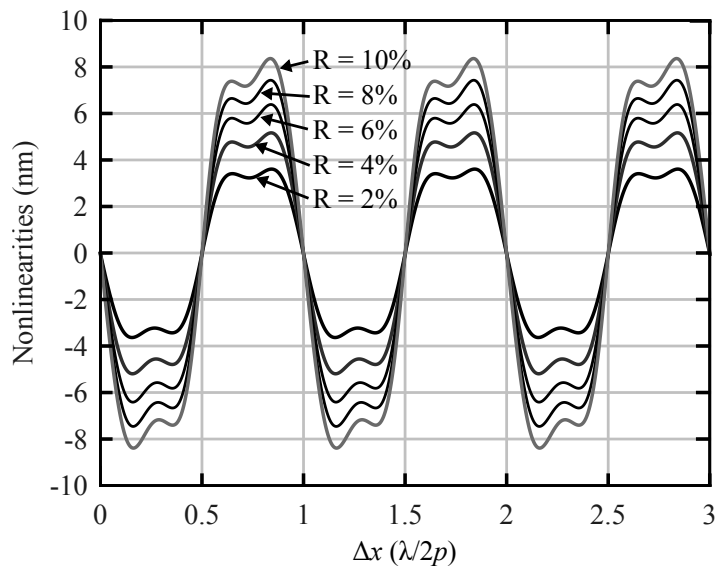


Figure 2.12: Periodic nonlinearities as a function of the displacement Δx for different target reflectivities R . The magnitude of the nonlinearities increases with increasing target reflectivity.

of interferometer is solely attributed to the Doppler effect.

This phase shift can be measured using two different quadrature detection schemes, which are based on the high frequency modulation of the laser wavelength. In the first detection scheme, also referred to as $0/\Omega$ quadrature scheme, the low-pass filtered signal and the 90° phase shifted signal gained through demodulation of the interference signal at the frequency Ω form a Lissajous figure whose angle represents the interference phase. In the second detection scheme, also referred to as $\Omega/2\Omega$ quadrature scheme, the Lissajous figure is formed by the signals gained through demodulation at the frequency Ω and 2Ω . The special $0/\Omega$ quadrature detection schemes limit the working range from few millimeters to several meters. The minimum working distance, which is typically in the order of few millimeters, mainly depends on the wavelength modulation depth, which is smaller the shorter the cavity is. At small working distances, the maximum modulation depth is insufficient for lock-in demodulation because the wavelength modulation cannot be increased indefinitely. The maximum working distance depends on several parameters like wavelength modulation depth, modulation frequency, and modulation phase. At long working distances, the measurement range is theoretically only limited by the destructive interference of the modulation frequency, provided that the modulation phase is updated dynami-

cally and that the modulation depth is adapted dynamically in order to maintain a constant modulation depth.

The calculations in this chapter further reveal the dependency of the reflected interference signal as a function of the target reflectivity and the power coupling efficiency. Maximum contrast occurs for the same fiber core and target reflectivity, in accordance with a target reflectivity of 3.6%. In case of a target reflectivity of 100%, maximum contrast occurs at a power coupling efficiency of 2.8%.

Using a Fabry-Pérot interferometer instead of an ideal Michelson interferometer leads to deterministic 2π periodic phase nonlinearities with an amplitude that depends on the cavity finesse and on the power coupling efficiency of the reflected light. These nonlinearities arise from multiple reflections within the cavity. Both quadrature detection schemes have been investigated with respect to their nonlinearities. In case of a cavity with a target reflectivity of 3.6% (best signal contrast), the maximum position deviation from linearity is ± 4.9 nm in the $0/\Omega$ quadrature scheme and ± 17.0 nm in the $\Omega/2\Omega$ quadrature scheme.

3 Measuring system

The field of application of today's commercially available displacement tracking interferometers is restricted. On the one hand, their use is limited to ambient environments mainly because of sensitive electronic parts in the sensor head. The size of these sensor head, which can reach several centimeters in each dimension in case of a Michelson interferometer, further limits their use to applications with suitable large space. This restriction results mainly from bulky optical parts like beam splitters or wave plates. On the other hand, the high costs prevent their use in higher volume projects, thus restricting interferometry to mere calibration applications.

For these reasons, this work pursues a different approach, namely that of a fiber-optic Fabry-Pérot interferometer operated in the telecom wavelength range. Compared with the widely used interferometers on the market, this type of interferometer has several advantages. The use of telecom wavelength parts makes the interferometer cost-efficient and enables its miniaturization. In particular, the system is based on a tunable distributed feedback laser which enables using a quadrature detection scheme based on the wavelength modulation of the laser and the demodulation of the modulated interference signal. The miniaturization of the interferometer and its robustness profit from the use of this quadrature detection scheme, because the evaluation electronic can be completely separated from the sensing cavity. However, this laser requires an external stabilization to a known wavelength reference in order to achieve a stability which is comparable to that of widely used commercial gas lasers.

In this chapter the experimental interferometric measuring system will be described and the performance will be demonstrated by means of different measurement setups. In particular, it will be demonstrated that the interferometer system tracks velocities up to 2 m/s with a measurement bandwidth (BW) of 10 MHz, and this even in the harshest environments such as cryogenic temperatures. The interferometer achieves a repeatability of $3\sigma = 0.45$ nm, a digital resolution of 1 pm and an accuracy of up to 1 nm and can track displacements over a range of 1 m. It is further well suited

for multi-channel applications. The simultaneous measurement of up to 12 axes was successfully demonstrated during this work. Apart from that, the performance of the interferometer will be qualified for operation at ambient conditions. A weather station is used in this case for the refractive index compensation. The key specifications of the interferometer are summarized in figure 3.1.

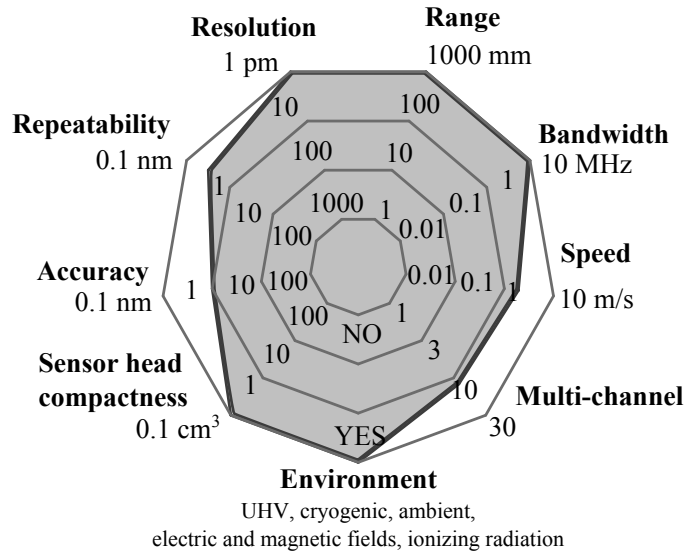


Figure 3.1: Specification map of the presented interferometer.

3.1 Sensor specification

The specification of sensors often leads to misunderstandings since some words are assigned to different meanings. In order to generate a common understanding of the words used in this work, this section provides a brief definition of the key parameters in accordance with standards that have been defined in literature.[8, 34] Measurement precision specifies how much the results of repeated measurements deviate under certain conditions. Precision specifies measurement repeatability, if it implies the same measurement conditions, and reproducibility, if it implies different conditions. Position resolution refers to the smallest position change that can be detected by the sensor and depends on the ability of the system to resolve changes of the interference phase angle. In general, the resolution is better the smaller the measurement bandwidth and the higher the measured frequency is. The sensor accuracy is the supreme discipline of a position sensor and specifies the difference between actual (real) and

measured value. The range of the sensor is the minimum and maximum position that can be detected, whereas the dynamic range specifies the ratio between range and resolution.[35] Beside these definitions, which are indispensable for the specification of the interferometer, there are also some other words that are often used with regard to interferometry. Sensitivity, for example, is no feature that is obvious from the position output of the interferometer system. It rather describes the sensitivity of the interference phase to changes of the position and depends on the used wavelength and on the folding order of the beam path, i.e. the smaller the wavelength and the larger the folding order of the measurement beam path, the higher is the interferometer sensitivity to position changes. Together with the sensitivity, the phase resolution determines the position resolution of our sensor.

3.2 Principle of operation

The interferometer setup is schematically shown in figure 3.2. The light from a tunable distributed feedback (DFB) laser emitting in the telecom wavelength range is routed to a first optical two-by-two directional fiber coupler (FC1, coupling ratio 50:50) via an optical single mode fiber (SMF). An optical fiber-coupled isolator (ISO) at the laser output is used to protect the laser from back reflections in the fiber circuit. The DFB laser has an optical output power of about 10 – 20 mW, which is reduced to about 150 μ W at the sensor head using a fiber-optic attenuator (OA) connected to the laser output. The laser wavelength is modulated with the frequency $f = \Omega/2\pi = 12.5$ MHz. The first output of coupler (FC1) is connected to a wavelength reference required for wavelength stabilization. The transmitted light is detected by the photodetector D2. The second output is connected to a second fiber coupler (FC2) which remotely connects the sensor head with the fiber circuit of the interferometer system. In order to simultaneously track the displacement of multiple axes, coupler FC1 can also be replaced by a $1 \times n$ fiber coupler, where $n - 1$ is the number of possible axes. The remote fiber ends up in a flat polished end (here realized by a FC/PC connector) which reflects part of the incoming light (about 4%) and, in this way, provides the reference beam of the interferometer. It follows that the reference beam length is zero ($x_r = 0$), a fact which makes the interferometer insensitive to thermal drifts. The rest of the light exits the fiber with a certain cone angle. Here, x denotes the distance between the fiber and mirror. After being reflected off

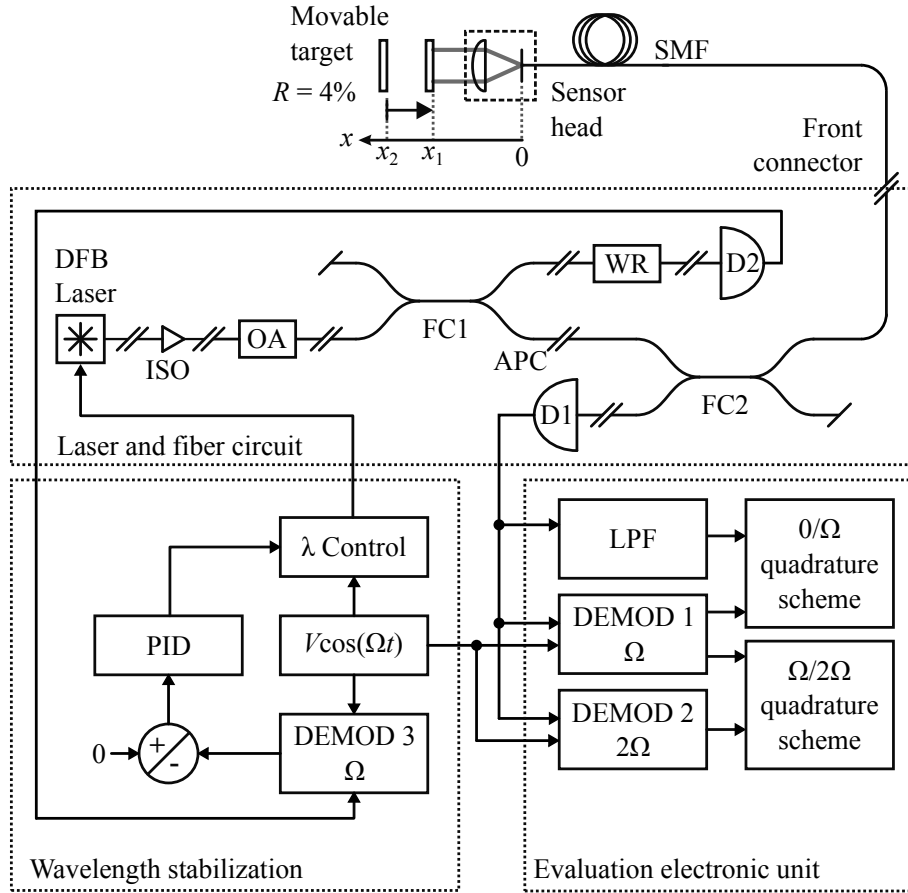


Figure 3.2: Fiber-optic Fabry-Pérot interferometer setup demonstrating the operation using two different quadrature detection schemes. The single mode fiber (SMF) circuit comprises two photodetectors D1 and D2, a wavelength reference WR, an isolator ISO, an attenuator OA, two directional fiber couplers FC1 and FC2, and a tunable distributed feedback (DFB) laser. The components are interconnected by angled physical contact (APC) connectors or by fusion splicing. The quadrature detection unit can be configured to use either the output of a low-pass filter LPF and a demodulator DEMOD1 or to use the output of two demodulators DEMOD1 and DEMOD2. The wavelength stabilization circuit comprises a feedback loop PID, a wavelength control circuit λ Control, an oscillator providing the voltage $V \cos \omega t$, and a demodulator DEMOD3.

the target reflector, part of the light is coupled back into the fiber and recombines with the reference beam. The other part of the light, which is not coupled into the fiber, is reflected by the fiber end and travels through the cavity once again. In this way, a Fabry-Pérot cavity with a length l is formed between the polished end of an optical single mode fiber and the reflector. The reflected light finally produces an interference pattern that is detected by the photodetector D1.

3.2. PRINCIPLE OF OPERATION

In the setup of figure 3.2, the interference signal is detected at the detector D1 and is then routed to the evaluation circuit, where one of the two quadrature detection schemes is applied. The signal processing in the evaluation circuit is performed by a FPGA (field-programmable gate array). Depending on the selected scheme, the detector signal is either sent to a low-pass filter LPF and to a lock-in amplifier DEMOD1 demodulating at the frequency Ω ($0/\Omega$ quadrature scheme) or it is sent to two lock-in amplifiers DEMOD1 and DEMOD2, demodulating at the frequencies Ω and 2Ω , respectively ($\Omega/2\Omega$ quadrature scheme). The wavelength modulation $\delta\lambda$ results from a superposition of the constant laser current with a small current modulation. The current is modulated by means of an oscillator providing a voltage $V \cos(\Omega t)$. The two quadrature detection schemes are compared in figure 3.3, where the upper

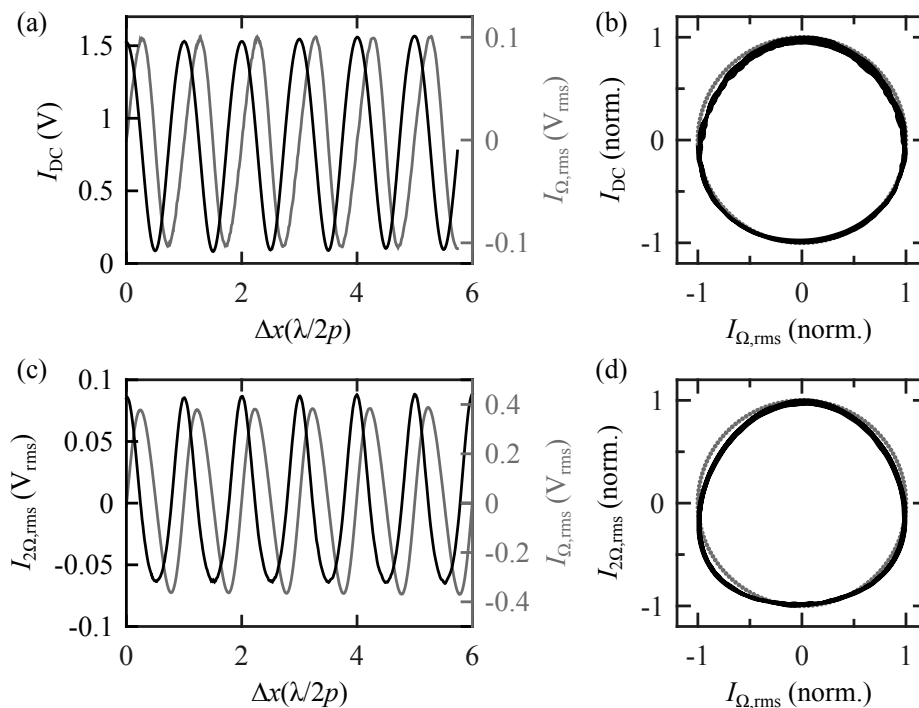


Figure 3.3: Comparison of two quadrature detection schemes applied to a low-finesse Fabry-Pérot interferometer. The first scheme (top) uses the filtered detector signal I_{DC} and the signal I_{Ω} , gained through demodulation at the frequency Ω , whereas the second scheme (bottom) uses the signals I_{Ω} and $I_{2\Omega}$, gained through demodulation at the frequencies Ω and 2Ω , respectively. (a) and (c) show the raw quadrature signals. (b) and (d) show the corresponding Lissajous figure after normalization of the raw signals. The deviation from a circle (gray line) results in periodic nonlinearities.

half refers to the $0/\Omega$ quadrature scheme and the lower half refers to the $\Omega/2\Omega$ quadra-

ture scheme. The raw signals of both schemes are shown in figure 3.3 (a) and (c). They were taken from a cavity with displacing target placed at a working distance of $WD = 20$ mm. The working distance is measured from the end of the sensor head to the target. In figure 3.3 (b) and (d), the raw signals are normalized and plotted against each other. In this way, a Lissajous figure is created, whose angle yields the interference phase Φ .

Fiber-optic Fabry-Pérot displacement interferometers are usually realized by a plane target which is placed in close vicinity to the optical fiber. Best interference signal contrast is achieved if the Fabry-Pérot mirrors have the same reflectivity, i.e. when the power reflected by the fiber end face equals the power which is coupled back from the cavity. Cavities suitable for high precision displacement tracking must further have a low-finesse in order to achieve a constant sensitivity over the whole measurement range. Normally, this kind of interferometer offers only a very short measurement range in the nanometer range when operated in the linear range of the interference pattern, where the detector signal increases linear with the position.[22] Exceeding the linear range of the interference pattern requires the use of a quadrature detection scheme. Since the interference intensity drops rapidly with increasing reflector separation due to the beam divergence of the light emitted from the fiber, the expansion of the measurement range beyond several microns can only be achieved by shaping the beam by means of lenses. The suitable beam shape crucially depends on the reflectivity of the target and on the measurement range. For long range measurements up to several meters, the beam must be collimated and the back reflected light must be reduced to about 4% of the incident power. This is achieved by using a plane glass target or a corner cube retro reflector which is offset with respect to the beam optical axis. The plane glass target requires a very precise alignment tolerance of ± 0.04 deg, but allows the simultaneous measurement of multiple directions of motion of an object. In contrast, the corner cube provides an acceptance angle of several degrees, but is limited to movements in only one-dimension. While a collimated beam which reflects off a high reflective plane target would saturate the detector at normal incidence, a convergent beam leads to good signal contrast if the target is defocused. This is, however, at the expense of measurement range. In this way, the presented interferometer can handle targets with various reflectivity and surface roughness. The various sensor head configurations will be described in detail in chapter 4.

3.2.1 Fiber optics

The fiber-optic circuit consists of different components which affect the optical power.[36] A simplified diagram of the fiber circuit is shown in figure 3.4. In the test setups used in this work, the fiber coupled components are interconnected either by FC (ferrule connector) connectors which are combined using mating sleeves or by fusion splicing. In case of FC connectors, all fiber ends, except the fiber end which forms the Fabry-Pérot cavity, have a 8° angled polish, also referred to as angled physical contact (APC), in order to reduce the back reflected light intensity (return loss is typically about 60 dB). The laser intensity launched into the circuit is designated I_0 . At first, the light passes an optical isolator ISO in order to protect the laser from any reflections (isolation is typically > 60.5 dB). Then, in most cases, an attenuator OA is required in order to reduce the optical power at the detector to $10 \mu\text{W}$ (the maximum detectable optical power of the detector circuit used in this work is limited to $10 \mu\text{W}$). The power damping of the attenuator or of any other optical part is given in dB according to

$$\text{Attenuation(dB)} = 10 \log \frac{P_{\text{out}}}{P_{\text{in}}}, \quad (3.1)$$

where P_{in} is the incident power and P_{out} is the output power. In the following, the attenuation of OA is assumed to be 0 dB. The light is then input into port P1 of the two-by-two directional fiber coupler and is split in two beams of equal intensity. One part of the light reaches output port P4, which ideally should absorb the entire incoming light. The other part of the light reaches output port P3 with an intensity of $I_0/2$ and is then routed to the cavity. At the polished fiber end, which is realized by a physical contact (PC) finish, the intensity $RI_0/2$ is reflected, where R is the reflectivity of the fiber end. The intensity $(1 - R)I_0/2$ is transmitted into the cavity. Maximum interference contrast is achieved when a total amount of $RI_0/2$ is also reflected by the cavity. Then, both parts recombine with a phase shift Φ and produce the phase dependent interference intensity $RI_0 \{1 + \cos \Phi\}$, which is again divided by two in the fiber coupler. At the end, only a small fraction $R \{1 + \cos(\Phi)\} I_0/2$ of the original laser intensity reaches the detector. In case of constructive interference, the detector power equals 4% or -14.0 dB of I_0 . An important parameter of the fiber coupler is the crosstalk between two input ports of a directional coupler, also referred to as directivity. It specifies the ratio between the power routed to the second input port P2 and the power launched in P1, according to $-10 \log (P_2/P_1)$.

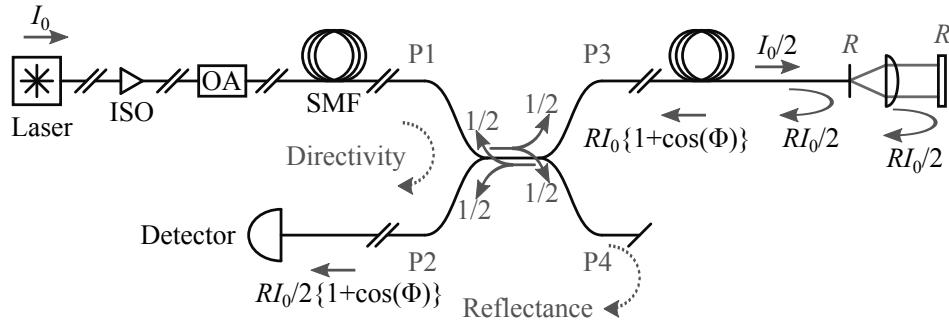


Figure 3.4: Fiber circuit diagram showing the intensities at different points of the circuit in case of equal reflectivities R of the Fabry-Pérot mirrors. The light from the laser is routed to the cavity via single mode fibers (SMF) and a fiber coupler and the reflected interference pattern is detected at the detector. The attenuation of the attenuator (OA) and the isolator (ISO) are not considered.

3.2.1.1 Laser

At the core of the system is a tunable distributed feedback (DFB) semiconductor laser, as shown in figure 3.5.[37] A summary of typical DFB laser diode specifications suitable for use in the present interferometer are provided in table 3.1. The laser is embedded in a standard 14-pin butterfly package with built-in thermoelectric cooler. The DFB laser has a number of advantages over external cavity diode lasers and over gas lasers like the helium-neon (HeNe) laser, which is often used for laser interferometry.[38] Compared to gas lasers, the emission wavelength of the DFB laser can be controlled by the laser current and temperature. This enables the use of a quadrature detection scheme based on the modulation of the laser wavelength, which simplifies the optical setup because the quadrature signal can be produced electronically. The large mode-hop free tuning range further allows the normalization of the quadrature signals upon system initialization and enables performing absolute distance measurements. However, this kind of semiconductor laser requires an external stabilization to a known wavelength reference in order to achieve a stability in the order of $\delta\lambda/\lambda = 10^{-8}$. The wavelength therefore has to match the spectral absorption range of the Acetylene 12 gas.[39] DFB lasers are available in all C-band ITU grid wavelengths. Wavelengths in the S-Band are rather uncommon and therefore more difficult to get. Best suited for wavelength stabilization is Acetylene 12 line P9 because of the high absorption depth. It has a wavelength of 1530.3711 nm, corresponding to the ITU grid line with a wavelength of 1530.33 nm or a photon frequency

3.2. PRINCIPLE OF OPERATION

Table 3.1: Summary of typical DFB laser diode specifications suitable for use in the present interferometer.

Optical output power	P_{opt}	5..100 mW
Wavelength tunability	$\partial\lambda/\partial T$	0.12 nm/K
Wavelength tuning range	$\Delta\lambda$	5.6 nm
Current tunability	$\partial\lambda/\partial I$	8 pm/mA
Current tuning range	$\Delta\lambda$	0.03 nm ⁽¹⁾
Spectral linewidth (FWHM)	$\Delta\nu$	1 MHz

¹ Measured for a current change of 20 mA using a 40 mW laser diode driven with 175 mA.

of 195.90 THz.

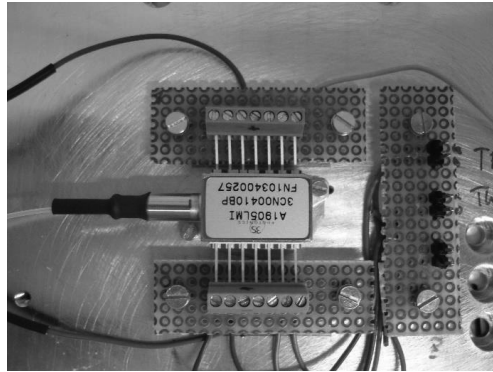


Figure 3.5: Fiber-coupled DFB Laser in a butterfly package with built-in thermoelectric cooler. The laser is thermally coupled to the ground plate for heat dissipation.

3.2.1.2 Detector

The detector consists of an InGaAs PIN photodiode and an amplifier circuit. Its specifications are summarized in table 3.2.

3.2.1.3 Noise sources

The fiber circuit has a significant influence on the noise characteristics of the interferometer. The total noise can be subdivided into noise originating from parasitic cavities and noise originating from the coupler directivity.

Parasitic cavities are formed between the interfaces of different fiber components which are reflecting part of the incoming light. The ratio of the reflected light power

Table 3.2: Summary of typical photodetector specifications suitable for use in the interferometer.

InGaAs PIN photodiode		
Cutoff frequency	f_c	2 GHz
Input power saturation	P_{sat}	10 mW
Bias voltage	U_{bias}	10..15 V
Noise equivalent power	NEP	$3 \cdot 10^{-15} \text{ W}/\sqrt{\text{Hz}}$

to the transmitted light power is designated as return loss. Parasitic cavities generate an interference pattern which is superimposed on the measurement signal. In some cases, the return loss can be further reduced by using an index matching material (e.g. a gel).

The second noise source is caused by the directivity of fiber couplers. Ideally, all of the light entering a directional coupler leaves it at the output ports. However, in real couplers part of the light is routed into the opposite direction and leaves the coupler at the second input port. This light interferes with the light reflected by the test cavity and contributes to the total noise level. The directivity of fiber couplers is typically specified greater than 65 dB. Its influence on the noise level can be roughly estimated. Therefore, two plane waves E_t and E_n are assumed.

$$E_t(x_t, t) = A_t e^{i(2kx_t - \omega t)} \quad (3.2)$$

$$E_n(x_n, t) = A_n e^{i(2kx_n - \omega t)}. \quad (3.3)$$

E_t represents the reflected interference signal which was generated by a displacement of the movable mirror. Its intensity is $RI_0/2(1 + \cos \Phi)$, which is RI_0 at maximum. E_n represents the signal that goes the direct way from the laser to the detector. It is described by the directivity, which is assumed to be 65 dB in the following, corresponding to a power ratio of $P_{\text{out}}/P_{\text{in}} = 0.3 \cdot 10^{-6}$. Superposition of both waves yields the intensity as a function of the mirror position and time, according to

$$\begin{aligned} I(x, t) &= |A_t \exp(ikx_t - i\omega t) + A_n \exp(ikx_n - i\omega t)|^2 = \\ &= \underbrace{|A_t|^2}_{\text{signal}} + |A_n|^2 + \underbrace{2|A_t||A_n| \cos\{kx_t - kx_n\}}_{\text{noise}}, \end{aligned} \quad (3.4)$$

where the first term represents the test signal produced by the displacing target and the third term represents the parasitic noise signal, which depends on the phase shift

3.2. PRINCIPLE OF OPERATION

between the two waves and on their polarization (not considered in this formula). The signal-to-noise ratio is then given by

$$\left(\frac{2|A_t||A_n| \cos \varphi}{|A_t|^2} \right)_{\max} = \frac{2|A_n|}{|A_t|} = 2\sqrt{\frac{0.3 \cdot 10^{-6} \cdot I_0}{RI_0}} = 5.5 \cdot 10^{-3}. \quad (3.5)$$

At maximum slope, the position equivalent noise amplitude according to equation 2.27 ($\Phi = \pi/4$) is 0.7 nm for the unfolded cavity and 1.3 nm for the folded cavity. This result shows that, even though the directivity is 65 dB, it produces a signal-to-noise level in the order of 10^{-3} .

The noise originating from the fiber circuit could in principle be reduced by rotating the polarization direction of the interference signal by 90° . For this purpose, the polarization rotator must be placed between the coupler and the cavity. Furthermore, all fibers are ideally polarization-maintaining in order to minimize the polarization rotation due to fiber birefringence. However, this would currently increase the price of the fiber circuit by a factor of about two. The fiber circuit can be tested experimentally with regard to parasitic cavities and coupler crosstalk by applying a wavelength ramp to the light which is coupled into the circuit. This would create resonances in the detector signal spectrum which scale with the cavity length.

3.2.2 Interferometer initialization

A proper initialization of the interferometer is essential for the correct operation. Before system initialization, the user needs to align the interferometer axis in such a way that the reflected beam is coupled back into the fiber and that the direction of the target movement is parallel to the laser beam. Since the laser beam is invisible, the interferometer system has a built-in red alignment laser which can help with the initial alignment of the setup. After that, the red laser is switched off and a fine adjustment of the setup is performed by means of optimizing the interference signal contrast. The setup is aligned in such a way that the interference signal has a maximum contrast and is constant over the entire measurement range. During this process, a low frequency (< 1 Hz) wavelength sweep with an amplitude of about 1 nm is applied to the laser by means of changing the laser temperature using the built-in Peltier cooler. This allows generating an interference pattern even under static conditions. The high frequency wavelength modulation needs to be switched off during this process in order not to change the amplitude of the interference signal. The same low frequency wavelength

sweep is used in the first initialization step to determine normalization values for the direct and demodulated signal, given by the maximum and minimum of both quadrature signals. These values are used to normalize the Lissajous figure. The arc tangent of both normalized signals finally yields the phase angle Φ . In the second step, the modulation amplitude is adjusted by means of increasing it from zero until a predefined demodulation value is reached. The low frequency wavelength sweep is again used to make sure the demodulation signal passes through its maximum and minimum value. In the last step, the wavelength is stabilized to a gas cell absorption line. This process is described in the following section.

3.2.3 Wavelength stabilization

The whole interferometer system is made more cost-effective by using telecom wavelength components operating in the short-wavelength infrared range. A central part of these components is the laser, whose wavelength stability determines an upper limit for the accuracy which can be achieved in a displacement measurement. Commercial laser displacement interferometers based on gas lasers (typically helium-neon lasers) usually achieve a long term laser stability of $\delta\lambda/\lambda = 2 \cdot 10^{-8}$. The laser used in this

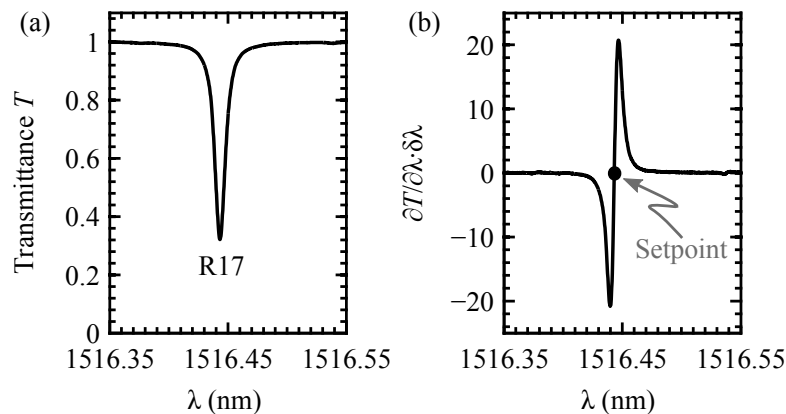


Figure 3.6: Laser wavelength stabilization. The laser wavelength is locked to the zero crossing of the gas cell demodulation signal at a specific absorption line of a molecular gas cell. (a) Transmittance T as a function of the wavelength λ around absorption line R(17) of Acetylene 12. (b) Corresponding wavelength demodulated signal.

work is a semiconductor DFB laser diode. In such lasers, the wavelength is sensitive to the laser temperature and current. This requires an external stabilization of the wavelength to a known reference in order to achieve a wavelength stability in the order

3.2. PRINCIPLE OF OPERATION

of $\delta\lambda/\lambda = 10^{-8}$. In this work, this is realized by locking the laser wavelength actively to a certain absorption line of a low-pressure Acetylene 12 molecular absorption gas cell. These lines are known with an uncertainty down to $\delta\lambda = 0.1$ pm.[39] The gas is inside a glass tube and has a pressure of 50 Torr (≈ 67 mbar). The tube has a length of 55 mm. The temperature dependence of the absorption lines is < 0.01 pm/K.

In practice, the laser current and temperature of the DFB laser are controlled by a wavelength control circuit (λ Control), which achieves a long-term frequency stability of typically 100 MHz peak-to-peak (Toptica DL DFB), corresponding to $\delta\lambda/\lambda = 5 \cdot 10^{-7}$. The laser temperature control can hold the laser wavelength within a temperature control interval δT , but not within the required wavelength stability and accuracy. In order to increase the stability, a feedback loop (PID) in the wavelength stabilization circuit, shown in figure 3.2, locks the laser wavelength to the zero crossing of the gas cell demodulation signal by controlling the more sensitive laser current, which is the control variable in this process. The zero crossing of the demodulation signal has the same wavelength as the absorption minimum. In contrast to the direct gas cell signal, the demodulation signal can serve as a process variable in the feedback loop because of the nonzero slope around the absorption minimum. The controller output is determined by a comparator which calculates the difference between the demodulation signal and the setpoint zero. The demodulation signal is provided by the lock-in amplifier DEMOD 3, which demodulates the signal from detector D2 at the frequency Ω . Figure 3.6 (a) exemplary shows the low-pass filtered absorption signal around absorption line R(17) of Acetylene 12. The corresponding wavelength demodulated signal, which is gained through demodulation of the absorption signal, is shown in figure 3.6 (b). The width of this line, measured from minimum to maximum, is typically around 7 pm. The wavelength information for this plot was gained through interpolation of the wavelength between the known absorption lines by means of the phase signal from a cavity with fixed length. With this stabilization technique a wavelength stability in the order of $\delta\lambda/\lambda = 5 \cdot 10^{-8}$ is achieved.

In order to produce defined wavelength shifts, the laser wavelength λ can be locked to different absorption lines of the molecular absorption gas cell. Figure 3.7 exemplary shows the wavelength sweep demodulation signal of an Acetylene 12 molecular absorption gas cell when changing the laser temperature from $T_1 = 16.6^\circ\text{C}$ to $T_2 = 30.3^\circ\text{C}$, resulting in a wavelength shift from line P(17) ($\lambda = 1535.3928$ nm) to P(19) ($\lambda = 1536.7126$ nm).

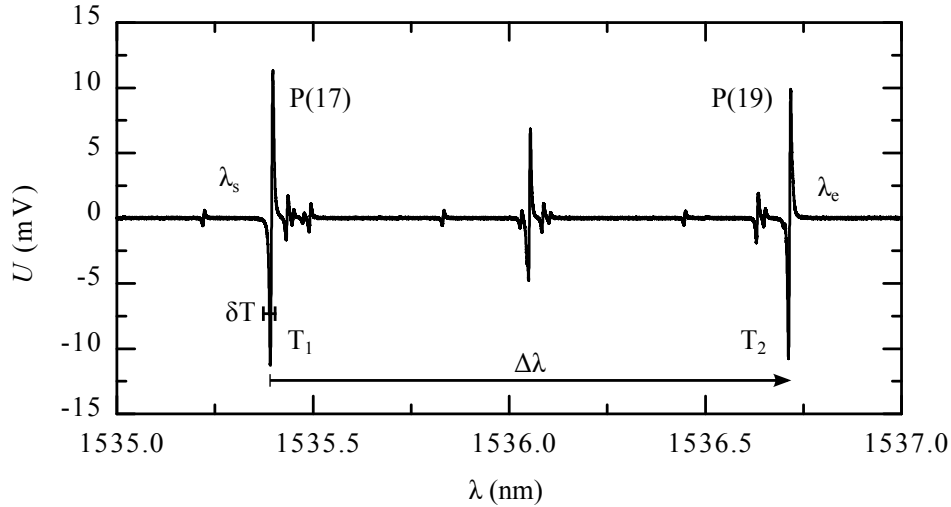


Figure 3.7: Wavelength sweep demodulator voltage U as a function of the wavelength λ of an Acetylene 12 molecular absorption gas cell. The laser temperature was increased from $T_1 = 16.6^\circ\text{C}$ to $T_2 = 30.3^\circ\text{C}$, corresponding to a wavelength shift of $\Delta\lambda = 1.3198$ nm.

3.3 Real-time interfacing

A central point of the interferometer system is the real-time interface which is responsible for the transmission of the position data. Inside the FPGA, the target position is measured with a bandwidth of 10 MHz (measurement bandwidth) and the position is encoded as 48 bit long serial word with a resolution of 1 pm. Outputting the position with full precision at maximum bandwidth would require an interface operating with a clock rate of at least $10 \text{ MHz} \cdot 48 = 480 \text{ MHz}$. However, the real-time interface provides a maximum output bit rate of only $\text{BitRate} = 25 \text{ MHz}$ (interface bandwidth). This means that, in practice, a compromise needs to be found for each application. For this reason, the real-time interface supports different serial and incremental protocols. Each format has its advantages and disadvantages which are described in the following sections. The latency between target movement and data transmission in the interferometer system is typically in the order of $1 - 2 \mu\text{s}$. In this work, the data were recorded using a 25 MHz digital I/O board (National Instruments PCIe-6536B) for continuously streaming data over the PCI Express bus of a computer. A shielded connector block (National Instruments BNC-2110) simplifies the connection of the digital signals.

3.3.1 Serial interface (HSSL)

The HSSL (High Speed Serial Link) interface enables the transmission of digital words (absolute displacement information) with user defined length and resolution using a binary serial format which is provided with one of two different signaling standards single-ended LVTTTL or differential LVDS.[40] HSSL is a synchronous protocol with two signal lines clock and data, whereby the data are synchronized with the rising edge of the clock signal. Figure 3.8 shows an example for the HSSL signal. The

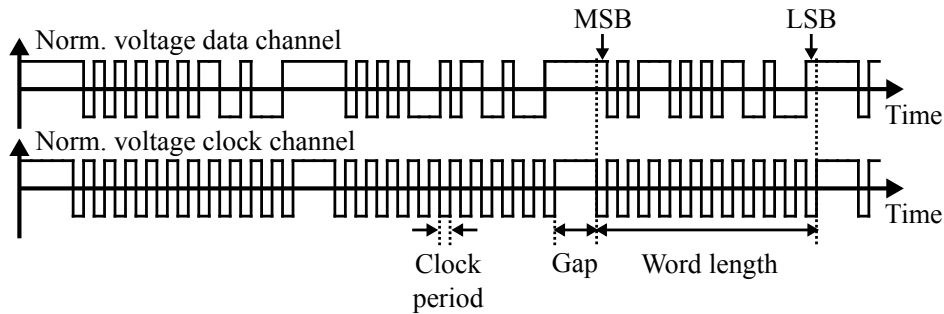


Figure 3.8: Illustration of the HSSL digital serial interface signals. The position value is encoded as a serial word with user adjustable *LSB* (least significant bit) and *MSB* (most significant bit).

HSSL data format is 48 bit signed with a resolution of 1 pm, starting with the most significant bit (*MSB* or high-order bit), i.e. the bit position which has the greatest value. The *LSB* (least significant bit) is the bit position having the smallest value, thus defining the units value respectively the position resolution of the transferred word. The bit position number of the *MSB* and *LSB* is ranging from 0 to 47. Both the *MSB* and the *LSB* position can be configured by the user in order to reduce the word length and to increase the data rate. The position resolution is given by

$$Resolution = 2^{LSB} \cdot 1 \text{ pm.} \quad (3.6)$$

The maximum transferable position range is given by

$$Range = 2^{MSB+1} \cdot 1 \text{ pm.} \quad (3.7)$$

The HSSL protocol is also defined by its bit rate, which can be adjusted as a multiple of the interface clock period or bit transmission time $Clock = 40 \text{ ns} = 1/BitRate$ by the user. Between two sets of position information, the clock signal is left out for some user adjustable multiples of the bit transmission time (referred to as gap bits),

thus allowing the synchronization of reader and sender within a continuous stream of position information. Consequently, the final data rate or repetition rate is given by

$$DataRate = (MSB - LSB + 1 + GapBits) \cdot BitRate. \quad (3.8)$$

The advantage of this protocol is that positions can be transferred in absolute values, thus promoting measurements requiring a large travel range and at the same time a high resolution. The disadvantage is the relatively slow data rate which makes HSSL unsuitable for measurements at higher frequencies.

3.3.2 Quadrature interface (A-quad-B)

The digital quadrature interface (A-quad-B) provides incremental position information with user defined resolution and clock period. Both resolution and clock period can be adjusted in multiples of 1 pm and 40 ns, respectively. Two digital two-level channels A and B are used to encode the position information, thus allowing to transmit both the target displacement and its direction. The amplitude levels are either LVTTTL (single-ended) or LVDS (differential). Plotting both channels A and B against each other creates a square, as illustrated in figure 3.9. A change of position is transformed into a stepping through the four possible states of the A and B quadrature signals, represented by the edges of the square. In this picture, a signal change of 90° represents, depending on the direction, a displacement of $\pm Resolution$. The A-quad-B protocol is best suited for measurements at high frequencies because the data rate is directly given by the interface bandwidth. However, the transmittable velocity is limited by

$$v_{\max} = Resolution/Clock. \quad (3.9)$$

Above this maximum velocity, the position data present in the FPGA require more time to be transmitted, which can be interpreted as a low-pass filtering of the data. The high data rate makes A-quad-B best suited for measurements at high frequency but with small amplitude, as it is the case in vibration or run-out measurements. However, great care has to be taken with the choice of the resolution. When it is too low there might be a conflict with the maximum velocity, resulting in a distortion of the transferred data.

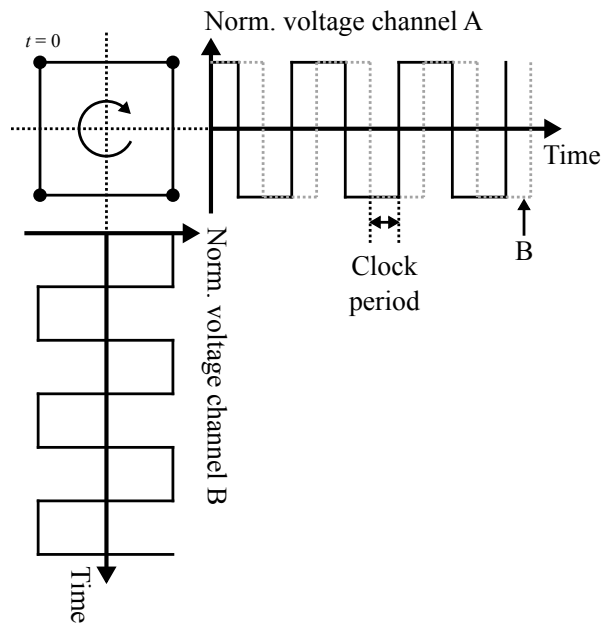


Figure 3.9: Illustration of the A-quad-B digital quadrature interface signals. Plotting both Channel A and B against each other creates a square. A rotation of 90° in the square corresponds to a position change in accordance with the value of one resolution.

3.3.3 Analog Sine/Cosine

A widely used signal standard for incremental position encoders is the analog Sine/Cosine interface.[41] The sine and cosine signals are synthesized from the 48 bit digital word information present in the FPGA. The implementation is very similar to the A-quad-B interface, with the difference that the signal square is a circle with intermediate points between the four states of the A-quad-B signal.

3.4 Measuring systems

During this work, different types of the interferometer have been developed and successfully launched on the market.

3.4.1 attoFPSensor

The first commercial attocube Fabry-Pérot interferometer system was delivered in the year 2010. It is a 19" rack system, as shown in figure 3.10, consisting of three different components, the laser controller, the evaluation electronic unit and the optical

component carrier. The laser controller is a Toptica “SYST DL DFB BFY” including a “DCB 110” analog interface board for laser temperature control by means of an external voltage signal and a “DL-MOD/DFB” high frequency modulation printed circuit board for laser wavelength modulation. The DL-MOD/DFB module is based on a field-effect transistor (FET) enabling to modulate the laser current by means of an external oscillator, resulting in a modulation of the wavelength. The FPGA based evaluation electronic unit is an attocube “AMC500” (attocube metrology controller, developed by n-Hands GmbH & CO. KG) which contains the lock-in amplifiers for demodulation of the interference signal, the wavelength stabilization PID controller, and the position evaluation unit. The optical component carrier is an attocube “ACC200” which contains all optical parts, including the DFB laser (Toptica “DL DFB BFY” laser head), detectors, gas cell, isolator, fiber couplers, and attenuators. The AMC500 provides an oscillator voltage output for laser wavelength modulation, an analog voltage output for controlling the laser temperature and one voltage input for each detector signal. The integrated PID controller further provides an analog voltage output for controlling the laser current and a voltage input for the gas cell detector signal. The three components in the attoFPSensor are interconnected by means of BNC cables. The PID controller output and the temperature control output of the AMC500 are connected to the laser current control module and to the current control module of the Toptica laser controller, respectively. The AMC500 oscillator output is connected to the laser FET input of the Toptica laser head. The strength of the attoFPSensor system lies, on the one hand, in the large number of parameters which can be accessed and controlled by the user, and on the other hand in the versatility of the optical components. Different configurations of the fiber circuit can be easily realized through interconnection of fiber coupled components, whereby the use of optical parts with FC/APC connectors enables interconnection with low back reflection. The attoFPSensor is well suited to handle a large number of independent interferometer axes and requires only one laser source. In this way, the operation of up to 12 axes has been successfully demonstrated.

3.4.2 FPS3010

The second interferometer system, the FPS3010 (see figure 3.11), was launched in November 2011. It combines all parts of the attoFPSensor in only one compact housing with a size of 21.4 x 21.4 x 4.5 cm³ and enables the simultaneous detection

3.4. MEASURING SYSTEMS

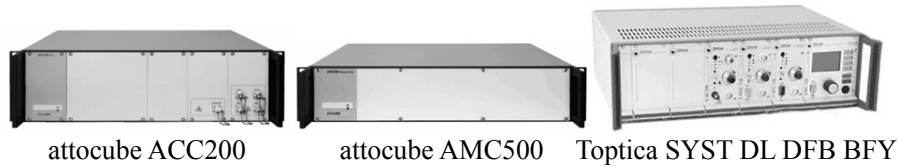


Figure 3.10: attoFPSensor real time interferometric sensor, consisting of the laser controller (Toptica SYST DL DFB BFY), the evaluation electronic unit (AMC500) and the optical component carrier (ACC200).

of the displacement of up to three independent interferometer axes with a digital resolution of 1 pm. Large effort has been put into improving the user-friendliness, which was achieved by adding functionalities such as an automatic adjustment of the demodulator phase, a continuous wavelength sweep during the alignment process of the setup allowing to monitor the interference contrast, an automatic normalization of the quadrature signals upon start-up, and an automatic wavelength stabilization process. The FPS3010 is also the first attocube interferometer which was offered with an environmental compensation unit (ECU) in order to compensate for the refractive index of air. In 2012, the FPS3010 received the R&D100 Award 2012, celebrating the top 100 technology products of the year.



Figure 3.11: FPS3010 real time interferometric sensor. The FPS3010 enables the simultaneous detection of position variations of three targets with picometer resolution up to a working distance of 3 m.

3.4.3 IDS3010

In November 2014, attocube launched the IDS3010, which is the first OEM (original equipment manufacturer) interferometer on the market. The IDS3010 is an ultra-compact three-axis fiber-based interferometer with a size of 5.0 x 5.5 x 19.5 cm³. It can be used in complex machine tools or lithography systems to control the stage position with nanometer accuracy and is meant for direct machine integration.[42] The IDS3010 continues the improvement of the user-friendliness started with in the



Figure 3.12: Industrial Distance Sensor IDS3010 for OEM displacement sensing. It was designed for direct machine integration.

FPS3010. It provides an open-loop control of the phase adjustment by means of the current displacement. Furthermore, the IDS3010 was the first to include an absolute distance functionality with an uncertainty of about $\pm 10 \mu\text{m}$. This absolute position information is used for automatic open-loop control of the wavelength modulation amplitude and as an input for the refractive index correction (see section 3.8). A manual measurement of the target distance is therefore no longer necessary.

3.5 System performance

In this section, the system performance is characterized with respect to its position repeatability, resolution, sensitivity, and accuracy on the basis of measurements and calculations. All of the following measurements have been performed using the DC/ Ω quadrature scheme. The resulting specifications are summarized in figure 3.1.

3.5.1 Stability

The repeatability of the interferometer is characterized by its long term stability. In order not to falsify the measurement by thermal drifts originating from the cavity, the cavity was cooled down to liquid helium temperature (4 K). Figure 3.13 shows the

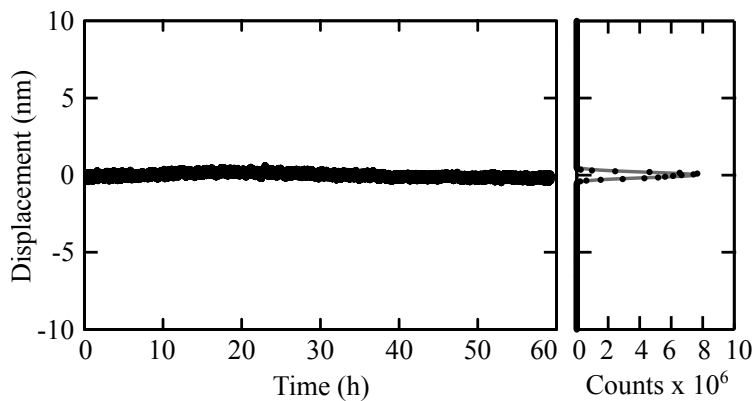


Figure 3.13: Interferometer long-term stability and histogram plot measured with the IDS3010 using an Invar (FeNi36) cavity which was cooled down to liquid helium temperature (4 K). The data were recorded at a cavity length of 77 mm (single pass) and a bandwidth of 100 Hz.

long term position stability of a cavity with a length of $l = 77$ mm over 60 hours and the corresponding histogram plot indicating a Gaussian distribution of the position noise with a standard deviation of $3\sigma = 0.45$ nm. The signal stability corresponds to a wavelength stability of $\Delta\lambda/\lambda = \sigma/l = 5.8 \cdot 10^{-9}$ and complies with the stability of gas lasers used in commercial displacement interferometers, which is typically in the order of $\delta\lambda/\lambda = 10^{-8}$. The data were taken with a bandwidth of 100 Hz and transmitted with a clock time of 200 ns (5 MHz) via HSSL. The position noise mainly originates from wavelength noise and spurious interferences within the fiber circuit.

3.5.2 Phase dependency of the position noise

Other measurements of the stability with similar cavities, however, revealed significantly different noise levels. The reason for these differences lies in a dependency of the noise on the interference phase or on the actual position in the Lissajous figure. This behavior is demonstrated in figure 3.14. The noise is maximum when the filtered signal is maximum and minimum when the filtered signal is minimum. Additionally, the noise is increased at phases corresponding to multiples of the $\pi/4$. At these points, the total noise is the sum of the DC and Ω signal.

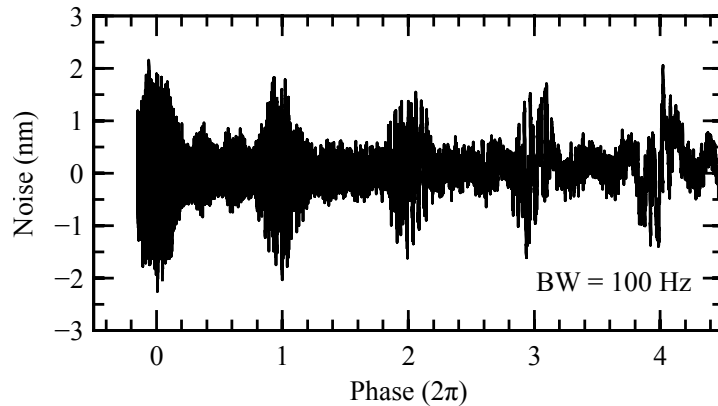


Figure 3.14: Displacement noise measured with the attoFPSensor as a function of the interference phase. The data were taken at a working distance of 38 mm (72 mm cavity length) using a drifting aluminum double pass cavity around room temperature.

3.5.3 Bandwidth dependence of the position noise

So far, the noise level has only been shown for a bandwidth of 100 Hz. Different bandwidths and cavity lengths, however, lead to different noise levels. In order to demonstrate the noise dependence from these parameters, the position noise standard deviation (3σ) was determined at two different cavity lengths, $WD = 20$ mm and $WD = 50$ mm, and at a bandwidth ranging from 10 Hz to 400 kHz. The results in figure 3.15, measured with the FPS3010, show that the noise increases with the square root of the measurement bandwidth, similar to the shot noise.[43] A second conclusion that can be drawn is that the noise is larger for shorter cavities. This comes from the smaller modulation depth at shorter cavity lengths, which increases the noise of the demodulator.

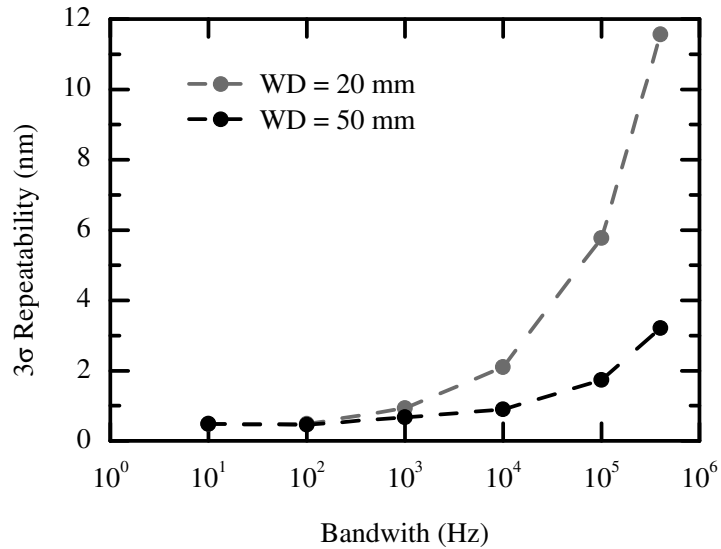


Figure 3.15: Standard deviation (3σ) of the position data measured with the FPS3010 as a function of the measurement bandwidth for two different working distances WD .

3.5.4 Noise spectral density

The spectral resolution of the interferometer, which is often of interest when performing vibration measurements, is gained by Fourier transformation of the position signal. The position noise spectral density measured with the FPS3010 is shown in figure 3.16, demonstrating a noise floor of about $6 \text{ pm}/\sqrt{\text{Hz}}$ for a measurement taken at the full bandwidth of 10 MHz. In order to achieve the highest possible frequencies, the data were transmitted via A-quadrant-B with a clock time of 200 ns (5 MHz) and the four different resolutions 1 pm, 10 pm, 100 pm and 1000 pm. Interestingly, the data start to roll-off from a certain frequency, which is higher the larger the resolution of the A-quadrant-B signal is. It is noteworthy that the product of the cut-off frequency and the A-quadrant-B resolution is constant for one data set. The reason for this roll-off lies in the noise floor which is also transferred into an output signal of the A-quadrant-B interface and, in this way, increases the load of the interface. This load is the higher the smaller the resolution of the A-quadrant-B interface is and is responsible for the low-pass filtering of the position data.

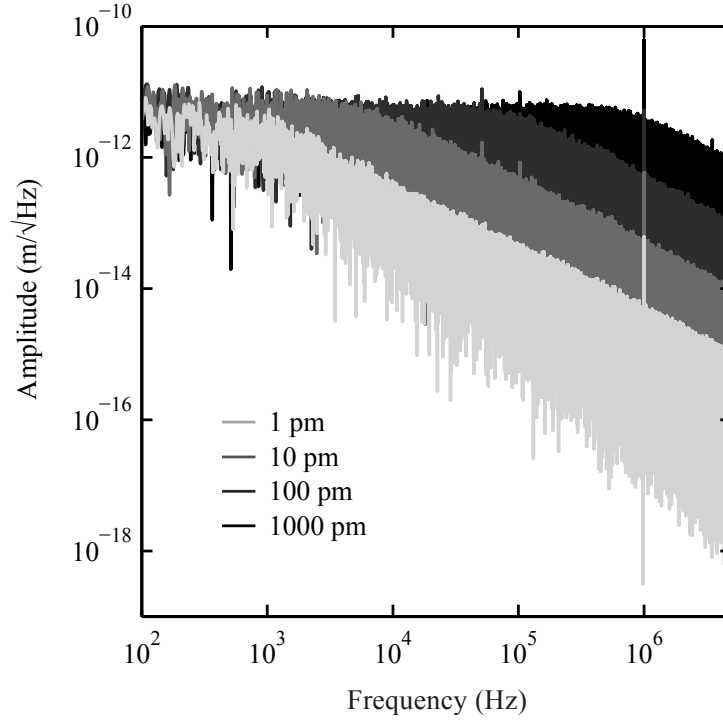


Figure 3.16: Noise spectral density measured with the FPS3010 and a cavity with a length of about 60 mm. The data were transmitted via A-quadrant with a clock time of 200 ns (5 MHz) and the four different resolutions 1 pm, 10 pm, 100 pm and 1000 pm.

3.5.5 Fiber circuit noise

As already mentioned, the noise partly arises from spurious interferences within the fiber circuit, which correspond to parasitic cavities with a length that is typically much longer than the cavity under test. It follows that, by reducing the coherence length of the laser source, these spurious interferences could in principle be reduced. The wavelength modulation inherent to the presented interferometer effectively broadens the linewidth of the laser from about 1 MHz to 0.1 GHz, which reduces the coherence length from about 300 m to 3 m. The coherence length is given by

$$l_c = \frac{c}{\delta\nu} \approx \frac{\lambda^2}{\delta\lambda}, \quad (3.10)$$

where $\delta\nu$ is the laser frequency linewidth and $\delta\lambda$ is the laser wavelength linewidth.[30] In fact, figure 3.17 shows a reduction of the noise when the wavelength modulation is turned on. It shows the laser noise change of the filtered detector signal around the quadrature point when switching off and on the wavelength modulation.

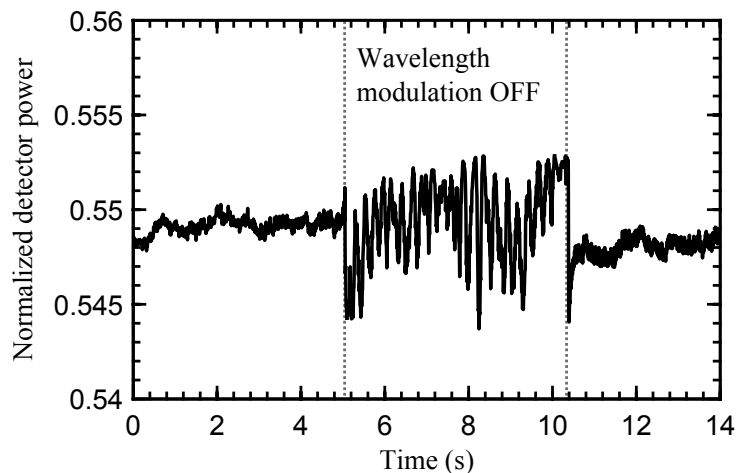


Figure 3.17: Influence of the wavelength modulation on the filtered interference signal noise around the maximum slope. The modulation shortens the coherence length of the light and thus reduces spurious interferences produced in the fiber circuit.

3.6 Nonlinearities

The accuracy of interferometric measurement techniques is mainly limited by periodic nonlinearities, which means that the measured displacement differs periodically from the real displacement. In the Michelson interferometer, these nonlinearities arise mainly from polarization mixing in the homodyne case [44, 45] and from frequency mixing in the heterodyne case.[46, 47] Polarization mixing results from imperfections in polarizing beam splitters and wave plates, preventing a complete separation of orthogonal polarization states. Frequency mixing results from a cross talk between the frequencies of two linearly polarized beams.[48] The periodic phase nonlinearities inherent to the presented interferometer can be subdivided into contributions arising from multiple reflections in the Fabry-Pérot cavity, from a non-sinusoidal time modulation and from an incorrect normalization.

The first source of nonlinearities are periodic phase nonlinearities arising from multiple reflections in the Fabry-Pérot cavity. These intrinsic nonlinearities have a phase periodicity of 2π and limit the accuracy of the displacement measurements to several nanometers. They depend on the finesse of the cavity, on the fiber coupling efficiency and also on the underlying quadrature scheme. The measured nonlinearities for the two different quadrature schemes are shown in figure 3.18 and compared to calculations. Figure 3.18 (a) depicts the Lissajous figure representation of the signals

measured with the $0/\Omega$ quadrature scheme and (b) shows the corresponding nonlinearities as a function of the relative displacement. Figure 3.18 (c) and (d) shows the same signals for the $\Omega/2\Omega$ quadrature scheme. Black and gray lines represent measured and calculated values, respectively. The nonlinearities are extracted by calculating the unwrapped phase angle in the normalized Lissajous figure according to equation 2.43, followed by subtracting a monotonous fit function. The data show a good agreement between measurement and calculation. The theoretical nonlinearities of the $0/\Omega$ quadrature scheme are within ± 4.9 nm and within ± 17.0 nm in the $\Omega/2\Omega$ quadrature scheme. The high reproducibility of the nonlinearities enables their correction by means of a look-up table deposited in the position processor. In this way, the accuracy of the interferometer can be enhanced up to 1 nm.

A second source of periodic phase nonlinearities is related to the transfer function between the oscillator and demodulator. A nonlinear transfer function of the high frequency laser modulation electronic circuit causes a non-sinusoidal time dependent modulation of the laser wavelength and results in 2π -periodic phase nonlinearities.

A third source of periodic phase nonlinearities is related to the normalization of the quadrature signals. The use of incorrect normalization values (maximum and minimum of the quadrature signals) leads to a deviation of the Lissajous figure from the unit circle and causes 2π -periodic phase nonlinearities.

3.7 Velocity and vibration tracking

In many applications, such as wafer alignment in semiconductor manufacturing, speed plays a key role and often requires fast displacement tracking. The interferometer achieves a large measurement speed by fast wavelength modulation with 12.5 MHz. Dynamic measurements with the presented interferometer are limited to a maximum target speed of $v_{\max} = 2$ m/s. This is due to the maximum measurement bandwidth of 10 MHz and the condition that unambiguous displacement determination is only possible when the target is displaced by less than $\Delta\Phi = \pi/2$ within the time interval $\Delta t = 1/10$ MHz. Figure 3.19 (a) and (b) show the displacement of a linear magnetic drive with a peak velocity of 2 m/s and a stroke of 1 m.

The same rules for the velocity apply to vibrations of the target. Assuming a target position oscillation of $\Delta x(t) = d \cdot \cos(\omega t)$ with amplitude d and angular frequency $\omega = 2\pi f$, the maximum velocity is given by $v_{\max} = (\partial x / \partial t)_{\max} = d \cdot \omega$. The maximum

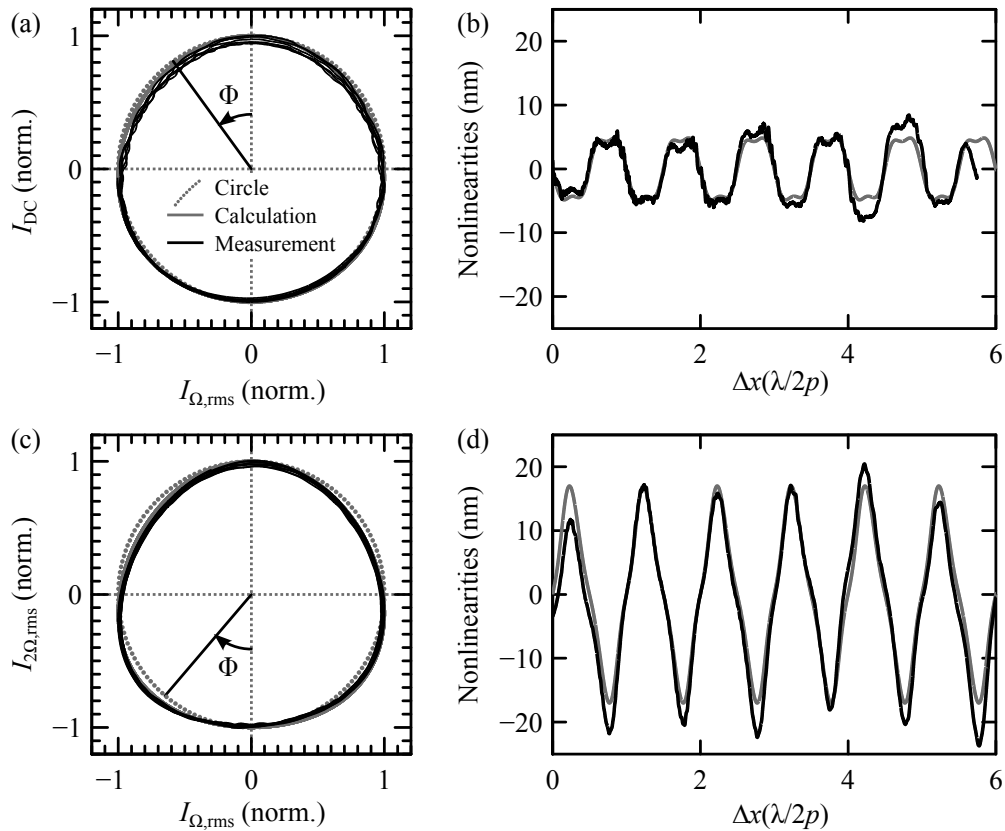


Figure 3.18: Comparison of two quadrature detection schemes applied to a low-finesse Fabry-Pérot interferometer. The first scheme (top) uses the filtered detector signal I_{DC} and the demodulated signal I_{Ω} , whereas the second scheme (bottom) uses the signals I_{Ω} and $I_{2\Omega}$, gained through demodulation at the modulation frequencies Ω and 2Ω , respectively. (a) and (c) show the normalized quadrature signals in the Lissajous figure representation. The deviation from a circle (dashed line) results in periodic nonlinearities which are shown in (b) and (d).

detectable vibration frequency is then given by $\omega = v_{\max}/d$. Figure 3.19 (c) and (d) show the detection of high and low amplitude vibrations of a piezoelectric ceramic oscillating with a frequency of 5 Hz. The displacement spectrum demonstrates the ability of the interferometer to detect vibrations with picometer amplitude (d) and vibrations with an amplitude that exceeds the linear range of the interference pattern (c). The data were taken with a bandwidth of 1 kHz.

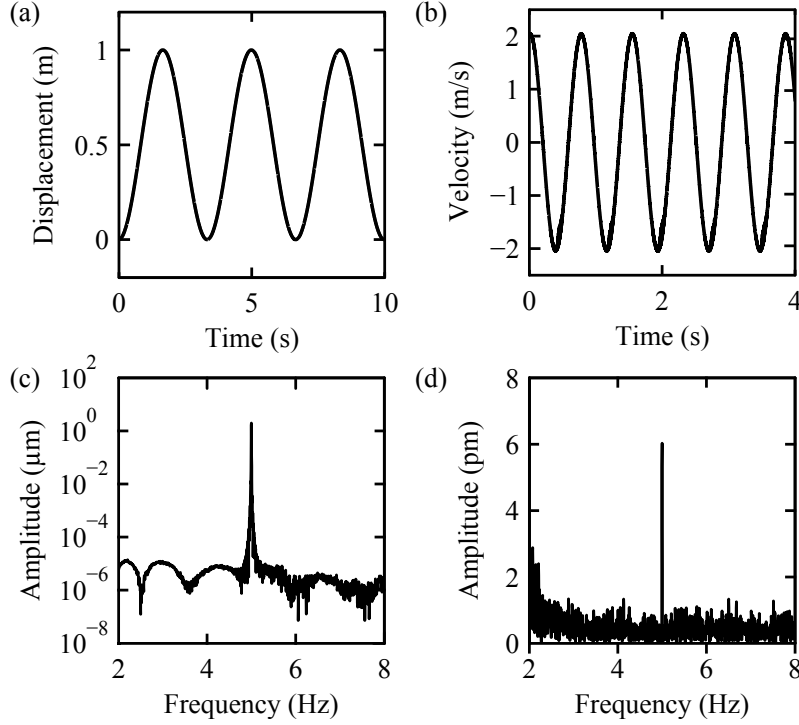


Figure 3.19: Top: High speed position detection of a linear magnetic drive moving with a stroke of 20 mm (a) and a maximum velocity of 1 m/s (b). Bottom: Detection of high (c) and low (d) amplitude vibrations of a piezoelectric ceramic oscillating with a frequency of 5 Hz.

3.8 Ambient environment compensation

The greatest challenge of today's interferometric position sensing is the operation at ambient conditions. When performing accurate interferometric absolute or relative position measurements at ambient conditions, the refractive index n of the medium inside the cavity must be taken into account. Changes of the refractive index are causing a phase shift $\Delta\Phi_{\text{amb}}$ with respect to the vacuum level, according to

$$\Delta\Phi_{\text{amb}} = \Phi_{\text{air}} - \Phi_{\text{vac}} = \frac{4\pi px}{\lambda}(n - 1), \quad (3.11)$$

where Φ_{air} is the phase measured in air and Φ_{vac} is the phase measured in a vacuum. This phase change falsifies the measurement result and must be compensated in order enable interferometry to compete with other position sensing techniques, such as linear scale encoders. All relative and absolute position measurements consequently rely on the accurate knowledge of the refractive index. In this context, the Fabry-Pérot interferometer reveals a great advantage in comparison with the Michelson

interferometer. In the Michelson interferometer, a change of the refractive index in the reference arm affects the measurement accuracy. Because of its common path structure, meaning that there is no reference beam, the Fabry-Pérot interferometer is insensitive to those refractive index differences.[7]

In order to correct for dynamic fluctuations of the refractive index in the relative displacement measurement described by equation 2.44, the time dependent refractive index $n_2(t)$ has to be considered. The corrected displacement measured when moving the target from position x_1 to $x_2(t)$ is then given by

$$\begin{aligned}
 \Delta x(t) &= x_2(t) - x_1 \\
 &= \frac{\Phi_2(t)}{2pk n_2(t)} - \frac{\Phi_1}{2pk n_1} \\
 &= \frac{\Phi_1 + \Delta\Phi(t)}{2pk n_2(t)} - \frac{\Phi_1}{2pk n_1} \\
 &= x_1 \left(\frac{n_1}{n_2(t)} - 1 \right) + \frac{\Delta\Phi(t)}{2pk n_2(t)},
 \end{aligned} \tag{3.12}$$

where Φ_1 and n_1 are the phase and the refractive index at the start position, and $\Phi_2 = \Phi_1 + \Delta\Phi(t)$ and n_2 are the phase and the refractive index at the end position. The equation shows that the environmental compensation requires the accurate knowledge of the absolute cavity length x_1 . Yet again, the advantage of the diode based interferometer becomes apparent. While in conventional gas laser based interferometers the distance needs to be determined by the user, the interferometer presented here enables an automatic absolute distance measurement based on a sweep of the laser wavelength (see section 5.1.1.1). This improves both the user-friendliness and the accuracy of the compensation. Particular attention must be paid in case the cavity contains a lens for beam shaping. In this case, the lens thickness must be subtracted from the cavity length.

Here, two special cases can be distinguished, constant cavity length and constant refractive index.

1. In case that the refractive index does not change during operation, meaning that $n_1 = n_2(t) = n$, the accurate measurement of the displacement does not require the knowledge of the absolute distance. The displacement is consequently directly deduced from the phase change $\Delta\Phi(t)$ according to

$$\Delta x(t) = x_2(t) - x_1 = \frac{\Delta\Phi(t)}{2pk n}. \tag{3.13}$$

In some applications with constant temperature, pressure and humidity or for short term measurements it might be sufficient to assume a constant refractive index.

2. In case of a constant cavity length x , i.e. $\Delta x(t) = 0$, the phase change $\Delta\Phi$ directly indicates the refractive index change due to a change of the air parameters.

$$\begin{aligned} n_2(t) &= n_1 \left(1 + \frac{\Delta\Phi}{\Phi_1} \right) \\ \Delta n(t) &= n_2(t) - n_1 = \Delta\Phi \frac{\lambda}{4p\pi x_1} \end{aligned} \quad (3.14)$$

This direct relation between phase change and refractive index can be used to specify the extend of refractive index correction achieved by the air compensation unit. However, this requires the knowledge of the absolute distance x .

This section considers two methods for the compensation of the refractive index. The first one, referred to as weather station, is based on measuring temperature, pressure, humidity and CO₂ content of the air and on deriving the refractive index from a dispersion formula. The second one measures directly the refractive index using an interference refractometer.

3.8.1 Weather station

A so called weather station corrects for the refractive index by measuring the physical parameters of the atmosphere. The relevant physical parameters are the temperature T , pressure p , humidity h and CO₂ content x_c of the air. For operation, the weather station must be brought in close vicinity to the measurement beam. The relative measurement error generated by the refractive index is in general expressed by

$$\delta x = \frac{x}{n} \left(\frac{\partial n}{\partial T} \delta T + \frac{\partial n}{\partial p} \delta p + \frac{\partial n}{\partial h} \delta h + \frac{\partial n}{\partial x_c} \delta x_c \right). \quad (3.15)$$

In order to calculate the refractive index from these air parameters, Ciddor developed equations for the visible and near infrared spectral range,[49] which connect the physical parameters of the air with the refractive index. The equations claim

3.8. AMBIENT ENVIRONMENT COMPENSATION

to provide an uncertainty of $\pm 5 \cdot 10^{-8}$. [50] In practice, the uncertainty is not better than $\pm 8 \cdot 10^{-8}$. [51, 52] According to the Ciddor equation, the refractive index at $T = 20^\circ\text{C}$, $p = 1013 \text{ mbar}$, 50% relative humidity and a CO_2 content of 400 ppm is $n = 1.000268091$ ($\lambda = 1530 \text{ nm}$). The dependence of the refractive index from temperature, pressure, wavelength, humidity and CO_2 content around these preconditions is analyzed using the Ciddor equation and summarized in table 3.3.

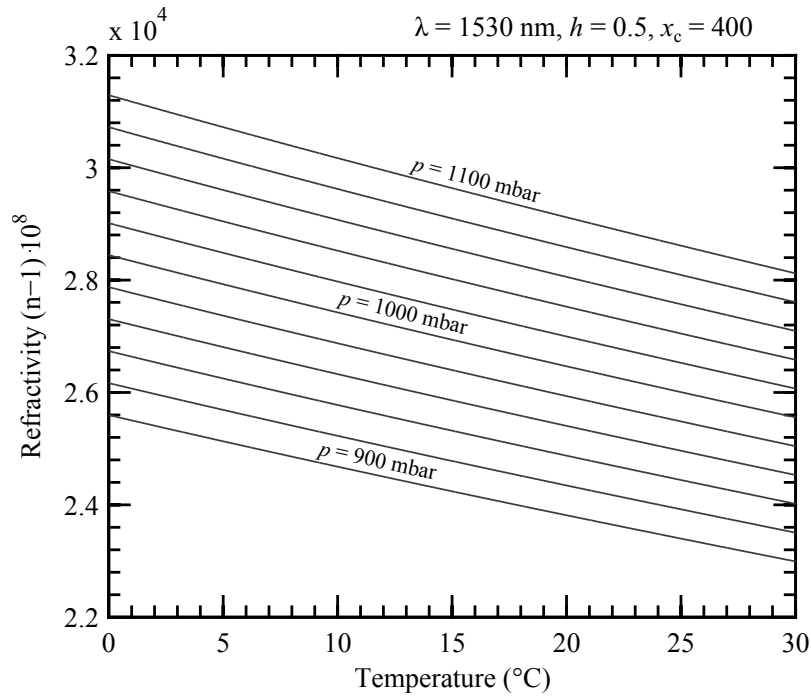


Figure 3.20: Refractivity of air as a function of the temperature T at different pressures p . The data were calculated using the Ciddor equation evaluated for a wavelength of $\lambda = 1530 \text{ nm}$, a humidity of $h = 50\%$, and a CO_2 content of $x_c = 400 \text{ ppm}$.

Temperature T	$dn/dT \text{ (K}^{-1}\text{)}$	$-9.32 \cdot 10^{-7}$
Pressure p	$dn/dp \text{ (mbar}^{-1}\text{)}$	$2.70 \cdot 10^{-7}$
Humidity h	$dn/dh \text{ (\%}^{-1}\text{)}$	$-8.72 \cdot 10^{-9}$
CO_2 content x_c	$dn/dx_c \text{ (ppm}^{-1}\text{)}$	$1.42 \cdot 10^{-10}$
Wavelength λ	$dn/d\lambda \text{ (nm}^{-1}\text{)}$	$-8.59 \cdot 10^{-10}$

Table 3.3: Dependence of the refractive index n of air from temperature T , pressure p , humidity h and CO_2 content x_c around $T = 20^\circ\text{C}$, $p = 101.325 \text{ kPa}$, $h = 50\%$, $x_c = 400 \text{ ppm}$ and $\lambda = 1530 \text{ nm}$.

In addition, figure 3.20 shows the refractive index n as a function of the temperature T at different pressures p . Figure 3.21 shows the refractive index n as a function of the pressure p at different temperatures T . Figure 3.22 shows the refractive index

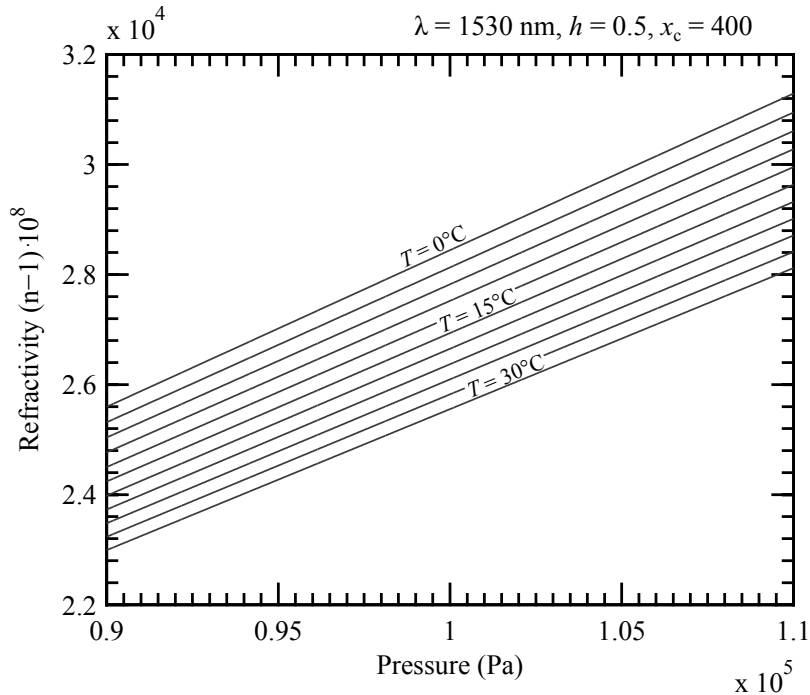


Figure 3.21: Refractivity of air as a function of the pressure p at different temperatures T . The data were calculated using the Ciddor equation evaluated for a wavelength of $\lambda = 1530$ nm, a humidity of $h = 50\%$, a CO_2 content of $x_c = 400$ ppm.

n as a function of the wavelength λ , humidity h and CO_2 content x_c .

Compensating the interferometer position readout by the precise measurement of temperature, pressure and humidity allows achieving an accuracy better than 1 ppm. This is exemplarily demonstrated for a change of the air pressure in figure 3.23. In this example, a stable cavity with a constant length of 36.7 mm was placed inside a closed chamber and exposed to a pressure change of 6.8 kPa. This pressure change was compensated by means of the weather station located inside the chamber, resulting in a position uncertainty of 0.3 ppm. The accuracy of the sensors used for this measurement was $\pm 0.1^\circ\text{C}$ (0.50°C) for the temperature, $\pm 1\text{hPa}$ (300..1100 mbar) for the pressure and $\pm 2\%$ (10..90 %) for the humidity.

In order to verify the accuracy of the interferometer at ambient conditions, the FPS3010 was calibrated at the National Metrology Institute of Germany (PTB) over a distance of 1.5 meters. The measurements were performed under various ambient

3.8. AMBIENT ENVIRONMENT COMPENSATION

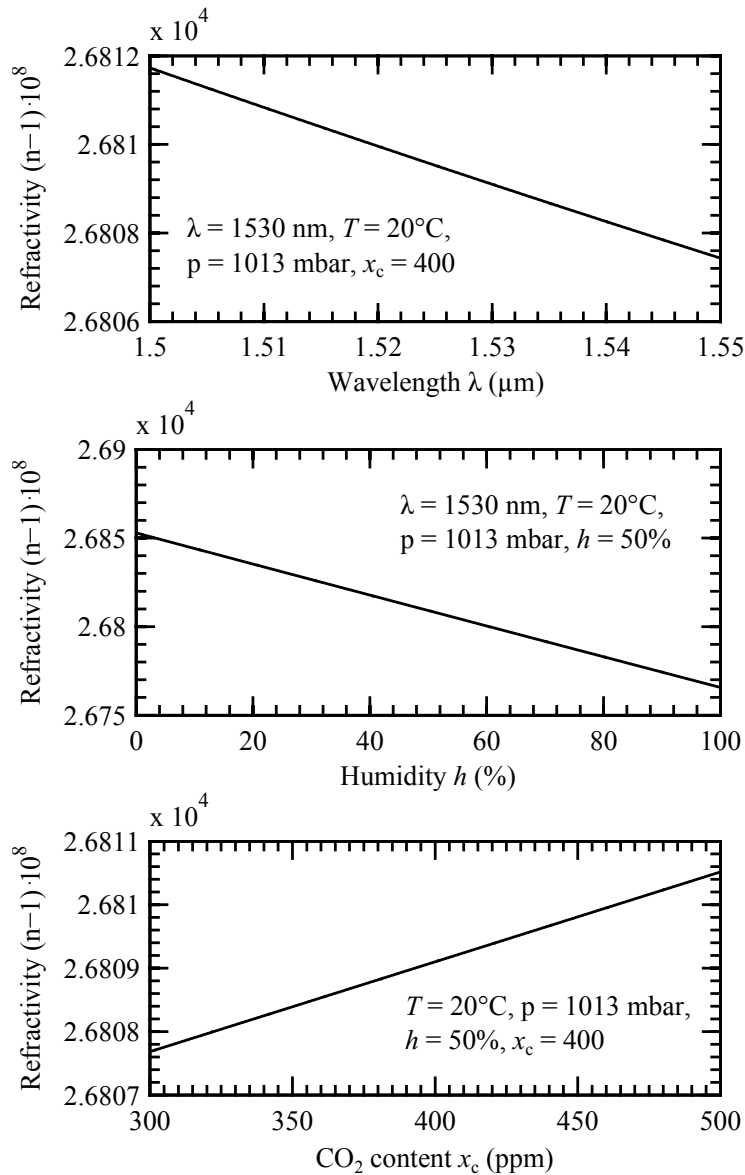


Figure 3.22: Refractivity of air as a function of the wavelength λ , humidity h , and CO₂ content x_c . The data were calculated using the Ciddor equation evaluated for a temperature of $T = 20^\circ\text{C}$ and a pressure of $p = 1013$ mbar.

conditions and the resulting refractive index changes were compensated using the environmental compensation unit. The accuracy of the FPS3010 was determined to be better than 0.14 ppm.

The main disadvantage of the weather station is that only homogeneous changes of the refractive index can be corrected, because the refractive index is measured only at one point in space. The existence of local air turbulence therefore limits the

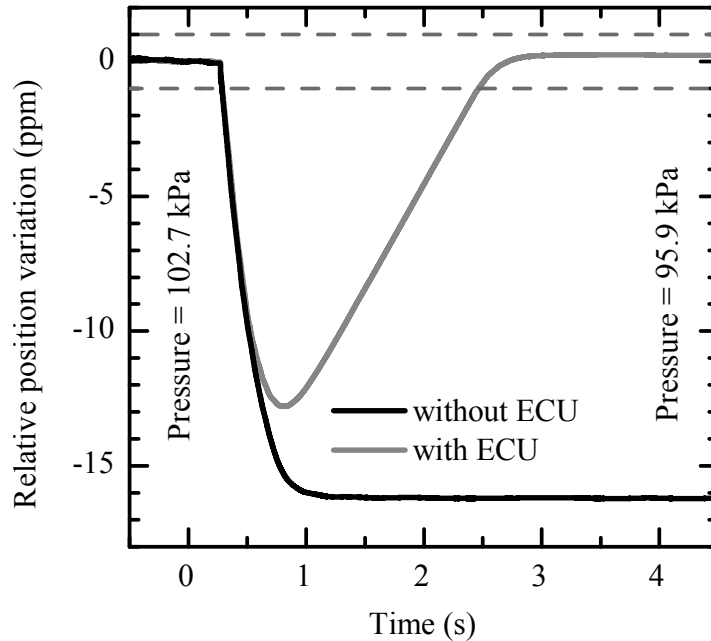


Figure 3.23: Environmental compensation of the position signal measured in a solid cavity under changing air pressure conditions. The gray line shows data corrected by a weather station, whereas the black line shows uncorrected data. The cavity is placed in a closed chamber and exposed to a pressure change of 6.8 kPa. The cavity has a length of 36.7 mm. The data show a position uncertainty of 0.3 ppm.

correction functionality. This case requires the direct measurement of the refractive index along the beam path.

3.8.2 Refractometer

The direct measurement of the absolute refractive index can be performed using interference refractometers, which continuously measure the phase change induced by the refractive index.[53] A comparison of the interference refractometers used by different research laboratories can be found in literature.[52] Measurements performed with the examined refractometers showed an agreement of better than $5 \cdot 10^{-8}$. Building an interference refractometer requires the accurate knowledge of the geometrical beam length $l = px$ of the cavity in a vacuum, the wavelength λ , and the optical phase difference $\Delta\Phi_{\text{amb}}(t)$. In order to determine $\Delta\Phi_{\text{amb}}(t)$, the cavity must be evacuated at least one time. The consideration of the uncertainty of each single parameter allows a coarse estimation of the total uncertainty that could be achieved by the presented

interferometer.

$$\frac{\delta n}{n} = \left(\frac{\delta \Delta \Phi_{\text{amb}}}{\Delta \Phi_{\text{amb}}} + \frac{\delta \lambda}{\lambda} - \frac{\delta x}{x} \right) \frac{n-1}{n} \quad (3.16)$$

The typical wavelength stability of the DFB laser is $\delta \lambda / \lambda = 4 \cdot 10^{-8}$. The phase uncertainty is mainly limited by periodic nonlinearities and is in the order of $\delta \Delta \Phi_{\text{amb}} / \Delta \Phi_{\text{amb}} = 4 \cdot 10^{-4}$ for a double pass cavity (see section 4.5) with a length of $x = 0.1$ m, but could in principle be increased to about $4 \cdot 10^{-5}$ by correcting these nonlinearities. The uncertainty of the cavity length is determined by its thermal expansion and by the uncertainty of the length measurement. The cavity is therefore ideally made of an extremely low expansion material, as e.g. the glass ceramic Zerodur [54] with a coefficient of thermal expansion of $\alpha = 0.1 \cdot 10^{-6} \text{ K}^{-1}$, leading to an uncertainty of $\delta x / x = 1 \cdot 10^{-7} \text{ K}^{-1}$. The length of the cavity could in principle be determined with an accuracy in the order of $\delta x / x = 10^{-4}$ using frequency tuning interferometry,[11] and is currently the limiting factor. In the best case, the total uncertainty would be in the order of $\delta n / n = 10^{-8}$ and, thus, about one order of magnitude better than the weather station.

At the moment, the accuracy of the measurement of the refractive index is limited by the accurate determination of the absolute length measurement of the cavity. The problem of the refractometer presented here is that the refractive index would not be measured along with the cavity under test. Finding a solution to this problem will be the central goal of future research and development.

3.9 Reference cavities

Measuring the displacement of a stationary target at ambient conditions always involves thermal drifts of the cavity length and fluctuations of the refractive index. This is especially undesired during characterization of the interferometer stability, because such distortions might be falsely attributed to the interferometer itself. The characterization of the performance of the interferometer consequently requires a stable reference cavity. Such a stable cavity can be realized by cooling it down to liquid helium temperature or by manufacture it from materials with a low coefficient of thermal expansion.

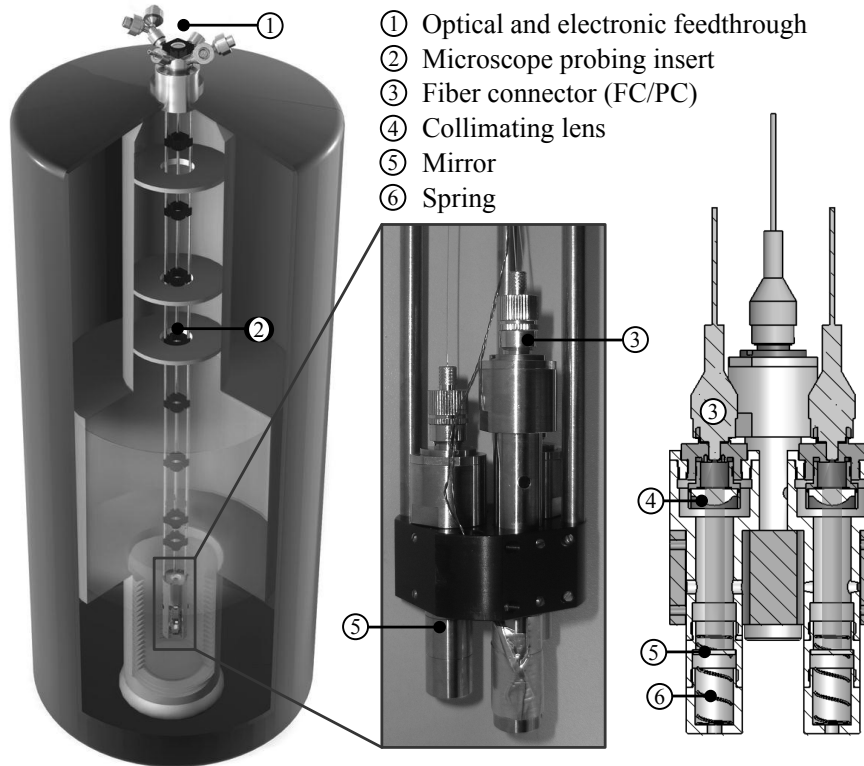


Figure 3.24: Schematic of the low temperature cryostat. The titanium cavities are cooled down to cryogenic fluid temperature by placing them into the cryogenic storage dewar. The cavities are mounted at the end of a modified attocube microscope probing insert. The insert is placed in a thin-walled stainless steel vacuum tube (not shown) filled with few millibar exchange gas in order to establish thermal contact to the dewar.

3.9.1 Low temperature cavity

Ideal drift-free cavities can only be realized by cooling them down to absolute zero temperature. In order to freeze thermal drifts in the Fabry-Pérot cavity, special low temperature cavities have been developed, which can be cooled down to cryogenic fluid temperature. Figure 3.24 shows the cryogenic setup, consisting of a top-loading liquid helium cryostat with a modified attocube microscope probing insert containing the cavity. The insert, which is shown in figure 3.25, consists of a sample stick which is placed in a thin-walled stainless steel vacuum tube. The sample stick consists of a vacuum flange and a framework which holds the cavity at the bottom of insert, where the lowest temperature is reached. The vacuum flange is equipped with several optical and electronic vacuum feedthroughs. The optical feedthrough has FC/APC connectors on both sides in order to minimize back reflections. The tube is evacuated

3.9. REFERENCE CAVITIES

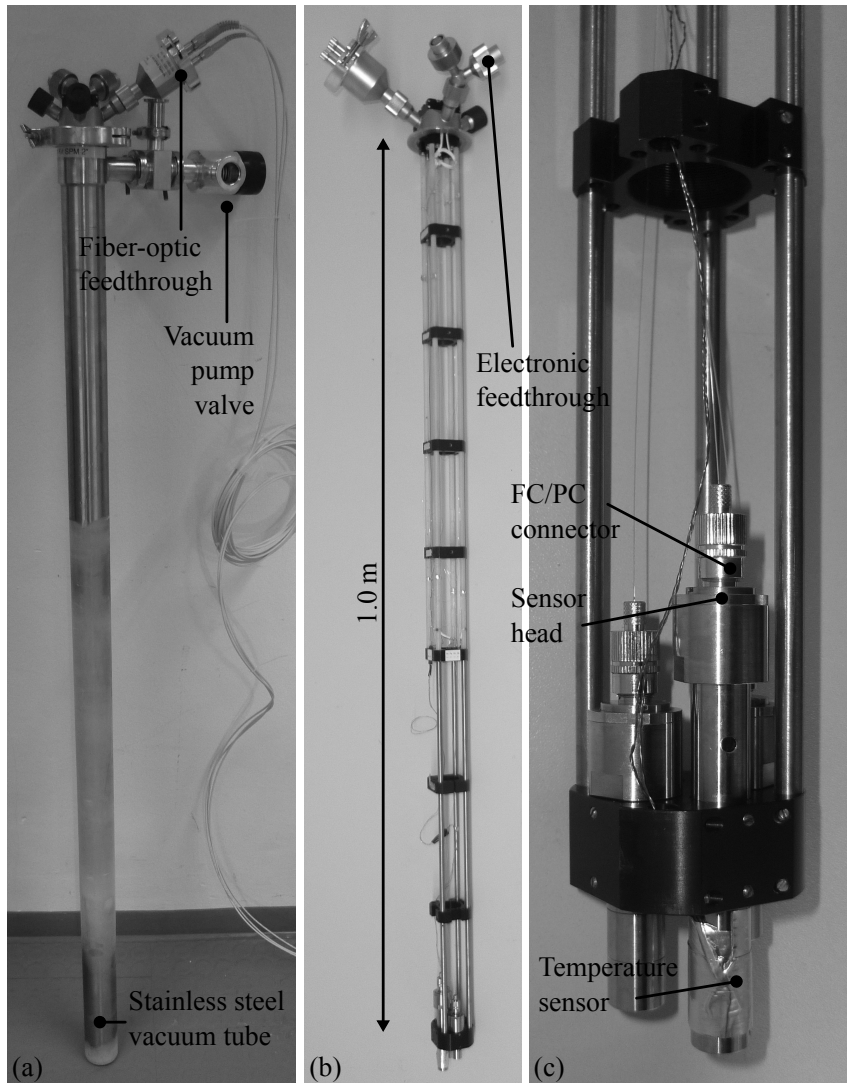


Figure 3.25: Low temperature insert. a) Cryostat insert consisting of a stainless steel vacuum tube and sample stick. b) Low temperature sample stick consisting of a vacuum flange equipped with optical and electronic vacuum feedthroughs and a framework which carries the cavities. c) Invar cavities with different lengths.

and filled with few millibar exchange gas in order to establish thermal contact to the dewar. The insert is lowered into the dewar and the cavities are cooling down. The fibers in the vacuum tube make the connection between the fiber feedthroughs (FC/APC connector) and the sensor head (FC/PC connector). Optical fibers used at low temperature and high vacuum are usually bare fibers with 250 μm diameter buffer coating and without jacket in order to avoid stresses due to thermal contraction and in order to minimize outgassing. For the same reasons, the connectors are made

without bend protection (boot).

3.9.2 Room temperature cavity

The use of low temperature cavities is time consuming and expensive. For this reason, a room temperature reference cavity that produces no running costs was developed. Figure 3.26 shows the cavity setup. The cavity is placed inside a 2 inch vacuum tube

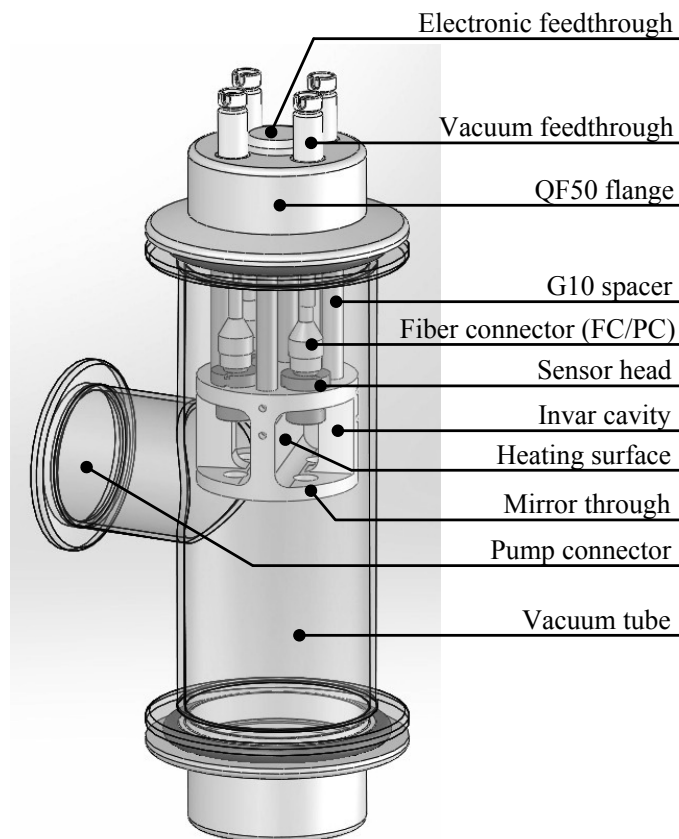


Figure 3.26: Room temperature cavity. The low expansion Invar cavity is placed in a vacuum tube in order to eliminate changes of the refractive index. The cavity can be temperature stabilized by means of a heating foil.

and is made of Invar (Fe – 36%Ni) with a low coefficient of thermal expansion of $\alpha = 3.0 \cdot 10^{-6} \text{K}^{-1}$. [55] There is a top and a bottom flange and a connector for the vacuum pump. A vacuum valve enables decoupling of the cavity from the pump. The top flange contains four optical feedthroughs for four independent interferometer axes and one electronic feedthrough. The electronic feedthrough contains 6 pins to connect

one heating foil and at least one temperature sensor (Pt100, model S651, Telemeter Electronic GmbH, 86609 Donauwörth). This enables temperature stabilization of the cavity as well as the induction of defined thermal drifts. For both processes a temperature controller (Model 335 Cryogenic Temperature Controller, Lake Shore Cryotronics, Inc., Westerville, OH 43082) was used. A solvent free 2-component epoxy resin adhesive (UHU plus endfest 300) was used to seal the gap between feedthrough and flange, whereas a sealing ring was used for the electronic feedthrough. For thermal decoupling of the cavity from the outside, the cavity was mounted to the upper flange by means of glass-fiber reinforced plastic (G-10) spacers. In order to ensure a low thermal expansion of the cavity, the mirrors were glued from the backside of the cavity. The cavity therefore has holes through which the light gets to the mirror. Gluing the mirrors to the inside of the cavity might result in thermal drifts caused by the glue.

3.10 Summary

In this chapter, the experimental realization of the interferometer described in the theoretical part was presented and the performance was specified by means of measurements. The interferometer is able to track displacements with picometer resolution and constant sensitivity and is well suited to work in extreme environments like ultra-high vacuum, cryogenic temperatures and high magnetic fields. The low output power of the interferometer, which is in the order of 0.1 mW, allows noninvasive operation, thus promoting displacement tracking even at liquid helium temperature. The use of telecom wavelength fiber-based components lowers the costs of the system and enables multi-channel operation. It was shown that the low-finesse Fabry-Pérot interferometer is capable of tracking length changes up to a working distance of 1 m with a maximum speed of 2 m/s.

The measurements in this chapter have further shown that the use of semiconductor laser diodes is well suited to replace conventional gas lasers in displacement interferometry. However, in order to achieve a wavelength stability in the order of $\delta\lambda/\lambda = 10^{-8}$, which is typically specified by the manufacturers of commercial gas laser based interferometers, this type of laser requires an active wavelength stabilization to a known wavelength reference absorption gas cell. In this way, a stability of $\Delta\lambda/\lambda = 5.8 \cdot 10^{-9}$ was successfully demonstrated.

The interferometer provides a real-time interface enabling the transfer of the displacement data with different digital protocols. The HSSL protocol transmits absolute displacement data which are encoded using a serial word format and supports high velocities and large travel ranges, but at the expense of the data rate. The A-quadrature protocol transmits incremental displacement data which are encoded using a quadrature format with four unique states and supports high frequency measurements up to the MHz range. However, the maximum velocity that can be tracked is limited by the interface bandwidth and the predefined resolution increment.

The measurements in this chapter moreover confirmed the theoretical predictions of the periodic nonlinearities stated in chapter 2.

As most of the interferometric displacement measurements are still made at ambient conditions, this chapter provides an equation for the correction of the refractive index of air using a weather station. The data show a position uncertainty of 0.3 ppm.

4 Sensor head configurations

A central part of the Fabry-Pérot interferometer system is the sensor head which is remotely connected to the interferometer system by means of a single mode fiber. The sensing cavity is then formed between the fiber end face and the target. Nowadays, the sensor head of a displacement sensor has to meet different requirements with respect to robustness, usability, size and working range. In integrated circuit manufacturing, for example, stage positioning and wafer alignment with nanometer precision over measurement ranges of up to several hundreds of millimeters is necessary to improve overlay in double patterning lithographic processes.[56, 57] Future semiconductor production will be based on extreme ultraviolet lithography which further requires the displacement sensor to be operated in a vacuum. Another example is scanning force microscopy, where an accurate spatial resolution can only be obtained when the probe position is tracked during surface scanning. The measurement range is typically in the micrometer range.[58] Since operation under extreme environments like cryogenic temperatures, ultra-high vacuum or high magnetic fields is highly desired in this field of application, it sets especially high requirements for the robustness and the size of the sensor head. The sensor head must fit into a cryostat with very constrained space and tolerate deformations caused by large temperature gradients which might lead to a misalignment of the system. In particle accelerators, for example, a large number of devices, such as steering and focusing magnets, have to be aligned with respect to the particle beam with nanometer precision,[59, 60] and this often within a vacuum and ionizing radiation.

These requirements can only be met if all electronic parts are separated from the sensor head, as is the case in the present Fabry-Pérot interferometer, where the sensor head consists only of a fiber connector, a collimator lens, and a housing holding both parts together. In contrast to the Michelson interferometer, the Fabry-Pérot interferometer includes no reference arm and no beam splitters. It profits significantly from this simple structure because it makes the sensor head small in size, robust

against external influences, and cost-efficient. The use of optical fibers makes the interferometer robust against environmental influences and allows remote sensing, thus promoting noninvasive operation.[61] These advantages are especially desirable for displacement sensors which should be operated at cryogenic temperatures or at high magnetic fields and achieve sub-nanometer resolution and accuracy, conditions where most other known commercial interferometers would fail. Depending on the configuration of the cavity, the Fabry-Pérot interferometer allows measuring on a variety of target materials which differ in their reflectivity and surface roughness. Configurations of the cavity differ in the type of lens, the separation of the lens from the fiber, and the target material. The applications presented above also require a certain tolerance of the configuration against angular misalignment. A large angular alignment tolerance tolerates, for example, deformations of the sensing cavity or guiding inaccuracies of a moving stage and makes the interferometer easy to align.

In this chapter, different configurations of the Fabry-Pérot cavity will be investigated and characterized with respect to their ability to increase the measurement range of the interferometer and to their tolerance against angular misalignment. For illustration, various representative practical configurations will be analyzed. In order to investigate the interference signal for a large parameter range, simulations have been performed which were tested to reproduce the experimental results. The simulations can help simplifying the development process and reducing the testing time for different configurations.

4.1 Instrumentation

The fiber-optic Fabry-Pérot interferometer setup is schematically shown in figure 4.1 with three different sensor head arrangements (a)-(c). The light source is a DFB laser with a wavelength of $\lambda = 1535$ nm. The laser source is connected to one of the two input arms of a two-by-two directional fiber coupler which splits the light at a ratio of 50% on each arm. One of the output arms is connected to a fiber patch cable. The polished fiber end of this cable forms the first semi-transparent mirror of the Fabry-Pérot cavity and provides the reference beam for the interferometer as it reflects about 4% of the incoming light. 96% of the light is coupled into the cavity and reflected off a mirror attached to a movable target. The reflected light is coupled back into the fiber and interferes with the reference beam, thus producing an interference

pattern which is detected at the second input arm of the coupler using a variable gain photoreceiver (Femto OE-200-IN2, FEMTO Messtechnik GmbH, Germany). In order to gain information about the maximum and minimum values of the reflected power signal at a fixed target position, the laser wavelength was swept by changing the laser temperature.

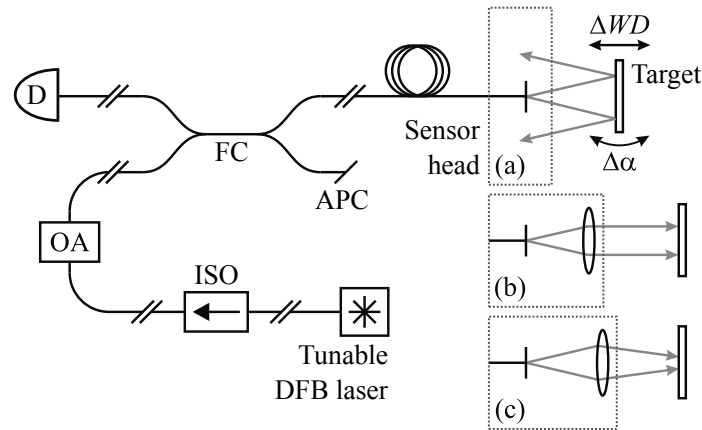


Figure 4.1: Fiber-optic measurement setup including laser source, isolator (ISO), optical attenuator (OA), fiber coupler (FC), photodetector (D) and optical Fabry-Pérot cavity, formed between fiber end and target. All parts are interconnected by FC/APC to FC/APC mating sleeves. Shown are also three different configurations of the sensing head, comprising (a) only fiber and target, (b) fiber, collimating lens and target and (c) fiber, focusing lens and target.

An example for the detected interference fringes is shown in figure 4.2. It was generated by applying a thermal drift to a cavity placed in a vacuum. The data were recorded with a bandwidth of 1 kHz. The root mean square (rms) noise at quadrature corresponds to an equivalent displacement of 0.04 nm.

The different Fabry-Pérot sensor head configurations used for displacement sensing are schematically shown in figure 4.1 (a)-(c). Configuration (a) consists of a bare fiber emitting a beam which directly impinges on the target. In (b), the light emitted by the fiber is collimated by a lens and in (c), the beam is focused by the same lens. For characterization of the measurement range and angle tolerance, both the constructive and destructive interference intensities are recorded as a function of the target tilt angle α and working distance WD . The two lens arrangements have been realized with the help of an adjustable sensor head composed of two parts. The first part includes a connector for the FC/PC fiber and the second part carries the lens. Both parts are connected to each other by a screw to retain a constant fiber

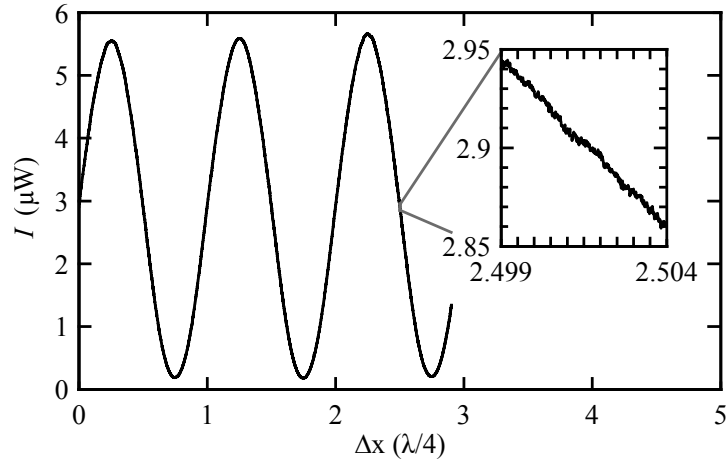


Figure 4.2: Interference pattern produced by sweeping the temperature of a 30 mm long cavity located inside a vacuum chamber. The inset shows the signal around the maximum slope.

to lens separation. In this way, different beam geometries can be easily realized. In this work, a lens with a focal length of $f \approx 8$ mm and a numerical aperture of $\text{NA} = 0.50$ was used. For testing, the sensor head was mounted onto a travel stage in order to change the cavity length, whereas the target tilts were realized by means of a gimbal center mirror mount including piezo-assisted micrometer drives. This chapter will focus on determining the interference contrast and consistently will only show measurement data of the interference extrema, corresponding to constructive and destructive interference. These intensities can also be determined analytically by inserting the coupling efficiency η into equation 2.64 and calculating $I_r(\varphi = \pi) = I_{\max}$ for constructive and $I_r(\varphi = 0) = I_{\min}$ for destructive interference. Equation 2.64 shows that the contrast crucially depends on the reflectivity of the movable target and on η . This is demonstrated in figure 2.9, which shows the constructive and destructive interference intensities and the corresponding contrast as a function of the target reflectivity R_2 , assuming $\eta = 1$. The contrast is of particular importance because it is a measure for the signal-to-noise ratio of the detected signal and thus for the resolution of the displacement sensing.[22] A maximum contrast of 1 allows displacement sensing with the highest resolution because the full detector range can be used. A contrast different to 1 leads to an offset of the interference signal and, as a consequence, not the whole detector range can be used for signal detection. The contrast is maximum around a target reflectivity that equals the fiber core, which is $R_2 = 0.0359$. For

higher reflectivities, the contrast decreases because of the increasing amount of light coupled back into the fiber. In this case, the contrast could be increased by reducing the coupling efficiency η , since $r_{2,\text{eff}}$ also depends on η according to equation 2.64. High target reflectivities thus can generally be compensated by reducing the coupling efficiency in order to achieve a higher contrast.

4.2 Coupling efficiency simulation

The amount of light coupled back into the source fiber is described by the coupling efficiency η , which is calculated as a function of the target tilt and working distance using an optics simulation software. When performing fiber coupling simulations, the numerical aperture of the optical fiber is required. Unfortunately, the definition of NA is not standardized. The manufacturers of optical fibers define it as the sine of the half light cone angle at which the far field intensity of the light exiting the fiber has fallen to 1% of its peak value ($\text{NA}_{1\%}$), while in laser optics it is commonly defined by the $1/e^2$ power level (NA_{1/e^2}). Optical software providers such as Zemax,[62] however, use two different definitions within their own software. The following considerations will refer to Zemax and provide a useful correspondence between all definitions.

In some places, the Zemax fiber coupling feature requires a source and receiver fiber NA which is defined by NA_{1/e^2} . The Corning data sheet[63] provides for the SMF-28 fiber $\text{NA}_{1\%} = 0.14$, which can be converted to the $1/e^2$ power level using the relation

$$\text{NA}_{1/e^2} = \text{NA}_{1\%} \cdot (2/\ln 100)^{1/2}. \quad (4.1)$$

It follows that $\text{NA}_{1/e^2} = 0.092$ for the SMF-28 fiber. In other places in the same software, the ‘‘object space numerical aperture’’, which refers to the source fiber NA, is twice the sine of the paraxial marginal ray angle, i.e. the full cone angle diverging from the source fiber, also called acceptance angle. It is calculated from the refractive index of core and cladding, resulting in $\text{NA} = 0.25$ according to

$$\text{NA} = (n_{\text{core}}^2 - n_{\text{clad}}^2)^{1/2}, \quad (4.2)$$

where $n_{\text{core}} = 1.4682$ is the index of refraction of the fiber core and $n_{\text{clad}} = 1.4629$ is the index of refraction of the fiber cladding at a wavelength of $\lambda = 1550$ nm, according to the Corning data sheet.

4.3 Position sensing with a bare fiber

The sensing cavity can take different shapes depending on the specific application. In a first configuration of the Fabry-Pérot cavity, the light emitted from the fiber is directly reflected by the target and coupled back into the fiber, as shown in figure 4.3 (a). This arrangement is especially well suited for applications with very constrained space. It can be found in atomic force microscopes for measuring the cantilever deflection [21] or in piezoelectric scanners for expansion measurements.

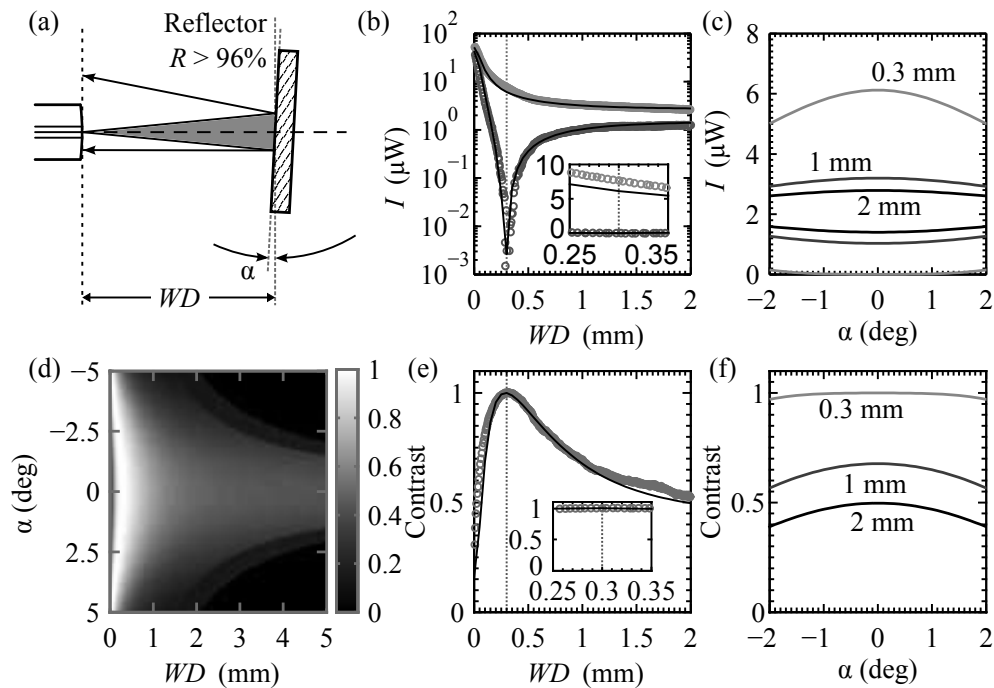


Figure 4.3: Angle and position dependence of the interference signal for the configuration shown in (a), consisting of a mirror that directly reflects the light emitted from the fiber. (b) Position dependence of the constructive and destructive interference intensities I at normal incidence ($\alpha = 0$). Light and dark gray circles denote measurement values for constructive and destructive interference, respectively. Solid lines represents simulation data. (e) Corresponding contrast. Circles represent measurement values for the contrast. (d) Simulated contrast as a function of the working distance WD and target tilt angle α . (c) Angle dependence at $WD = 0.3$ mm (position of maximum contrast), $WD = 1$ mm and $WD = 2$ mm. (f) Corresponding contrast.

An example for this interferometer type is shown in the work of Smith *et al.*, [22] where a glass wedge forms the movable reflector in order to get equal reflectivities of both cavity surfaces. Such a balanced low-finesse cavity is crucial to achieve a high

4.3. POSITION SENSING WITH A BARE FIBER

signal-to-noise ratio. Due to the divergence of the light emitted from the fiber, this system is limited to cavity lengths not exceeding $5 \mu\text{m}$, a range which is too small for most applications. Extending the measurement range of this type of interferometer and at the same time preserving its large angular alignment tolerance will be the central goal of this work.

In the special case of the bare fiber, a good signal contrast can be achieved by either using a glass target placed in close vicinity to the fiber or by using a high reflective target placed far enough away so that the beam divergence reduces the back coupled power to approximately 4% of the total power. In order to determine the position of maximum contrast for high reflective targets analytically, the position dependent power coupling efficiency of the reflected light must be known. For normal incidence, it can be calculated by the convolution of two Gaussian beam profiles, one representing the field distribution of the acceptance fiber Ψ_1 and the other one representing the field distribution Ψ_2 after a distance of two times the cavity length z .

$$\eta = \left| \int d^2r \Psi_1 \Psi_2^* \right|^2 \quad (4.3)$$

The radial field distribution Ψ at a distance ζ from the source fiber is given by

$$\Psi(\zeta) = \sqrt{\frac{2}{\pi}} \frac{1}{w(\zeta)} \exp \left\{ - \left(\frac{r}{w(\zeta)} \right)^2 \right\} \quad (4.4)$$

where w is the beam waist size and r is the radius with respect to the fiber optical axis. The normalized power coupling efficiency η is then given by the convolution of the field distributions at a distance $\zeta_1 = 0$ and $\zeta_2 = 2z$.

$$\begin{aligned} \eta &= \left\{ \frac{2}{\pi w_1 w_2} \int_0^{2\pi} d\varphi \int_0^\infty dr \exp \left[- \left(\frac{1}{w_1^2} + \frac{1}{w_2^2} \right) r^2 \right] \right\}^2 \\ &= \left[\frac{2w_1 w_2}{w_1^2 + w_2^2} \right]^2 \end{aligned} \quad (4.5)$$

The beam waist at a distance ζ from the fiber is

$$w(\zeta) = w_1 \sqrt{1 + (\zeta/z_R)^2}, \quad (4.6)$$

where z_R is the Rayleigh length, given by

$$z_R = \frac{\pi w_1^2}{\lambda}. \quad (4.7)$$

Inserting equation 4.6 into equation 4.5 yields the coupling efficiency as a function of the target distance z for normal incidence,

$$\eta(z) = \left\{ \frac{2\sqrt{1 + (2z/z_R)^2}}{2 + (2z/z_R)^2} \right\}^2 \quad (4.8)$$

It can be used to calculate the interference intensities and the contrast using equation 2.64. The resulting contrast is represented by the solid line in figure 4.3 (e) and is identical to the results from the simulations.

Apart from this analytical approach, simulations have been carried out to quantify the signal change for target tilts with respect to the fiber optical axis and for target movements along this axis. The results are shown in figure 4.3 (b)-(f) and compared to position dependent measurements at normal incidence. For small distances between the fiber and target, the signal intensities decrease rapidly with increasing working distance, whereas the contrast becomes maximum when the returning light intensity approaches 4%. For normal incidence, the maximum contrast is reached at a distance of 0.3 mm away from the fiber (cf. figure 4.3 e). The inset of figure 4.3 (b) shows the signals in a range of 50 μm around the maximum contrast. This area is well suited for piezo scanner position readout as the signal contrast is well above 0.98 in this range. Regarding the position readout, it is important to note that this configuration is not compatible with the quadrature detection scheme presented earlier in this work. The reason for this lies in the small modulation depth which can be achieved at these short distances. The modulated amplitude is typically too small for being resolved by the demodulator.

4.4 Towards increasing the measurement range

One way to increase the measurement range of a low-finesse Fabry-Pérot interferometer is to put a collimating lens into the beam path between the fiber and glass target, as shown in figure 4.4 (a). When the light hits the reflector at normal incidence and the reflector is made of glass with a reflectivity similar to the fiber core, the signal contrast becomes maximum as demonstrated in figure 4.4 (b) and (c). The figures show both constructive and destructive interference intensities and the corresponding contrast as a function of the target tilt angle α . Both interference intensities are approaching $I_{r1} = 2.1 \mu\text{W}$ for large angles, meaning that the coupling of light from the

4.4. TOWARDS INCREASING THE MEASUREMENT RANGE

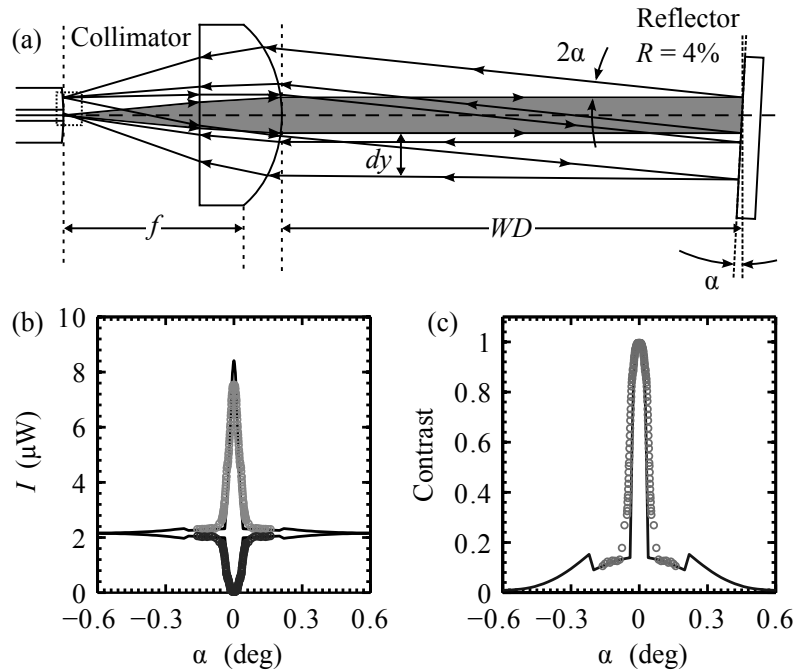


Figure 4.4: Angle dependence of the interference signal for the configuration shown in (a), consisting of a lens which collimates the light emitted from a fiber and a plane glass target that reflects part of the light at a working distance of 31 mm. (b) Interference intensities I as a function of the target tilt angle α . Light and dark gray circles denote measurement values for constructive and destructive interference, respectively. Solid lines represent simulation data. (c) Corresponding signal contrast. Circles denote measurement values for the contrast. The solid lines represents simulation data.

cavity into the fiber nears zero, so that only the reflection from the fiber end I_{r1} contributes to the detected intensity. The total intensity I_0 which is routed to the cavity is then $I_0 = I_{r1}/R_1 = 52.5 \mu\text{W}$, where $R_1 = 0.0359$ is the reflectivity of the fiber core. The data reveal the main problem of this approach, namely a very high sensitivity of the interference signal contrast to target angular misalignment. This makes this arrangement unsuitable for many displacement tracking applications. However, this configuration provides the highest accuracy because it produces no geometrical errors and allows two dimensional displacement tracking on plane surfaces. It is therefore used for position tracking of high-precision stages moving in two or three directions in space.

A further arrangement might use a retro reflector instead of a plane reflector to increase the angle tolerance of the displacement measurement. To determine the angle tolerance, an aluminum coated corner cube retro reflector was mounted on a tilt

stage at a working distance of $WD = 400$ mm, as depicted in figure 4.5 (a). When

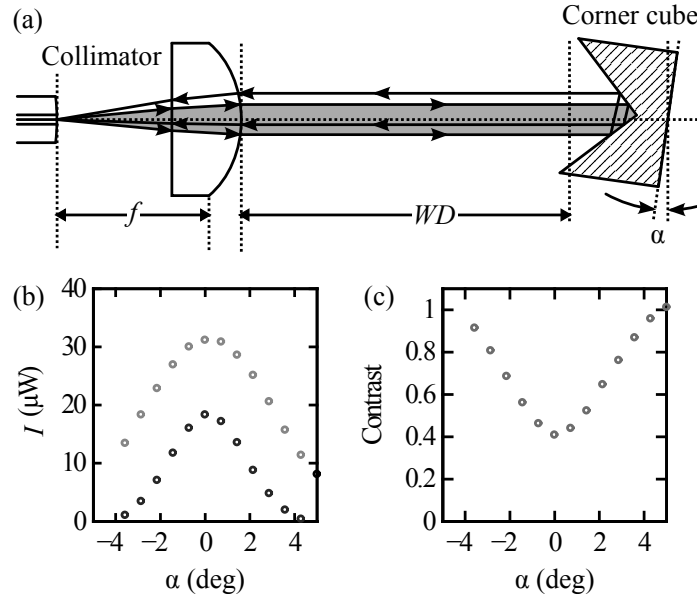


Figure 4.5: Measured angle dependence for the configuration shown in (a), consisting of a lens which collimates the light emitted from a fiber and an aluminum coated corner cube retro reflector placed at a working distance of 400 mm. (b) Interference intensities I . Light and dark gray circles denote measurement values for constructive and destructive interference, respectively. (c) Corresponding signal contrast. Gray circles denote measurement values for the contrast.

increasing the target angle, i.e. the angle between the retro reflector optical axis and the incident beam optical axis, the interference signals decrease as shown in figure 4.5 (b), whereas the contrast increases according to figure 4.5 (c). The angle dependent decrease of the interference intensities result from a reduction of the light that is coupled back into the source fiber, caused by an offset between the fiber optical axis and the reflected beam. At 0° , the light emitted into the cavity is expected to be completely coupled back into the fiber, thus causing the interference intensities to be around I_0 . As this is not the case, there must be imperfections in the corner cube which prevent the light from being reflected parallel to the incident beam, thus causing losses which reduce the power at the detector. For practical applications, the contrast can be further improved by tilting or decentering the corner cube.

4.5 Position sensing using a confocal double pass arrangement

The previous section shows that a tedious alignment of the reflector is required to couple the light back into the fiber when using a low reflective plane target, thus making this technique hard to use and sensitive to angular changes which might occur during a target movement. A corner cube retro reflector might relax the alignment procedure, but for some applications it is too bulky, too expensive, or it might suffer from a weak signal contrast when working in the center of the corner cube. In some other applications, such as tracking the position of a stage moving in two directions, using a retro reflector is not possible, since they only support movements in one direction.

A new approach uses a high reflective plane target slightly tilted with respect to

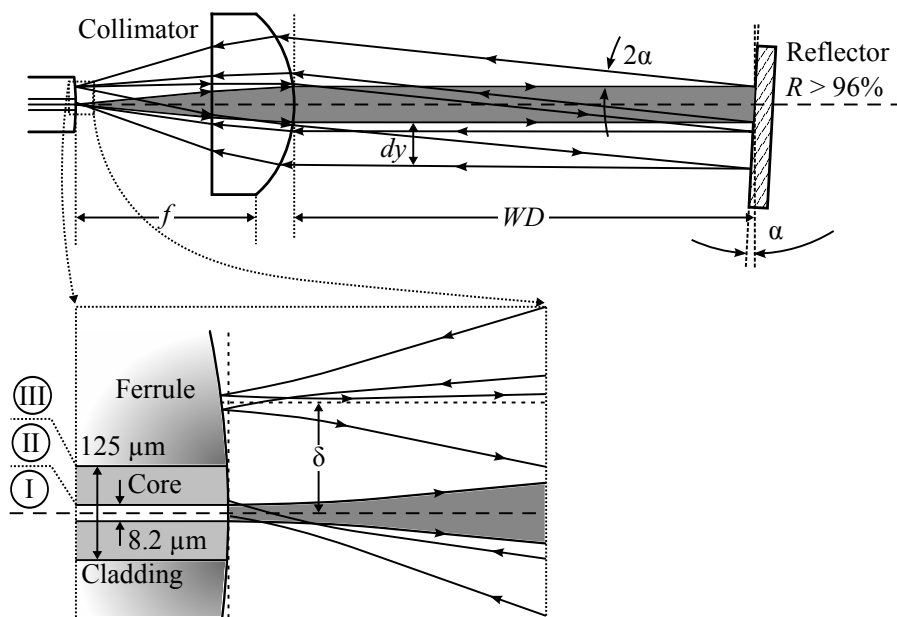


Figure 4.6: Confocal double pass arrangement consisting of a lens that collimates the light emitted from the fiber and a high reflective plane mirror placed at a working distance WD away from the lens. When tilting the target away from normal incidence, the reflected spot moves along the fiber end face and increases in this way the angular acceptance angle. An increase of the tilt angle α also increases the lateral offset dy between the incident and reflected beam, leading to a reduction of the coupling efficiency.

the incident collimated beam, forming a confocal arrangement as shown in figure 4.6.

In this configuration, the beam is not directly coupled back into the fiber. It rather makes use of a small target misalignment causing the reflected light to be focused on the fiber cladding or the ferrule of the connector surface.[4] Depending on the reflectivity of cladding or ferrule, a certain amount of light is reflected off the connector surface and passes the cavity a second time. Since the returning beam is parallel to the incident collimated beam, it will be exactly focused to the fiber core after having passed the cavity twice. This means that the cavity has a kind of self-alignment mechanism that makes the coupling of the reflected light into the fiber independent from the target alignment. At the same time, the balanced reflectivities of the fiber core and cladding allow to achieve a high signal contrast of the interference pattern. Additionally, their low reflectivities, which are in the order of 4%, make the cavity low-finesse, resulting in a more sinusoidal interference pattern which again increases the accuracy of displacement measurements.

To demonstrate the signal tolerance against target tilts and displacements for a wide parameter range, simulations have been carried out, for which the arrangement is investigated in greater detail. The optical system in figure 4.6 can be described as a folded Fabry-Pérot cavity which is set up between the fiber core and cladding respectively ferrule, separated by a cavity length which equals about twice the distance between fiber end and target. The reflector only serves as a folding element which has no influence on the finesse of the cavity. The crucial point of this technique is the beam focusing to the fiber connector surface. For this reason, this section will focus on the beam geometry near the fiber, which is shown in more detail in the inset of figure 4.6. For the given configuration, the angle between incident beam and its first reflection is twice the tilt angle α of the reflector. It follows that the distance δ between the center of the fiber core and the reflected spot is

$$\delta = f \tan(2\alpha), \quad (4.9)$$

where f is the effective focal length of the collimator lens. The reflected spot consequently moves along the radial direction on the connector surface when the reflector surface normal is tilted away from the fiber optical axis, thus relaxing the alignment procedure. The end face of an optical single mode FC/PC connector is composed of three parts, namely the fiber core, the cladding and the ferrule. The fiber core has a diameter of $8.2 \mu\text{m}$ and an index of refraction of $n_{\text{core}} = 1.4682$ at a wavelength of $\lambda = 1550 \text{ nm}$, [63] leading to a reflectivity of $R_{\text{core}} = 0.0359$ in standard air with an

4.5. POSITION SENSING USING A CONFOCAL DOUBLE PASS ARRANGEMENT

index of refraction of $n_{\text{amb}} = 1.0003$, according to

$$R_{\text{core}} = \left| \frac{n_{\text{core}} - n_{\text{amb}}}{n_{\text{core}} + n_{\text{amb}}} \right|^2. \quad (4.10)$$

The cladding has a diameter of $125 \mu\text{m}$ and an index of refraction of $n_{\text{clad}} = 1.4629$ at the same wavelength, yielding a reflectivity of $R_{\text{clad}} = 0.0353$. The ferrule is made of zirconia and has an index of refraction of $n_{\text{ferrule}} = 2.1252$ at $\lambda = 1550 \text{ nm}$, yielding a reflectivity of $R_{\text{ferrule}} = 0.1295$ in air. Usually, the end face of a FC/PC connector is not flat. It has a radius of curvature of about $r_{\text{ferrule}} = 20 \text{ mm}$, which also has to be considered in the simulations. To simulate the whole complexity of the folded cavity with respect to interference intensities, the simulations were subdivided into three cases, characterized by the radial position δ of the reflected spot on the fiber surface or by the tilt angle α , which is related to δ by equation 4.9.

For small angles, referring to $|\delta| < 4.1 \mu\text{m}$ or $|\alpha| < 0.014^\circ$ (regime I), the Fabry-Pérot cavity is set up between the fiber end and mirror and the beam passes the cavity only once (single pass, folding order $p = 1$) because the spot lies on the fiber core. This means that the reflectivities of the target and the core have to be considered in the transfer function calculations of the cavity.

When the tilt is further increased, corresponding to $4.1 \mu\text{m} < |\delta| < 62.5 \mu\text{m}$ or

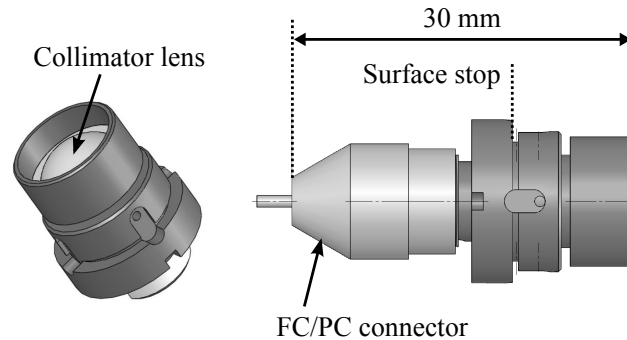


Figure 4.7: Technical drawing of the low expansion double pass sensor head. The thermal stability of the sensor heads was improved by relocating the surface stop level to the level of the connector ferrule end. This eliminates the effective collimator length which is subject to thermal drifts.

$0.014^\circ < |\alpha| < 0.220^\circ$ (regime II), the configuration enters the regime in which the beam passes the cavity twice (double pass). In this regime, the beam is focused on and reflected off the fiber cladding and the mirror only has a folding function. This means that the Fabry-Pérot cavity is set up between the fiber core and cladding,

leading to a cavity length that is about twice the distance between fiber and target and the folding order is $p = 2$.

For tilts exceeding 0.220° or $|\delta| > 62.5 \mu\text{m}$ (regime III), the configuration is still in double pass mode, but the beam is focused on the ferrule, leading to a higher finesse of the cavity because of the higher reflectivity of the ferrule. The transition between the cladding and ferrule causes a jump in the reflected interference signal because of the higher reflectivity of the ferrule.

The practical realization of such a sensor head is shown in figure 4.7. The sensor heads are made of titanium and are therefore resistant to corrosion and well suited to work in magnetic fields. It further provides a connector for a FC/PC fiber. The lens is inside a separate part which is glued to the fiber part in order to ensure a good beam collimation. Such collimating sensor heads can also be bought from different companies, but usually do not provide a sufficient beam collimation.

4.5.1 Measurements and simulations

The simulation results for the angular dependence of the interference intensities at a working distance $WD = 31 \text{ mm}$ are shown in figure 4.8 and compared to measurements. Figure 4.8 (a) shows a detail of the fiber end face drawn to scale according to the plots below. Figure 4.8 (b) shows measurements and simulations of the angle dependent contrast. In the high contrast regime III, the back coupled signal power decreases with increasing target tilt, which shows up in a decrease of the contrast in (c) for angles larger than 0.6° . This decline is caused by the limited acceptance angle of the fiber which reduces the amount of light which is coupled back into the fiber, i.e. the larger the angle of incidence towards the fiber is, the lower is the coupling efficiency. An increasing tilt increases the distance between the incident and the last reflected beam (denoted as dy in figure 4.8 a), thus increasing the fiber incidence angle of the latter. The single pass regime I, however, has a weak contrast because of the large amount of light which is coupled back into the fiber and is, therefore, not suited for high resolution displacement sensing, i.e. in this arrangement the target should always be slightly tilted. The simulations in this section make a good fit to the experimental data and are therefore well suited to predict the physical properties of the sensor head. Deviations might arise from deviations of the ferrule curvature or from a badly collimated beam.

Figure 4.9 (a) shows both constructive and destructive interference intensities for

4.5. POSITION SENSING USING A CONFOCAL DOUBLE PASS ARRANGEMENT

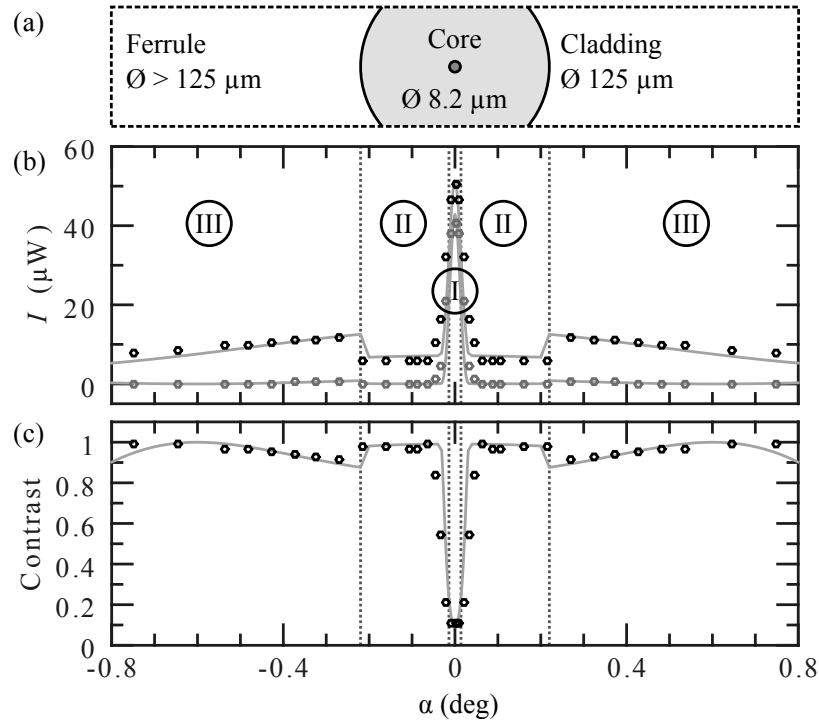


Figure 4.8: Angle dependence for the double pass configuration. (a) Detail of the fiber end face drawn to scale. (b) Interference signal as a function of the target tilt angle α at a working distance $WD = 31$ mm. Black and gray circles denote measurement values for constructive and destructive interference, respectively. Solid lines denote corresponding simulation data. (c) Corresponding contrast. Circles represent measurement values for the contrast. Solid lines denote results from the model calculation. Angular range I refers to single pass mode, whereas range II and III refers to double pass mode.

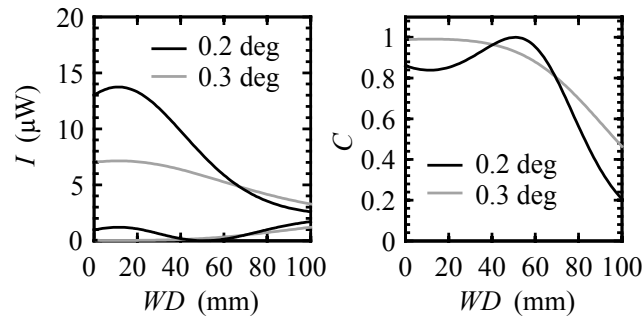


Figure 4.9: Calculated constructive and destructive interference intensity I (a) and contrast C (b) as a function of the working distance WD for the double pass configuration.

working distances ranging from 0 to 100 mm at two exemplary angles that correspond to a reflection on the cladding ($\alpha = 0.2^\circ$, regime II) and the ferrule ($\alpha = 0.3^\circ$, regime III). Figure 4.8 (b) shows the corresponding contrast. The lower contrast for

small distances at $\alpha = 0.3^\circ$ results from the higher reflectivity of the ferrule. When the distance to the target is further increased, the contrast becomes maximum as a result of a decreasing coupling efficiency which compensates the high reflectivity of the target.

Figure 4.10 shows simulations of the distance and angle dependent contrast. The dark regions have a weak interference contrast and are not suited for operation of the interferometer. This applies in particular to the horizontal dark line which represents the single pass regime I. Here, the strong signal will lead to a saturation of the photodetector.

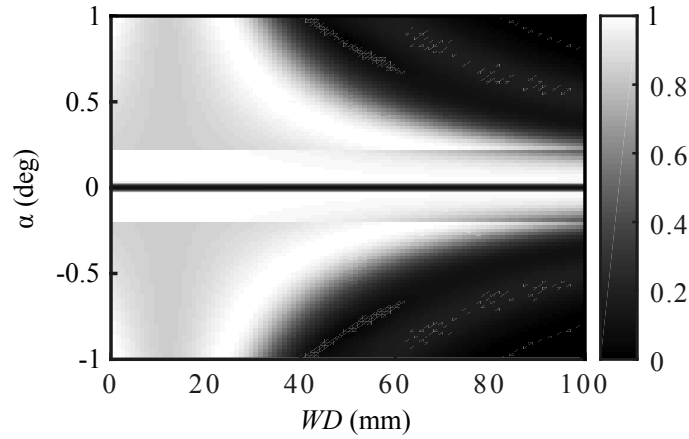


Figure 4.10: Simulated contrast as a function of working distance WD and target tilt angle α for the double pass configuration.

4.5.2 Nonlinearities

The advantage of the confocal double pass arrangement is the high alignment tolerance. This is, however, associated with nonlinearities which degrade the accuracy of the position signal. In particular, two nonlinearity sources can be distinguished. The first one results from the beam geometry inside the cavity, the second one results from a mixing of the single and double pass state, referred to as double modulation in this work.

4.5.2.1 Geometrical nonlinearities

Besides cosine and Abbé errors,[35] the accuracy of the displacement measurement in the confocal double pass system is mainly limited by the geometrical error caused

4.5. POSITION SENSING USING A CONFOCAL DOUBLE PASS ARRANGEMENT

by angular misalignment of the target. Angular tilts lead to an elongation of the beam path with respect to normal incidence. This issue is illustrated in figure 4.11 (a), where the thick black line shows the central beam path within the folded Fabry-Pérot cavity. In order to quantify the deviation of the beam length with respect to normal incidence, the length of the central beam was calculated using Zemax and subtracted from the beam length at zero target tilt. The beam elongation is shown in figure 4.11 (b) as a function of the working distance for different target tilt angles α . The data reveal that the beam length does not increase linearly with the working

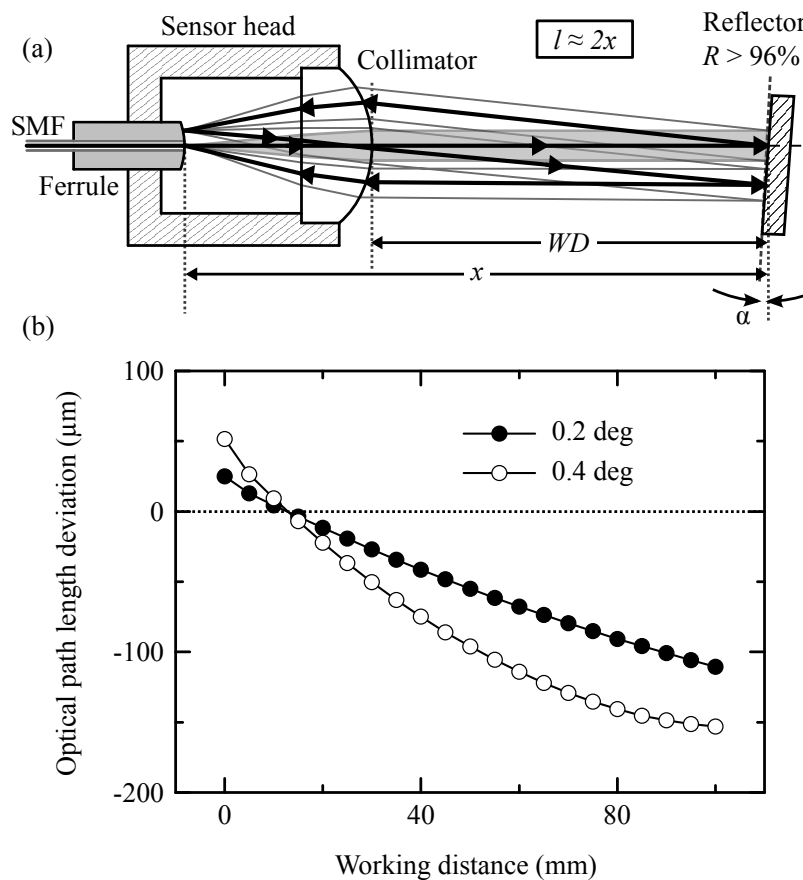


Figure 4.11: (a) Drawing of the alignment free interferometric sensor head. The fiber core and cladding form a folded Fabry-Pérot cavity with a length $x \approx 2l$. (b) Deviation of the optical path length from normal incidence as a function of the working distance and for different target tilt angles α .

distance, thus limiting the measurement accuracy to several tens of micrometers for displacements over the full range of 100 mm. For example, when displacing the target at a tilt of $\alpha = 0.2^\circ$ over the full range of 100 mm, the total error is 110 μm . The

beam elongation also increases with increasing target tilt angle. In order to obtain nanometer accuracy for sub-meter displacements, it is recommended to use a corner cube retro reflector or a plane glass target.

4.5.2.2 Double modulation

When the target mirror is moving with constant velocity under an angle somewhere in between regime I and II, the interference pattern will beat with half of the frequency of the the double pass mode. The reason for this is that, for small target tilt angles, the folding order of the cavity is a mixture between non folded ($p = 1$, single pass) and folded ($p = 2$, double pass) state, resulting 4π -periodic phase nonlinearities.

4.6 Position sensing with focusing optics

Practice has shown that it's not always possible to attach a sufficiently large reflector to the displacing target. Applications further might require the measurement directly on rough surfaces, surfaces with low reflectivity or surfaces with curvatures. Other applications allow only a very small beam spot on a surface with arbitrary reflectivity. For all these applications, it is appropriate to use a focused beam which is easily realized by moving the lens a bit further away from the fiber, as schematically shown in figure 4.12 (a). Light being reflected off a target placed in the focus of the beam will always be refocused to the fiber core. This makes the configuration very tolerant against misalignment of the target and, thus, also applicable to rough surfaces. This configuration is especially well suited for targets with a low reflectivity, as the maximum contrast is achieved for a reflectivity of about 4%, assuming that $\eta = 1$. The small spot size at the focus point again promotes the use of rough surfaces and small targets. The $1/e^2$ intensity beam diameter at the focus point is twice the radial beam waist w , given by $w \approx \lambda/\pi\theta$, where θ is the half convergence angle of the beam propagating towards the target. High reflective targets, however, significantly decrease the fringe contrast when placed in the focus. Therefore, the coupling efficiency needs to be reduced, which can be achieved by defocusing of the target. Since the technique used for measuring displacements with a focused beam consequently depends on the target reflectivity, this section distinguishes exemplarily between low reflective ($R \approx 4\%$) and high reflective targets ($R > 96\%$) to illustrate the difference of both approaches. For both parts, the resulting signal and its sensitivity to target

4.6. POSITION SENSING WITH FOCUSING OPTICS

misalignment and position changes is exemplary shown for one special arrangement of fiber, lens and target. Here, the focusing lens is inserted into the beam path at a distance $d_{fl} = 7.38$ mm away from the fiber. This leads to a focus point at a working distance of $WD = 54$ mm with a beam width of $28 \mu\text{m}$. Basically, the focus point F can be adjusted to different working distances by simply changing the distance between the fiber and lens in the sensor head. The position of the focus point as a function of the fiber to lens distance d_{fl} is shown in figure 4.12. It is noteworthy

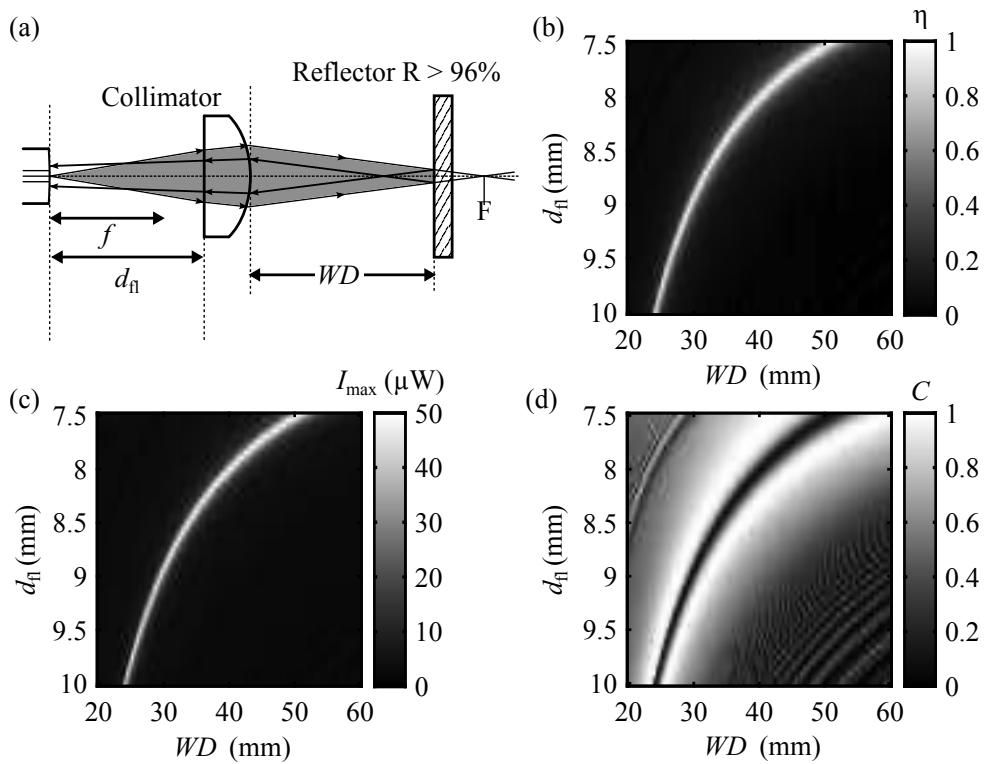


Figure 4.12: Simulation of the working distance WD of the focus point F as a function of the fiber to lens distance d_{fl} for the focused beam arrangement shown in (a). (b) Coupling efficiency η , (c) constructive interference intensity I_{max} , and (d) interference contrast C as a function of WD and d_{fl} .

that the ultimate accuracy of this method requires taking the Gouy phase shift into account, especially when the target shifts through the focus.[64]

4.6.1 Target with low reflectivity

Displacement measurements of targets with low reflectivity are required in applications such as the positioning of telescope lenses with low reflectivity or the quantiza-

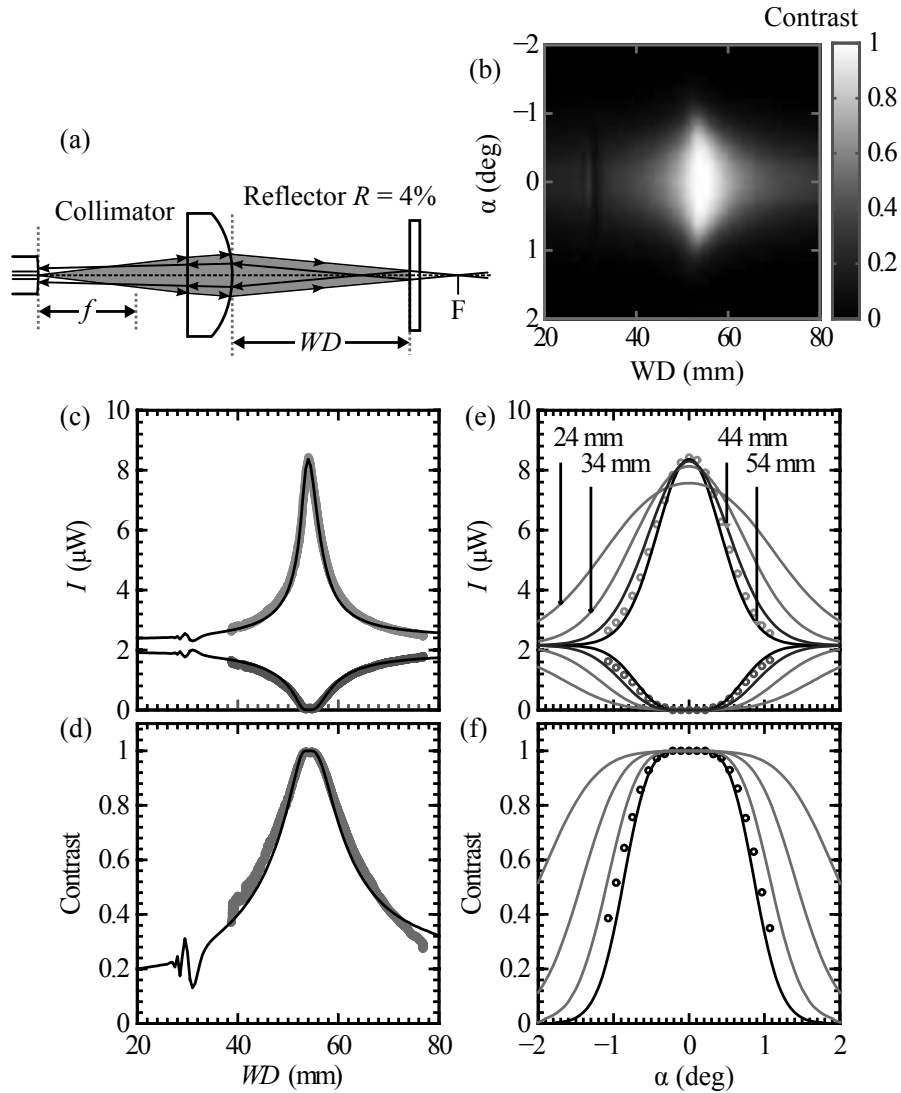


Figure 4.13: Angle and position dependence for the configuration shown in (a), consisting of a low reflective plane glass target and a lens which focuses the light from the fiber to a working distance of $WD = 54$ mm. (b) Simulated contrast as a function of working distance WD and target tilt angle α . (c) Position dependence of the constructive (upper curve) and destructive (lower curve) interference intensities I at normal incidence. Circles denote measurement values and lines represents simulation data. (d) Corresponding contrast. (e), (f) Angle dependence at the focus point with the beam focused to $WD = 24$ mm, $WD = 34$ mm, $WD = 44$ mm and $WD = 54$ mm.

tion of the expansion of a piezoelectric material with high surface roughness. In this case, the targets must be placed directly in the focus point of the lens in order to maximize the back coupled light intensity to ideally 4% of the incident light and to ensure a large fringe contrast.

To demonstrate the signal tolerance against target tilts and displacements, measurements have been carried out using a plane glass with a curved backside placed in the focus of the beam so that the plane surface forms the second semi-transparent mirror of the cavity. The curvature helps to reduce unwanted reflections from the backside. The target is made from crown glass (BK7) with an index of refraction of $n_2 = 1.50065$, yielding a reflectivity of $R_2 = 0.040$ in dry air. The measurements are again compared to simulations covering a greater parameter range.

The analysis of the data shown in figure 4.13 reveals a good agreement between measurement and simulation. The reflectivity of the target, which is very similar to the fiber core, leads to a very high contrast of $V = 0.996$ in the experiment and $V = 1.000$ in the simulation. The contrast drops to $V = 0.9$ for distances of about $\Delta WD = \pm 3$ mm around the focus point. In the same interval, the constructive signal drops by a factor of about 2, thus limiting the accuracy of large range measurements, as intensity changes are always interpreted as displacements. To ensure a measurement accuracy in the low nanometer regime, displacements should be limited to a few hundred nanometers around the focus point. Figure 4.13 (e) and (f) show the angle dependence of the interference intensities I and the contrast at the focus point, respectively, and this for different working distances of the focus point. For the focus point at $WD = 54$ mm, the contrast drops to $V = 0.5$ for tilt angles of $\alpha = \pm 0.9^\circ$ around the fiber optical axis, demonstrating the high tolerance of this method against target misalignment. The angle dependence can be further reduced by focusing the beam to smaller working distances, i.e. the system gets more tolerant to misalignment the smaller the distance to the focus is. The decrease of constructive interference intensity with decreasing focus distance at normal incidence originates from optical aberrations.

4.6.2 Target with high reflectivity

Other applications require the measurement of displacements of high reflective surfaces and, at the same time, only allow very small beam spots or curved surfaces. Examples are the measurement of cantilever movements [65] or the measurement of the wobble of a rotating cylinder.[66] Some applications, moreover, suffer from a limited space, as for example when working in cryostats that allow only very small sensor heads, but require a measurement range of several millimeters. A focusing sensor head with a small lens operated in a defocused mode can meet these demands.

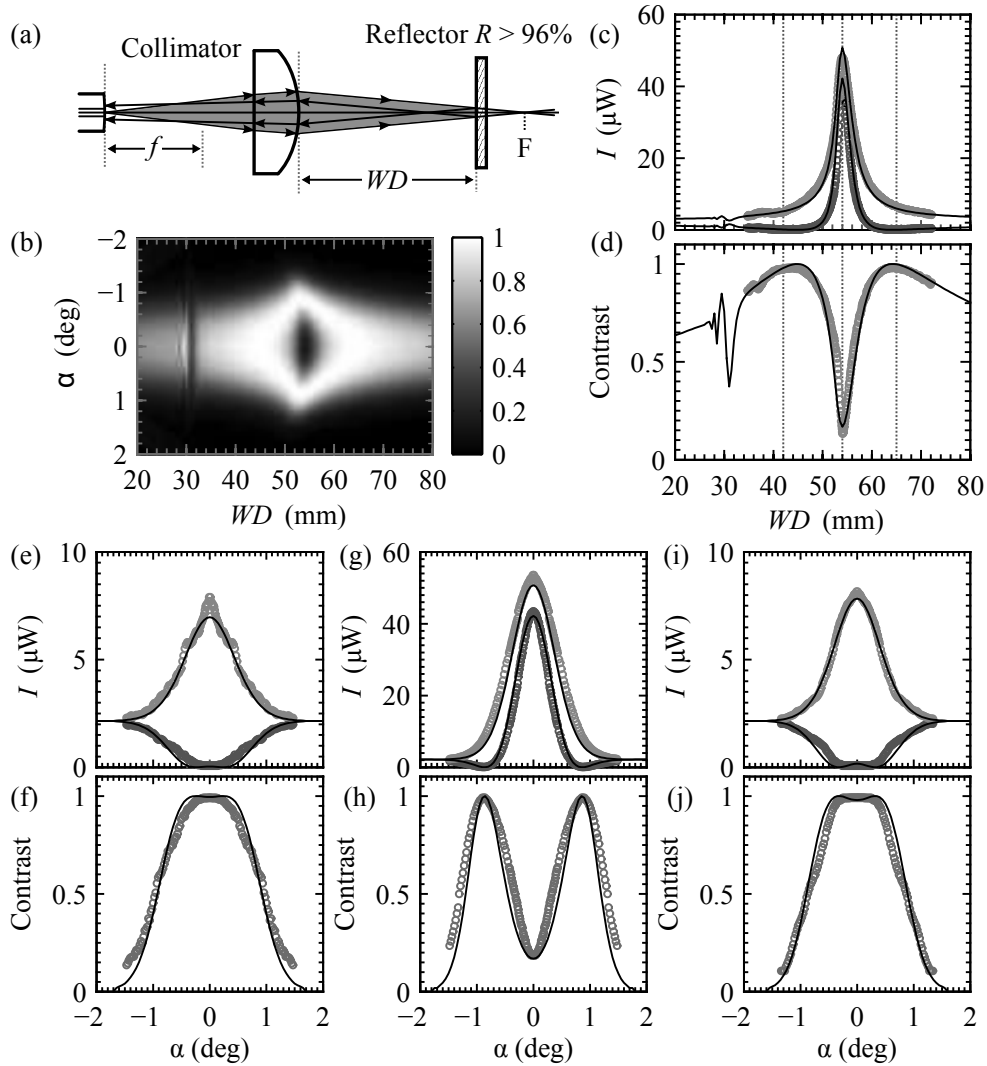


Figure 4.14: Angle and position dependence for the configuration shown in (a), consisting of a high reflective plane mirror and a lens which focuses the light from the fiber to a working distance of $WD = 54$ mm. (b) Simulated contrast as a function of working distance WD and target tilt angle α . (c) Position dependence of the constructive (upper curve) and destructive (lower curve) interference intensities I at normal incidence. Circles denote measurement values and lines represents simulation data. (d) Corresponding contrast. Circles represent measurement values and lines represents simulation data. (e)-(j) Angle dependence at $WD = 42$ mm, $WD = 54$ mm (focus point) and $WD = 65$ mm. Circles denote measured data and lines denote results from the model calculation.

The slightly larger target spot size outside the focus enlarges also the reflected spot size, leading to a smaller coupling efficiency and, consequently, to a higher contrast. A large angle tolerance is still guaranteed because of the large area which is covered

by the reflected beam on the fiber surface.

Figure 4.14 shows both theoretical and experimental data for the system consisting of a focused beam and a high reflective mirror. According to the simulations in figure 4.14 (b), the contrast has a minimum at the focus point due to the high coupling efficiency and the high target reflectivity, leading to a saturation of the detector at that point or, if the signal is attenuated, to a low displacement resolution. According to figure 4.14 (c) and (d), interferometry should be rather performed at working distances of about ± 5 mm around the maximum contrast at $WD = 42$ mm and $WD = 65$ mm, yielding a contrast greater than $V = 0.9$. This working range is about twice the range measured with low reflective targets and the change of signal intensities is significantly reduced, thus promoting long range measurements with high accuracy. The points of maximum contrast are also very insensitive against misalignment, as shown in figure 4.14 (e), (f) and (i), (j). According to these figures, a contrast of $V = 0.5$ is reached at a target tilt of $\Delta\alpha = \pm 0.8^\circ$. For large range measurements over several hundreds of nanometers, the intensity change has to be taken into account when accuracies of only a few nanometers are required. Figure 4.14 (g) and (h) additionally show the angle dependence at the focus point, illustrating again the good accordance between measurements and simulations. The simulation results in figure 4.14 (b)-(d) further show oscillations in the intensities and the contrast around $WD = 30$ mm, which might be attributed to wavefront distortions.

4.6.3 Target with curved surface

Up to now, measurement with the focusing optics only considered plane surfaces. This section will show theoretically, by means of one practical example, that measurements on curved surfaces are possible as well. In this particular case, the wobble of a high reflective rotating cylinder with a radius of $r = 7.5$ mm had to be measured from two perpendicular directions in a plane perpendicular to the cylinder rotational axis. The working distance was given by the setup and amounted $WD = 28.2$ mm. This task required finding a working range where the interference intensities are insensitive to displacements and, at the same time, have a high contrast. In order to find an appropriate range, the interference signal was calculated as a function of the working distance WD and the distance d_{fl} between the fiber and lens, as shown in figure 4.15. For the given working distance, this plot allows finding a matching fiber to lens distance. Once a good range is determined, the sensor head must be adjusted

to this fiber to lens distance. This can be achieved using the plane mirror relation shown in figure 4.12. For the determined fiber to lens distance, one has to read off the corresponding working distance. Then, a cavity with this specific working distance is set up and the sensor head fiber to lens distance is adjusted to produce a focus at the mirror by maximizing the reflected signal.

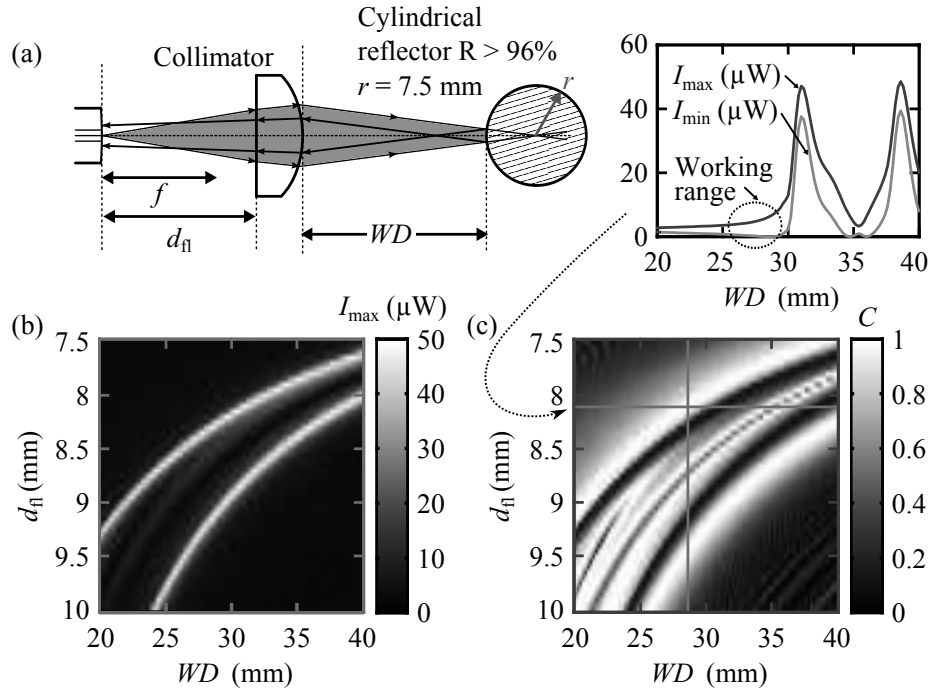


Figure 4.15: Measurement of the wobble of a rotating cylinder with the focused beam configuration shown in (a). An appropriate measurement range has a high contrast and the interference intensities are insensitive to displacements. It is determined from the intensity distribution I in (b) and from the interference contrast C in (c), which are both shown as a function of working distance WD and the fiber to lens distance d_f . Note that (b) allows only to display the constructive interference intensity I_{\max} .

4.7 Summary

This chapter has shown that the low-finesse fiber-optic Fabry-Pérot interferometer is suitable for displacement sensing in a wide range of applications by using different configurations of the sensing cavity. The interferometer enables remote sensing by means of optical fibers and is, therefore, well suited to work in extreme environments like cryogenic temperatures, ultra high vacuum or high magnetic fields. The possi-

4.7. SUMMARY

ble working ranges and angular alignment tolerances of the presented configurations of the Fabry-Pérot cavity have been characterized experimentally and theoretically with respect to the interference contrast which is a measure for the signal quality. The results can give assistance in finding the right sensor head configuration for the desired application. For theoretical characterization of the optical response of the Fabry-Pérot interferometer, a simulation method based on the combination of the Airy formula with the coupling efficiency calculation provided by Zemax was introduced. The good agreement between measurements and simulations demonstrate that this method is well suited to predict the optical response of arbitrary future sensor head configurations. This simplifies the customization of sensor heads as well as the development of new sensor heads as it reduces the time for prototyping and testing. In this way, several new sensor head designs have already been realized, as shown in figure 4.16. The simple structure of the sensor head allows miniaturization down to a diameter of currently 1.2 mm.



Figure 4.16: Experimental implementation of different types of sensor heads. Sensor heads “M12” and “M15.5” provide a collimated beam and are used in the single pass mode for measurements over several meters or in the double pass mode to achieve a high alignment tolerance. In contrast to the “M12” head, the “M15.5” head has an integrated flex structure for angular alignment. The miniature sensor heads “xs” and “xxs” have a diameter of 4 mm and 1.2 mm, respectively, and provide a focused beam. They are used for measurements on targets with various reflectivities.

The investigation of different configurations of the Fabry-Pérot cavity has shown that small size sensor heads are realized by placing a bare fiber close to a high reflec-

tive mirror. Best signal contrast is obtained at a distance of about 0.3 mm, with a measurement range in the order of a hundred microns and an angle tolerance of more than $\pm 2^\circ$. By using a confocal double pass arrangement comprising a collimator, the measurement range can be expanded to at least 100 mm, while ensuring a good alignment tolerance. The position dependent angular alignment tolerance around the expected normal incidence angle is ranging from $\pm 1^\circ$ at minimum distance to about $\pm 0.2^\circ$ at maximum distance. This arrangement makes the interferometer easy to use and insensitive to lateral displacements of the moving target. However, this enhancement of the alignment tolerance is at the expense of linearity. Calculations of the geometrical nonlinearities have revealed a total error of 110 μm when the target is displaced at a tilt of $\alpha = 0.2^\circ$ over the full double pass range of 100 mm. For further extending the measurement range up to 1 m, a high reflective corner cube can be used as target reflector, but with a reduced contrast of about 0.4 for normal incidence, which is still more than good enough for any practical devices. The use of a focusing lens, moreover, allows the measurement to be made on rough, low reflective or small targets and enables a measurement range ranging from hundreds of microns to several millimeters, depending on the reflectivity and the degree of beam focusing. A high target reflectivity can be compensated by a reduction of the fiber coupling efficiency, which is practically realized by defocusing of the target.

Future work should evaluate the dependence of the displacement measurement resolution and accuracy on coupling efficiency changes in order to further specify the signal within the possible working ranges. It further should deal with the correction of nonlinearities arising from the Fabry-Pérot cavity.

5 Absolute distance sensing

Laser interferometers are used for position tracking when the combination of high accuracy, nanometer sensitivity and long range displacement is required simultaneously. They are relying on the accurate pitch length provided naturally by the laser wavelength. A displacement is determined by counting and recording the number of pitches experienced during the target motion while measuring accurately and sensitively the last fraction of pitch at the time the measurement is recorded. In essence, most laser interferometers allow only for an absolute position measurement within a wavelength fraction and rely on counting and memorizing the number of pitches detected during displacement to reconstruct the full target displacement and position. Interrupting a laser interferometer measurement, albeit intentionally or accidentally, leads to the loss of position should the target subsequently drift away by more than a pitch length. In many instances, the loss of position and displacement information is very detrimental, in particular in systems where accessibility is much reduced and fine alignment is critical. Typical situations are that of position stages located in ultra-high vacuum like in synchrotron beamlines or in remote locations like on board of satellites or probes. Even in much less extreme situations, knowing for instance the precise position of a tool or a work piece on a milling machine upon powering it on, and this without having to initialize the xyz stages by displacement to a preset origin, is very much desirable. Apart from pure positioning applications, the knowledge of the absolute distance is also prerequisite for accurate distance sensing in ambient conditions, as already demonstrated in the environmental compensation algorithm in section 3.8. It can further be used for dynamic open loop adjustment of both the wavelength modulation amplitude and the demodulator phase.

There are a number of ways to combine dual or multi-wavelength interferometer to create much larger effective pitches, but ultimately the issue of determining the absolute distance remains.[67, 68, 69, 70] The use of frequency combs has lead to a significant progress of this technique in the last years, providing an uncertainty of up

to 10^{-13} without ambiguity, but at the expense of system complexity and for now very high costs.[71, 72] A different approach to interferometric absolute distance measurement is called variable-wavelength interferometry or frequency tuning interferometry (FTI) and is based on the ability to tune the laser wavelength.[73, 74, 75] However, the frequency tuning range required in order to measure a distance in the sub-meter range within nanometer accuracy, makes the laser system prohibitively expensive. The tuning range obtained by temperature adjustment of typical commercial semiconductor laser diodes allows an uncertainty in the micrometer range only.

The approach used in this chapter combines the use of frequency tuning interferometry with dual wavelength interferometry and establishes this way a novel method for absolute distance sensing without ambiguity limitation. In particular, a robust and industry scalable fiber-optic Fabry-Pérot miniature interferometer is presented, which is capable of measuring absolute distances with nanometer repeatability.

5.1 Principle of measuring absolute distances

In a Michelson or Fabry-Pérot interferometer, the absolute distance between a reference mirror and a target mirror is only known if the interference order is determined. This is the fundamental limitation of single fixed wavelength interferometers, in which the phase difference between the reference beam and target beam is only known modulo 2π . The use of two independent laser sources with the wavelengths λ_a and λ_b can help reducing the ambiguity of the interference order in that the interference signal shows a periodic beating pattern as a function of the distance. In this section, two different approaches for two laser absolute distance sensing will be presented. They are referred to as synthetic wavelength approach and combinatory fringe number approach.

5.1.1 Synthetic Wavelength Approach

The beating generated by using two different wavelengths can be viewed as a synthetic wavelength that is typically much longer than λ_a or λ_b , when the two wavelengths are chosen to be relatively close to each other. The ambiguity on the synthetic interference order is fully eliminated when the beating wavelength can be made long enough to fall within the uncertainty range of an independent but much less accurate

measurement of the distance. Here, such a measurement is conveniently realized by sweeping the laser wavelength of one laser over few nanometer, typically providing an absolute distance with micrometer uncertainty.[76, 77] However, the uncertainty of the wavelength sweep measurement is increased when the target moves during the wavelength sweep, e.g. due to target position drifts. This problem is solved by tracking target movements during the wavelength sweep by means of the second laser and correcting the phase data accordingly.[75, 74, 78]

Based on this concept, a three step procedure successively increasing the accuracy of the absolute distance computation has been implemented. The procedure is well suited to work with a fiber-optic Fabry-Pérot interferometer operated with two laser sources, one of which is at least tunable. In the following, this procedure is described. The index “a” and “b” refers to Laser A and B, respectively.

5.1.1.1 Frequency tuning interferometry

The first step provides a coarse absolute distance x_{fti} by sweeping the wavelength of one laser by an amount $\Delta\lambda$. [79] The interference phase Φ is in general given by

$$\Phi = \frac{4p\pi n}{\lambda}x, \quad (5.1)$$

where n is the refractive index of the medium in the cavity, p is the folding order of the cavity (1, 2, 3, ...) and x is the absolute distance to be measured, which is the distance between the fiber end and a movable reflector, both forming a Fabry-Pérot cavity with a length of $l = p \cdot x$. A confocal Fabry-Pérot cavity arrangement, by way of example, might include a folding mirror which effectively doubles the optical beam path, resulting in the folding order $p = 2$. [4] When changing the wavelength λ of the light, the interference phase experiences a change $\Delta\Phi$ which is proportional to the optical path difference of the interferometer. The absolute distance x_{fti} obtained from frequency tuning interferometry is expressed as

$$x_{\text{fti}} = \frac{\Lambda_a}{4p\pi n_a} \Delta\Phi_a, \quad (5.2)$$

where $\Delta\Phi_a = \Phi_{a,s} - \Phi_{a,e}$ is the phase change induced when sweeping the laser wavelength of Laser A from the start wavelength $\lambda_{a,s}$ to the end wavelength $\lambda_{a,e}$ by an amount $\Delta\lambda = \lambda_{a,e} - \lambda_{a,s}$. n_a is the refractive index which is assumed to be constant in the given wavelength range. Λ_a is an effective wavelength given by

$$\Lambda_a = \frac{\lambda_{a,s}\lambda_{a,e}}{\lambda_{a,s} - \lambda_{a,e}}. \quad (5.3)$$

The uncertainty δx_{fti} of this measurement mainly depends on factors like target drifts δx_{drift} during the wavelength sweep, wavelength uncertainties $\delta\lambda$, phase nonlinearities $\delta\Phi_{\text{NL}}$ and phase noise $\delta\Phi_{\text{noise}}$. Phase nonlinearity occurs when the interference fringe intensity departs from a strict cosine or sine form as a function of the cavity length. The total error can be estimated using the relation

$$\delta x_{\text{fti}} = \frac{\Lambda_a}{\lambda_{a,e}} \delta x_{\text{drift}} + \frac{\Lambda_a}{\lambda_{a,s}^2} x \delta\lambda + \frac{\Lambda_a}{4p\pi n_a} (\delta\Phi_{\text{NL}} + \delta\Phi_{\text{noise}}). \quad (5.4)$$

The most significant error is usually produced by cavity drifts during the wavelength sweep. Due to the large effective wavelength Λ_a , δx_{drift} is amplified with a leverage factor of $\Lambda_a/\lambda_{a,s}$, which is typically in the order of 10^3 . The second stabilized laser (Laser B) is used to track target drifts and the phase change measured with Laser A is corrected by these drifts. The cavity drifts are considered in equation 5.2 by subtracting the phase change measured with Laser B, yielding

$$x_{\text{fti}} = \frac{\Lambda_a}{4\pi p n_a} \left(\Delta\Phi_a - \frac{n_a \lambda_b}{n_b \lambda_{a,e}} \Delta\Phi_b \right). \quad (5.5)$$

5.1.1.2 Synthetic wavelength

In the second step, the result x_{fti} is used to determine the beating wavelength fringe number N_Λ and to determine an intermediate coarse value of the initial absolute distance, $x_{\Lambda,s}$. [76] N_Λ is the maximum number of integer beating wavelengths that fit into the optical beam path within the cavity and is expressed using the floor function, which returns the largest integer not greater than its argument, according to

$$N_{\Lambda,s} = \left\lfloor \frac{2p}{\Lambda_s} x_{\text{fti}} - \frac{\Phi_{\Lambda,s} \bmod 2\pi}{2\pi} + \frac{1}{2} \right\rfloor, \quad (5.6)$$

where Λ_s is the beating wavelength with respect to the start wavelength $\lambda_{a,s}$, given by

$$\Lambda_s = \frac{\lambda_b \lambda_{a,s}}{n_a \lambda_b - n_b \lambda_{a,s}}, \quad (5.7)$$

and $\Phi_{\Lambda,s}$ is the corresponding beating phase, given by

$$\Phi_{\Lambda,s} = \Phi_{a,s} - \Phi_b = \left(\frac{4p\pi n_a}{\lambda_{a,s}} - \frac{4p\pi n_b}{\lambda_b} \right) x = \frac{4p\pi x}{\Lambda_s}. \quad (5.8)$$

By way of example, $\lambda_{a,s}$ was used as the wavelength for Laser A, but $\lambda_{a,e}$ could have equally well been chosen, resulting in a beating wavelength Λ_e and a beating phase

$\Phi_{a,e}$, provided that the following equations are adapted accordingly. The absolute distance δx_{fti} obtained from the wavelength sweep must fulfill the condition

$$\delta x_{fti} < \Lambda_s/2p \quad (5.9)$$

in order to determine $N_{\Lambda,s}$ without ambiguity. This condition sets a lower limit to the choice of a convenient Λ_s . In particular, Λ_s should be chosen just long enough so that it still fulfills the condition. The absolute distance $x_{\Lambda,s}$ derived from the beating phase $\Phi_{\Lambda,s}$ then becomes

$$x_{\Lambda,s} = \left(N_{\Lambda,s} + \frac{\Phi_{\Lambda,s} \bmod 2\pi}{2\pi} \right) \frac{\Lambda_s}{2p}. \quad (5.10)$$

5.1.1.3 Fringe number assignment

In the third and final step, $x_{\Lambda,s}$ is used to determine the interference order N_a or N_b of one of the two lasers, in this case the fringe number $N_{a,s}$ corresponding to Laser A at the wavelength $\lambda_{a,s}$, yielding

$$N_{a,s} = \left\lfloor \frac{2pn_a}{\lambda_{a,s}} x_{\Lambda,s} - \frac{\Phi_{a,s} \bmod 2\pi}{2\pi} + \frac{1}{2} \right\rfloor. \quad (5.11)$$

This last assignment step is necessary because the uncertainty of $x_{\Lambda,s}$ in the experimental setup is in the order of $\lambda_{a,s}/2p$. To ensure again the unambiguity of $N_{a,s}$, the uncertainty $\delta\Phi_{\Lambda,s}$ must fulfill the condition

$$\delta\Phi_{\Lambda,s} < 2\pi\lambda_{a,s}/\Lambda_s. \quad (5.12)$$

As will be shown in the following paragraphs, this condition can only be met in the experimental setup when correcting periodic phase nonlinearities inherent to this kind of interferometer system (see section 5.2.2). The high precision absolute distance x is then given by

$$x = \left(N_{a,s} + \frac{\Phi_{a,s} \bmod 2\pi}{2\pi} \right) \frac{\lambda_{a,s}}{2pn_a}. \quad (5.13)$$

Equation 5.13 requires a relatively high wavelength accuracy in the order of $\delta\lambda/\lambda = 10^{-9}$. Practically, most applications do not need nanometer distance accuracy, but nanometer repeatability. In such cases, the requirement for wavelength accuracy can be relaxed, and the target distance is

$$x = N_{\Lambda,s} \frac{\Lambda_s}{2p} + \frac{\lambda_{a,s} \Phi_{a,s} \bmod 2\pi}{4p\pi n_a} + \left\lfloor \frac{\Lambda_s \Phi_{\Lambda,s} \bmod 2\pi}{2\pi\lambda_{a,s}} - \frac{\Phi_{a,s} \bmod 2\pi}{2\pi} + \frac{1}{2} \right\rfloor \frac{\lambda_{a,s}}{2pn_a}. \quad (5.14)$$

When only a high repeatability is required, it is sufficient to know $N_{\Lambda,s}$ and to count the number of interference fringes N_a^* within the fractional part of $\Phi_{\Lambda,s}$, expressed by the floor function term. The absolute knowledge of N_a is not necessary. This enables repeatable absolute distance measurements also for wavelength accuracies in the $\delta\lambda/\lambda = 10^{-8}$ range, which is typically achieved in the present case.

After determination of the absolute distance, the system outputs a continuous position by adding the displacement measured with the displacement tracking Laser B from the start of the measurement, yielding

$$x(t) = x + \Delta x(t) = x + \frac{\lambda_b}{4p\pi n_b} \Delta\Phi_b(t). \quad (5.15)$$

5.1.2 Combinatory Fringe Number Approach

The combinatory fringe number approach provides another scheme to compute a high accuracy absolute position x . In contrast to the synthetic wavelength approach, no beating wavelength is required. Generally, this approach uses an extremum principle for determining the high accuracy absolute position x . This method, also known as method of excess fractions or method of exact fractions, relies on the fractions ϵ of the interference fringes of two or more laser wavelengths.[80, 81] It is based on recording fractional values of the interferometric phases of both laser lights at the start and/or stop points of defined wavelength sweeps, on establishing one or more sets of fringe number combinations based on a coarse knowledge of an absolute position and on applying an extremum principle for electing a specific fringe number combination from each of the sets of fringe number combinations. These steps will be described in the following sections.

5.1.2.1 Determining fractional phases

In a first step, the laser wavelengths of Laser A and Laser B are stabilized to the known start wavelengths $\lambda_{a,s}$ and $\lambda_{b,s}$, respectively. As soon as the start wavelengths are reached, the fractional values $\Phi_{a,s} \bmod 2\pi = 2\pi\epsilon_{a,s}$ and $\Phi_{b,s} \bmod 2\pi = 2\pi\epsilon_{b,s}$ of the interferometric phases are measured and recorded. The absolute phases (i.e. the start fringe numbers $N_{a,s}$ and $N_{b,s}$) are unknown but the start fractional phase values $2\pi\epsilon_{a,s}$ and $2\pi\epsilon_{b,s}$ are measured with high interferometric precision.

5.1.2.2 Laser wavelength sweep

In a subsequent process, the wavelength λ_a of Laser A is shifted continuously from $\lambda_{a,s}$ to another precisely known wavelength $\lambda_{a,e}$. At the same time, the wavelength λ_b of Laser B is maintained at a constant and exact value, e.g. at its stabilized start value $\lambda_{b,s}$. The shift of the wavelength of Laser A is performed slow enough so that the corresponding interferometric phase shift $\Delta\Phi_a$ can be measured. During the operation of shifting the wavelength of Laser A, the associated phase shift is continuously recorded until the laser wavelength has reached its stable exact end value $\lambda_{a,e}$. When the wavelength λ_a has reached its end value $\lambda_{a,e}$, both the single value $\Delta\Phi_a$ of the phase displacement of the light of Laser A during the wavelength sweep as well as the single value $\Delta\Phi_b$ of the phase displacement of the light of Laser B during the wavelength sweep are recorded. Because the wavelength λ_b has been kept constant during this operation, a non-zero phase displacement $\Delta\Phi_b$ will be solely due to a change Δx in the cavity length x . In contrast, the phase displacement $\Delta\Phi_a$ results both from the intended wavelength shift caused by the wavelength sweep and from any change Δx in the cavity length.

5.1.2.3 Computation of a coarse absolute distance

In a further process, the values x and Δx of the cavity length and the change in the cavity length that occurred during the first laser wavelength sweep are computed by using some of the following equations:

$$\Phi_{a,s} = \frac{4\pi p n_a}{\lambda_{a,s}} x \quad (5.16)$$

$$\Phi_{a,e} = \frac{4\pi p n_a}{\lambda_{a,s} + \delta\lambda_{a,fti}} (x + \Delta x) \quad (5.17)$$

$$\Phi_{b,s} = \frac{4\pi p n_b}{\lambda_b} x \quad (5.18)$$

$$\Phi_{b,e} = \frac{4\pi p n_b}{\lambda_b} (x + \Delta x) \quad (5.19)$$

$$\Delta\Phi_a = \Phi_{a,e} - \Phi_{a,s} \quad (5.20)$$

$$\Delta\Phi_b = \Phi_{b,e} - \Phi_{b,s} \quad (5.21)$$

This is a system of six unknown quantities $\Phi_{a,s}$, $\Phi_{a,e}$, $\Phi_{b,s}$, $\Phi_{b,e}$, x , and Δx . From equation 5.21 the displacement Δx in the cavity length that occurred during the

wavelength shift is calculated according to

$$\delta x = \frac{\lambda_b}{4\pi p n_a} \Delta\Phi_b, \quad (5.22)$$

which is typically accurate within nanometers. The cavity length x (absolute position x) at the initial measurement is

$$x = \frac{\Lambda_a}{4\pi p n_a} \left(\Delta\Phi_a - \frac{\lambda_b}{\lambda_{a,e}} \Delta\Phi_b \right), \quad (5.23)$$

where the effective wavelength Λ_a is given by

$$\Lambda_a = \frac{\lambda_{a,s} \lambda_{a,e}}{\lambda_{a,s} - \lambda_{a,e}}. \quad (5.24)$$

From a mathematical point of view, equation 5.23 already solves the problem. However, in reality the measured values of $\Delta\Phi_a$ and $\Delta\Phi_b$ may not be sufficiently exact and may deviate from the reality due to phase noise and other measurement errors inherent to interferometric displacement sensing. It must be noted that an error φ on the phase measurement leads to an error Σ on the position expressed by

$$\Sigma = \frac{\Lambda_a}{4\pi p n_a} \phi. \quad (5.25)$$

The effective wavelength Λ_a is significantly longer than $\lambda_{a,s}$ since the wavelength shift $\lambda_{a,e} - \lambda_{a,s}$ is typically only a small fraction of $\lambda_{a,s}$. In fact, the same phase error φ leads to an actual position error of

$$\sigma = \frac{\lambda_a}{4\pi p n_a} \phi. \quad (5.26)$$

In other words, the error on the evaluated position x is $\Sigma = \sigma(\Lambda_a/\lambda_{a,s}) = \sigma\lambda_{a,s}/(\lambda_{a,e} - \lambda_{a,s})$. This indicates an amplification of the error with a leverage factor of $\Lambda_a/\lambda_{a,s}$, which may be about 10^3 . That is, an actual position error of 10 nm would lead to an error of 10 μm of the evaluated absolute position x . Thus, the error of the evaluated absolute position x may be far larger than the measurement pitch of $\lambda_a/2p$. Therefore, in reality, equation 5.23 may only provide for a coarse estimation of the absolute position x .

5.1.2.4 Computation of an accurate absolute distance

In a further process, some others of the equations 5.16 - 5.21 are exploited to reduce an error on the evaluation of x . As it is possible to measure the fractional parts of

5.1. PRINCIPLE OF MEASURING ABSOLUTE DISTANCES

the phases $\epsilon_{a,s}$, $\epsilon_{a,e}$, $\epsilon_{b,s}$, $\epsilon_{b,e}$ within the measurement pitch, the following equations may be used:

$$\Phi_{a,s} = 2\pi(N_{a,s} + \epsilon_{a,s}) \quad (5.27)$$

$$\Phi_{a,e} = 2\pi(N_{a,e} + \epsilon_{a,e}) \quad (5.28)$$

$$\Phi_{b,s} = 2\pi(N_{b,s} + \epsilon_{b,s}) \quad (5.29)$$

$$\Phi_{b,e} = 2\pi(N_{b,e} + \epsilon_{b,e}) \quad (5.30)$$

Unknown are the integer fringe numbers $N_{a,s}$, $N_{a,e}$, $N_{b,s}$, $N_{b,e}$, which are also referred to as the interference orders in this work. Combining these equations with equations 5.16-5.19, the following equations are obtained.

$$N_{a,s} + \epsilon_{a,s} = \frac{2pn_a}{\lambda_{a,s}}x \quad (5.31)$$

$$N_{a,e} + \epsilon_{a,e} = \frac{2pn_a}{\lambda_{a,s} + \delta\lambda_{a,fti}}(x + \delta x) \quad (5.32)$$

$$N_{b,s} + \epsilon_{b,s} = \frac{2pn_b}{\lambda_b}x \quad (5.33)$$

$$N_{b,e} + \epsilon_{b,e} = \frac{2pn_b}{\lambda_b}(x + \delta x) \quad (5.34)$$

A coarse absolute position value of x is then input into the equations 5.31 and 5.33 in order to get coarse values of the fringe numbers $N_{a,s}$, $N_{b,s}$. Then, possible combinations $[N_{a,s}|N_{b,s}]$ of fringe numbers are formed. As the typical uncertainty on the fringe numbers $N_{a,s}$ and $N_{b,s}$ at the start are known (e.g. plus or minus a known integer M), the set of all possible combinations of $[N_{a,s}|N_{b,s}]$ are given by the fringe number combinations lying around the coarse values of $N_{a,s}$, $N_{b,s}$ within the tolerance of M , respectively. Then, the term

$$(N_{a,s} + \epsilon_{a,s})\frac{\lambda_{a,s}}{2p} - (N_{b,s} + \epsilon_{b,s})\frac{\lambda_{b,s}}{2p} \quad (5.35)$$

is calculated, which is the condition of eliminating x between equations 5.31 and 5.33. The combination $[N'_{a,s}|N'_{b,s}]$ for which

$$(N_{a,s} + \epsilon_{a,s})\frac{\lambda_{a,s}}{2p} - (N_{b,s} + \epsilon_{b,s})\frac{\lambda_{b,s}}{2p} \rightarrow 0 \quad (5.36)$$

is 0 or closest to 0 of all possible combinations $[N_{a,s}|N_{b,s}]$ is determined. Then, based on this minimum combination $[N'_{a,s}|N'_{b,s}]$, an accurate value of the absolute

position x is calculated from equation 5.31 or 5.33. In other words, equation 5.36 is minimized over all possible combinations of $[N_{a,s}|N_{b,s}]$ in order to determine the minimum combination $[N'_{a,s}|N'_{b,s}]$. The minimum combination $[N'_{a,s}|N'_{b,s}]$ provides the unknown value of x with high accuracy.

5.1.2.5 Consistency check

In order to obtain confirmation about the value of x , some others of the equations 5.31 - 5.34, namely equations 5.32 and 5.34, may be exploited to compute an accurate value of the absolute position of x . After having determined the start fractional values $2\pi\epsilon_{a,s}$ and $2\pi\epsilon_{b,s}$ of both interferometric phases, a frequency sweep of Laser A and a frequency sweep of Laser B are performed to deliver two sets of data, which may then be exploited to compute an accurate value of x in different ways. At the end of the frequency sweep of Laser A, the end fractional value $2\pi\epsilon_{a,e}$ of the interferometric phase is recorded. The frequency sweep of Laser B is performed after the end of the frequency sweep of Laser A. The wavelength of Laser B is shifted continuously to another precisely known wavelength value $\lambda_{b,e}$. At the same time, the wavelength λ_a of laser A is maintained at a constant and exact value, e.g. at its stabilized end value $\lambda_{a,e}$. Shifting the wavelength of Laser B is performed slow enough so that the corresponding interferometric phase shift can be measured. At the end of the frequency sweep of the Laser B, the end fractional value $2\pi\epsilon_{b,e}$ of the interferometric phase is recorded. Thus, the absolute phases (i.e. the end fringe numbers $N_{a,e}$ and $N_{b,e}$) are unknown but the end fractional values $2\pi\epsilon_{a,e}$ and $2\pi\epsilon_{b,e}$ of the interferometric phases may be measured with high interferometric precision. A coarse absolute position value of x is then input into equations 5.32 and 5.34 to get coarse values of the fringe numbers $N_{a,e}$ and $N_{b,e}$. Then, possible combinations of $[N_{a,e}|N_{b,e}]$ are established and again, the combination $[N'_{a,e}|N'_{b,e}]$ for which

$$(N_{a,e} + \epsilon_{a,e})\frac{\lambda_{a,e}}{2p} - (N_{b,e} + \epsilon_{b,e})\frac{\lambda_{b,e}}{2p} \rightarrow 0 \quad (5.37)$$

is determined. Then, based on this minimum combination $[N'_{a,e}|N'_{b,e}]$, an accurate value of the absolute position x is calculated from equation 5.33 or 5.34. In other words, equation 5.37 is minimized over all possible combinations of $[N_{a,e}|N_{b,e}]$ in order to determine the minimum combination $[N'_{a,e}|N'_{b,e}]$. The minimum combination $[N'_{a,e}|N'_{b,e}]$ provides the unknown value of x with high accuracy based e.g. on equation 5.33 or 5.34.

Based on the sets of possible combinations or on the absolute position values x obtained through equation 5.36 and 5.37, a consistency check may be performed. If the accurate absolute position value x from equation 5.36 and the accurate absolute position value x from equation 5.37 differ by more than a predetermined threshold, e.g. $\lambda/4p$, a measurement error will be assumed.

5.2 Instrumentation

The fiber-optic Fabry-Pérot interferometer setup is schematically shown in figure 5.1. At the core of the system are two tunable distributed feedback lasers, Laser A and B, emitting light with the wavelength λ_a and λ_b , respectively. Both lasers were bought from TOPTICA Photonics AG and included a laser head (Toptica DL DFB BFY), a supply rack (SYS DC 110 R 19"), an analog interface board (DCB 110) for the external change of the laser temperature, and a modulation circuit board (DL-MOD/DFB) with field-effect transistor and Bias-T for the high frequency current modulation. The tuning range of these semiconductor diode lasers is in the order of $\Delta\lambda/\lambda = 10^{-3}$. The dependence of the laser wavelength from the laser current is typically in the order of 8 pm/mA and the dependence from the laser temperature is in the order of 0.12 nm/K. Laser A is connected to a first two-by-two directional fiber coupler (FC1) and Laser B is connected to a second two-by-two directional fiber coupler (FC2). Both the first and the second coupler provide an output to a third two-by-two directional fiber coupler (FC3), which is used to mix the light of both sources. The two-wavelength light is routed to a fourth two-by-two directional fiber coupler (FC4), whose first output forms the optical output of the interferometer. A fiber patch cable connects the interferometer with the all-optical sensor head and enables remote sensing. The measurements in this chapter have been performed with a sensor head in a confocal double pass arrangement. The cavity had a length of $x = 115$ mm and was placed inside a vacuum chamber. The Fabry-Pérot interferometer has the advantage that the computation of the absolute distance is performed without the use of any reference length or length standard which are sometimes required in other absolute distance interferometers.[82] This is because the absolute distance is equal to the distance between the movable reflector and the fiber end face and is therefore independent from any reference length that might be subject to thermal drift.[6] When displacing the target, the detector outputs a beating interference pattern rather than a sinusoidal

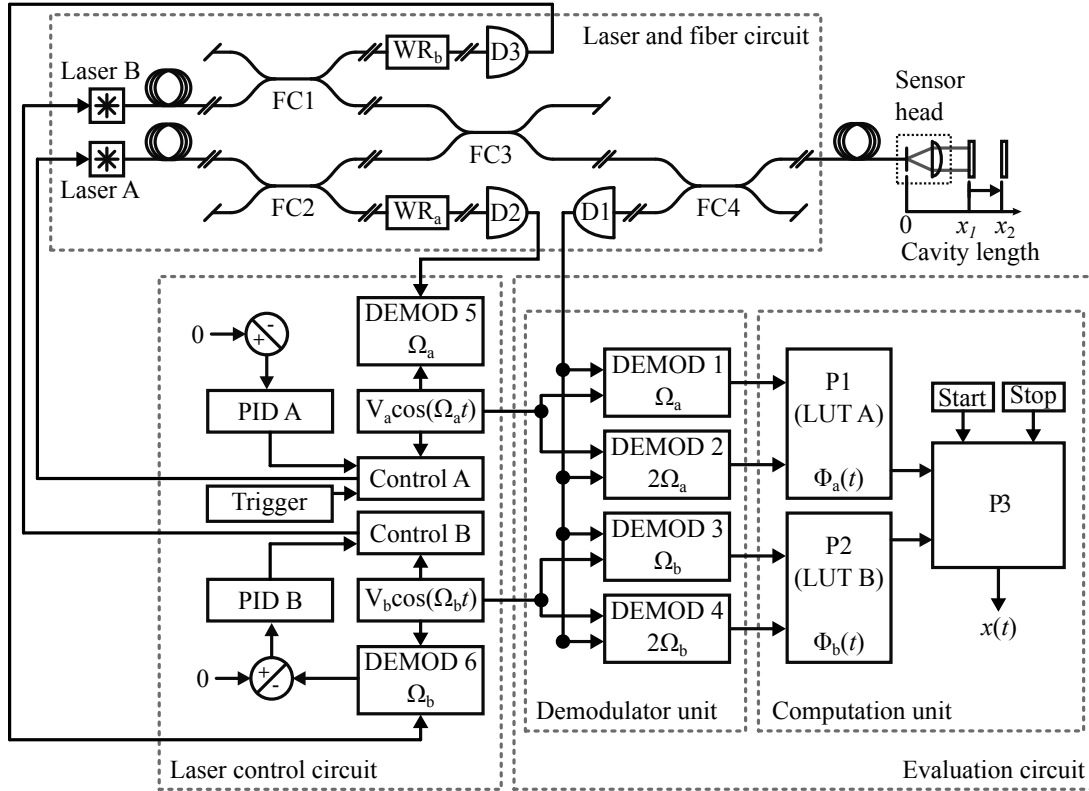


Figure 5.1: Dual laser interferometer setup for the measurement of absolute distances using a low-finesse Fabry-Pérot cavity. The light from two tunable lasers (Laser A and B) is mixed in the fiber circuit and routed to the sensing cavity which is formed between the fiber endface of the sensor head and the movable reflector. The fiber circuit moreover comprises two molecular absorption gas cells (WR_a and WR_b) for laser wavelength stabilization. The laser control circuit controls the wavelength of both lasers based on the control of the laser current and temperature. The evaluation circuit, comprising demodulator unit and computation unit, computes the absolute distance x .

interference pattern. The separation and recovery of the reflected interference signals is achieved with a quadrature detection method which is described in the following section.

5.2.1 Quadrature detection

The separation of both laser signals and the recovery of the interference phases of both lasers could be realized using optical filters, but with the drawback of increasing system complexity and costs and reduced signal stability. To overcome these limitations, the phase information is encoded by different wavelength modulation frequencies of

both lasers, a technique often referred to as frequency division multiplexing.[61] The light emitted from Laser A with the wavelength λ_a is modulated with the frequency $\Omega_a = 2\pi f_a$ and the light emitted from Laser B with the wavelength λ_b is modulated with the frequency $\Omega_b = 2\pi f_b$. The wavelength modulation is provided by two oscillators generating the signals $V_a \cos \Omega_a t$ and $V_b \cos \Omega_b t$. For an ideal Michelson interferometer, the detector signal at D1 is a superposition of signals represented by

$$\begin{aligned} I(\Phi_a, \Phi_b) = & I_{0,a} + I_{0,b} + \\ & C_a \cos(\delta\Phi_a \sin \Omega_a t + \Phi_a) + \\ & C_b \cos(\delta\Phi_b \sin \Omega_b t + \Phi_b), \end{aligned} \quad (5.38)$$

where $\delta\Phi$ is the modulation depth given by $\delta\Phi = -4p\pi n x \delta\lambda / \lambda^2$. The total interference detector signal at D1 is therefore a composition of different time dependent signals which carry the phase information of both interference phases. They can be distinguished by their modulation frequency according to

$$I = I_{0,a} + I_{0,b} + I_{\Omega_a} + I_{2\Omega_a} + I_{\Omega_b} + I_{2\Omega_b} + \dots \quad (5.39)$$

By lock-in demodulation of the interferometer detector signal D1 at the fundamental modulation frequencies Ω_a and Ω_b and their harmonics $2\Omega_a$ and $2\Omega_b$, the signal amplitudes are recovered. The demodulated intensities in their first and second harmonic are given by decomposition of equation 5.38 in Bessel functions $J_i(\delta\Phi)$, yielding[61]

$$\begin{aligned} I_{\Omega_a} &= -I_{0,a} C_a J_1(\delta\Phi_a) \sin(\Omega_a t) \sin(\Phi_a) \\ I_{2\Omega_a} &= I_{0,a} C_a J_2(\delta\Phi_a) \cos(2\Omega_a t) \cos(\Phi_a) \\ I_{\Omega_b} &= -I_{0,b} C_b J_1(\delta\Phi_b) \sin(\Omega_b t) \sin(\Phi_b) \\ I_{2\Omega_b} &= I_{0,b} C_b J_2(\delta\Phi_b) \cos(2\Omega_b t) \cos(\Phi_b). \end{aligned} \quad (5.40)$$

The Ω and 2Ω components show to be conveniently in quadrature, i.e. 90° phase shifted. The detection of the amount and sign of the interference phase changes $\Delta\Phi_a$ and $\Delta\Phi_b$ with constant sensitivity is therefore achieved with a quadrature detection method requiring two sinusoidal signals phase shifted by 90° . [3, 26] Equal modulation amplitudes of the Ω and 2Ω components are obtained for a modulation depth of $\delta\Phi = 2.6$ rad, resulting in an equal sensitivity of both quadrature components.[61] However, this is not necessarily required because the amplitudes are normalized in a further process. Referring solely to the laser data sheet which specifies a current tuning rate of $\delta\lambda/\delta I_{\text{mod}} = 8$ pm/mA and a maximum modulation amplitude $\delta I_{\text{mod}} = \pm 1.5$ mA

and assuming a modulation depth of $\delta\Phi = 2.6$ rad, the minimum distance between fiber and target which is achievable in this setup is estimated to lie around 10 mm.

The interference phases can be recovered by lock-in demodulation, followed by normalization of the signal amplitudes and determination of the tangent between the Ω and 2Ω components. The interference phases Φ_a and Φ_b are then given by

$$\begin{aligned}\Phi_a &= \arctan(SQ_{\Omega_a}/S_{2\Omega_a}) \\ \Phi_b &= \arctan(SQ_{\Omega_b}/S_{2\Omega_b}),\end{aligned}\tag{5.41}$$

where $SQ_{\Omega_a} = -\sin \Phi_a$ and $SQ_{\Omega_b} = -\sin \Phi_b$ are the normalized amplitudes of the demodulation at the fundamental frequency Ω and $S_{2\Omega_a} = \cos \Phi_a$ and $S_{2\Omega_b} = \cos \Phi_b$ are the normalized amplitudes of the demodulation at the harmonic frequency 2Ω .

The normalized demodulated amplitudes and the corresponding interference phases

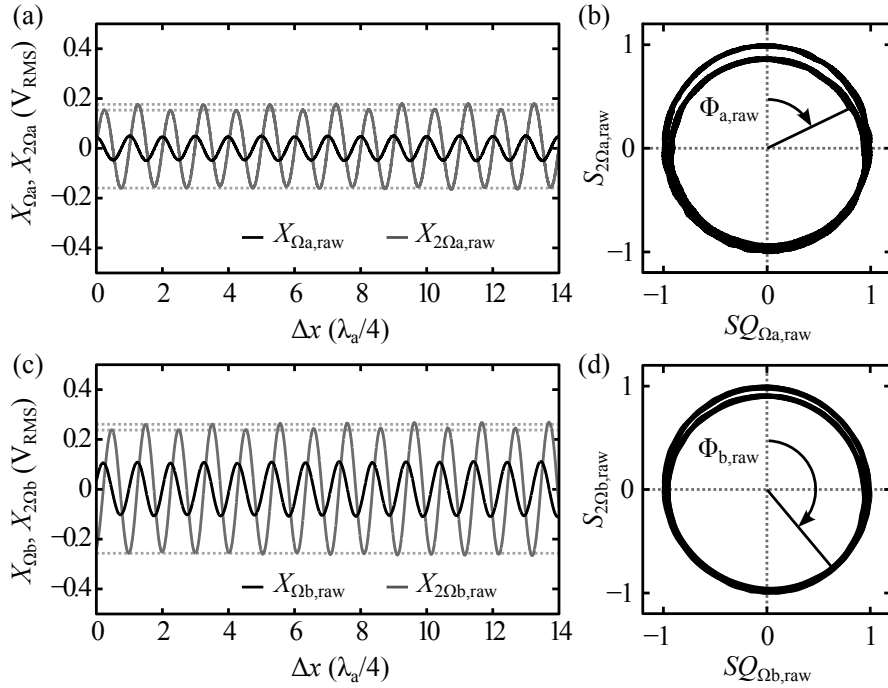


Figure 5.2: Wavelength demodulated signals of the interferometer detector signal D1 gained through demodulation at the frequencies Ω_a and $2\Omega_a$ (a) and Ω_b and $2\Omega_b$ (b). The signals were taken from a cavity placed in a vacuum while the target is displacing. The raw signals in (a) and (b) are normalized and plotted against each other to form the Lissajous figures in (c) and (d).

are obtained by continuously processing the signals from the demodulator unit in the processors P1 and P2. In our setup, the lock-ins DEMOD 1-4 are realized by a

digital lock-in amplifier (HF2LI Lock-in Amplifier, Zurich Instruments AG) which allows simultaneous demodulation of detector signal D1 at the four frequencies Ω_a , Ω_b , $2\Omega_a$ and $2\Omega_b$. The lock-in output raw signals for a drifting cavity in a vacuum, measured with Laser A and B, are shown in figure 5.2 (a) and (c), respectively, as a function of the cavity displacement Δx in units of $\lambda_a/4$. The signals $X_{\Omega_a, \text{raw}}$ and $X_{\Omega_b, \text{raw}}$ are obtained by demodulation at the first harmonic of the carrier frequency Ω_a and Ω_b , respectively. The signals $X_{2\Omega_a, \text{raw}}$ and $X_{2\Omega_b, \text{raw}}$ are obtained by demodulation at the second harmonic of the carrier frequency $2\Omega_a$ and $2\Omega_b$, respectively. The second harmonic modulation amplitude is in our experiment smaller than the first harmonic. This is because of the small modulation depth that was used for the measurements, leading to different modulation amplitudes according to the Bessel functions in equations 5.40. These signals are used in the next process to calculate the normalized demodulated signals which are expressed by $S_{2\Omega_a, \text{raw}} = X_{2\Omega_a, \text{raw}}/X_{2\Omega_a, \text{max}}$, $S_{2\Omega_b, \text{raw}} = X_{2\Omega_b, \text{raw}}/X_{2\Omega_b, \text{max}}$, $SQ_{\Omega_a, \text{raw}} = X_{\Omega_a, \text{raw}}/X_{\Omega_a, \text{max}}$ and $SQ_{\Omega_b, \text{raw}} = X_{\Omega_b, \text{raw}}/X_{\Omega_b, \text{max}}$, where the index “max” indicates maximum signal intensity. The maximum signal intensities are conveniently determined by sweeping the wavelength of both lasers which allows going through the interference pattern. Figures 5.2 (b) and (d) show the normalized Lissajous figures obtained through normalization of the lock-in demodulated signals and plotting the normalized first and second harmonic modulation amplitude against each other. The signals $X_{2\Omega_a, \text{raw}}$ and $X_{2\Omega_b, \text{raw}}$ show a clear 4π -periodic deviation from a cosine or sine form, causing undesired phase nonlinearities which might infringe the unambiguity condition stated in equation 5.12. The 4π -periodic deviations are only present in case of a double pass cavity. A single pass cavity would only produce 2π -periodic deviations, which would even simplify the correction process. In the Lissajous figure representation, phase nonlinearities show up in deviations from an ideal circle. In particular, for 4π -periodic nonlinearities the Lissajous figure shows a double trajectory. These nonlinearities occur at target tilt angles smaller than about ± 0.1 deg. In this range, the reflected spot falls onto the transition region between fiber core and cladding, causing part of the light to experience cavity folding and the other part not. In order to quantify the phase nonlinearities $\delta\Phi_{\text{NL}(a), \text{raw}}$ and $\delta\Phi_{\text{NL}(b), \text{raw}}$ related to Laser A and B, respectively, the raw voltage signals from the demodulators are first normalized and then converted into phases using equation 5.41. Then, a polynomial fit is subtracted from these phase data, yielding the nonlinearities represented by the gray curves in

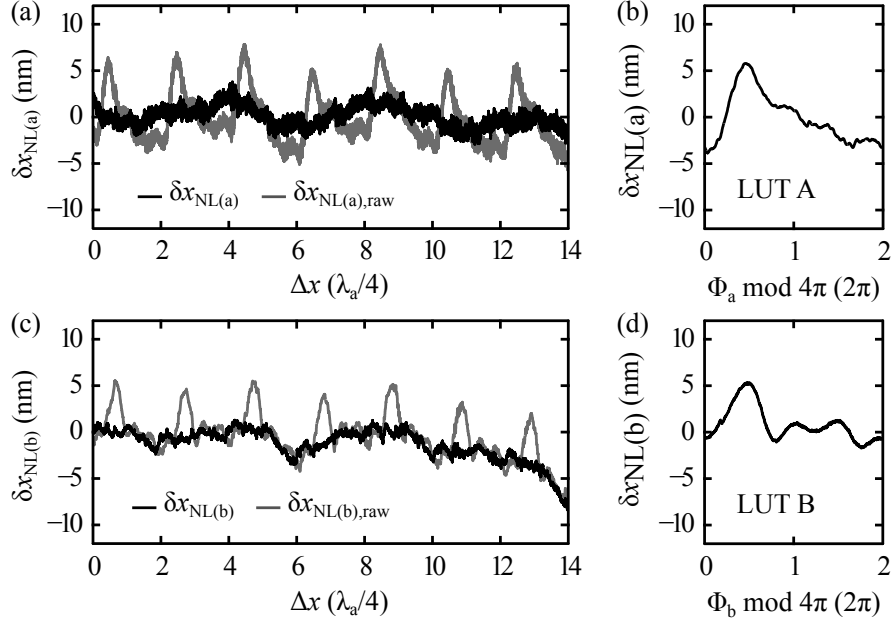


Figure 5.3: Periodic nonlinearities δx_{NL} as a function of the target displacement Δx measured with Laser A (a) and Laser B (b). The black line represents nonlinearities measured after correcting phases Φ_a and Φ_b by means of the 4π -periodic look-up tables LUT A (c) and LUT B (d) (phase nonlinearities are converted into displacements to simplify matters).

figure 5.3 (a) and (c). The phase nonlinearities are converted into displacements $\delta x_{NL(a),raw}$ and $\delta x_{NL(b),raw}$ for simplicity. In the present setup, such nonlinearities are too large for equation 5.12 to hold. Fortunately, however, the deterministic nature of these nonlinearities allows for their correction using a process which is presented in the next section.

5.2.2 Correction of periodic nonlinearities

The measurements with both lasers have shown that the interference phase is not linear but deviates periodically as a function of the actual displacement. Deterministic phase nonlinearities of up to about $\delta\Phi_{NL}/2\pi = 3 \cdot 10^{-2}$ have been measured in the interferometer system, corresponding to a displacement deviation of about $\delta x_{NL} = 13$ nm. These nonlinearities are too large to fulfill equation 5.12. Due to the unpredictability of some influences, nonlinearities are difficult to model analytically, although the changes arising from multiple reflections in the Fabry-Pérot cavity and from reflector misalignment are well understood.[83] For this reason, a self-calibrating technique is used to measure these deviations. In this approach, both laser wave-

lengths are swept monotonically and independently in order to predetermine the nonlinearities of both phases. The laser wavelength sweep induces a phase change of the interference signal which is recorded and stored for further processing. By subtracting a monotonic polynomial fit from the phase data, two 4π -periodic look-up tables (LUT A and LUT B), containing the periodic phase deviations from the actual phases Φ_a and Φ_b , are created and stored in P1 and P2, respectively.

In the experiment, the wavelength sweep is performed prior to the absolute distance computation by linearly ramping the laser temperature of both lasers by means of the wavelength control circuits Control A and B. This induces phase changes of several periods of 4π , allowing to improve the statistic of the look-up tables by averaging over all nonlinearities in the phase interval modulo 4π . The computation of LUT A and LUT B is performed in Processor P3. P3 makes a polynomial fit to the wavelength sweep phase data and subtracts this fit from the phase raw data. The differences are the nonlinearities, which are stored as a function of the fit phase data modulo an interval of 4π . The interval 4π is subdivided and all nonlinearities falling in a certain sub-interval are counted and averaged, yielding a relation between nonlinearities and fitted phase. To obtain the relation between measured raw phase and fit phase, the same procedure is repeated and the measured raw phase modulo 4π is stored as a function of the fit phase data modulo 4π , yielding a relation between measured raw phase data and fitted phase. In this way, a relation between nonlinearities and measured phase is established for both interference phases and stored in the look-up tables LUT A and LUT B, which are then used to correct the measured raw phases.

Processors P1 and P2 continuously calculate the phases $\Phi_{a,raw}$ and $\Phi_{b,raw}$ from the signals provided by the demodulator unit and correct these values by periodic nonlinearities. This is done by subtracting the values stored in the look-up tables LUT A and LUT B from the corresponding phase raw data. The nonlinearities after correction are represented by the black curves in figure 5.3 (a) and (c), demonstrating the reduction of the deviations from the actual displacement to about 2 nm. Both look-up tables used for the correction process are shown in figure 5.3 (b) and (d). The fact that both curves differ from each other suggests that not all nonlinearities have an optical background. Some nonlinearities might be caused by a non-sinusoidal wavelength modulation. The whole correction process is performed for initial adjustment of the interferometer, i.e. prior to the absolute distance measurement. The corrected phases Φ_a and Φ_b modulo 2π are shown for the thermally drifting cavity in

figure 5.4 (a).

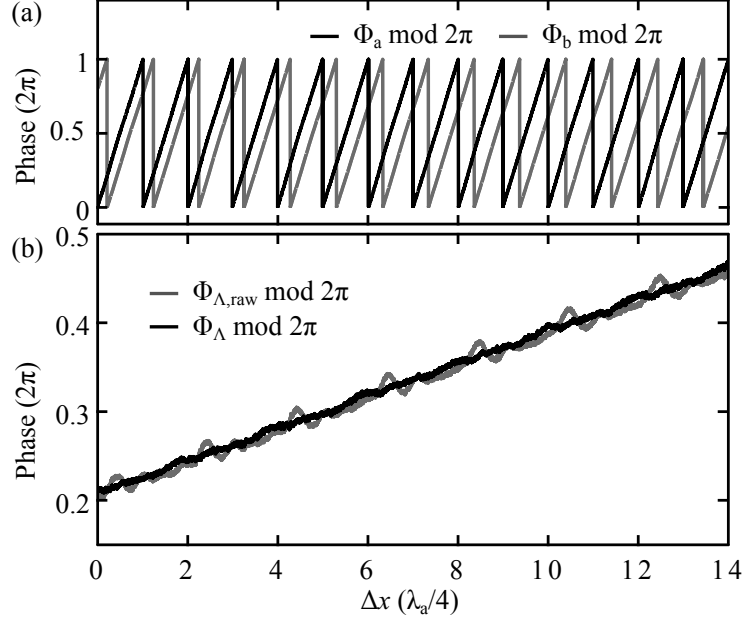


Figure 5.4: Interference phases Φ_a and Φ_b (a) and beating wavelength phase $\Phi_{\Lambda, s}$ (b) as a function of the target displacement Δx . (b) also shows the raw beating wavelength phase $\Phi_{\Lambda, \text{raw}}$ without correction of periodic nonlinearities.

For unambiguous determination of the absolute distance, the interferometer setup requires a measurement of the beating phase with an uncertainty of $\delta\Phi_{\Lambda, s}/2\pi < 15 \cdot 10^{-3}$, which was ensured by means of look-up table correction. The beating phase is given by the phase difference $\Phi_{\Lambda, s} = \Phi_a - \Phi_b$ and is shown for the same drifting cavity in figure 5.4 (b). The gray curve represents the measured raw values of the beating phase $\Phi_{\Lambda, \text{raw}}$, including the superimposition of the nonlinearities of both raw phases. The black curve represents the values of $\Phi_{\Lambda, s}$, where both phases are separately corrected for nonlinearities. The curves demonstrate that the nonlinearities of $\Phi_{\Lambda, s}$ could be reduced to about $\delta\Phi_{\Lambda, s}/2\pi = 6 \cdot 10^{-3}$, corresponding to a factor of about 3 to 4, meaning that $\delta\Phi_{\Lambda, s}$ now can hold the condition of equation 5.12.

5.2.3 Wavelength control

The measurement of absolute distances requires a high stability of both lasers which cannot be guaranteed only by current and temperature stabilization. Lasers A and B are therefore stabilized to the wavelength references WR_a and WR_b , respectively,

ensuring a wavelength stability in the order of $\delta\lambda/\lambda = 10^{-8}$. WR_a and WR_b are two low pressure gas cells with defined absorption lines, to which the laser wavelengths are locked. In our setup, the second output of the first fiber coupler is connected to the first gas cell WR_a (Acetylene 12) and the second output of the second fiber coupler is connected to the second gas cell WR_b (Acetylene 13). The laser wavelengths are controlled by the laser wavelength control circuits Control A and B, which enable wavelength stabilization as well as defined wavelength sweeps by controlling both the laser current and temperature. Wavelength sweeps are performed by changing the laser temperature. The laser temperature control can hold the laser wavelength within a certain wavelength interval, but not with the required wavelength accuracy. For that reason, defined wavelength sweeps are achieved by locking the laser wavelength to different absorption lines of the absorption gas. For wavelength stabilization, the laser wavelength is brought close to the desired absorption line by means of the laser temperature. A feedback loop which controls the more sensitive laser current then locks the wavelength to the desired absorption line.

The wavelength scan shown in figure 5.5 (a) is an example for the absorption spectrum of Acetylene 12 detected with D2, normalized to the transmittance T . The corresponding normalized demodulation signal $\partial T/\partial\lambda\cdot\delta\lambda$ is shown in figure 5.5 (b). In this example, the peak-to-peak wavelength modulation $\delta\lambda$ was about 0.7 pm. Figure 5.5 (c) shows the absorption spectrum of Acetylene 13 detected with D3. The corresponding normalized demodulation signal $\partial T/\partial\lambda\cdot\delta\lambda$ is shown in figure 5.5 (d). For the absolute distance measurement, the wavelength of Laser A was tuned between wavelength $\lambda_{a,s} = 1518.2131$ nm and $\lambda_{a,e} = 1514.7703$ nm, corresponding to absorption peak R(21) and R(13) of Acetylene 12, respectively.[39] The wavelength was swept by an amount $\Delta\lambda = 3.4$ nm, corresponding to a laser temperature change of 30.2°C. The wavelength of Laser B was intended to be kept constant at $\lambda_b = 1541.1670$ nm, corresponding to absorption peak P(14) of Acetylene 13.[84] However, in this experiment λ_b was stabilized to the minimum slope of the gas cell direct signal using an attocube ASC500 scan controller which provides a suitable feedback loop. As a result of stabilizing the laser wavelength off the absorption minimum, the wavelength was slightly shorter ($\lambda_b = 1541.164$ nm). In order to guarantee a stable wavelength stabilization, the direct signal was low-pass filtered in order to remove the high frequency modulation required for the phase determination. The wavelength stabilization of both lasers results in a beating wavelength of $\Lambda_s(\lambda_{a,s}|\lambda_b) = 101.936$ μm in the experiment,

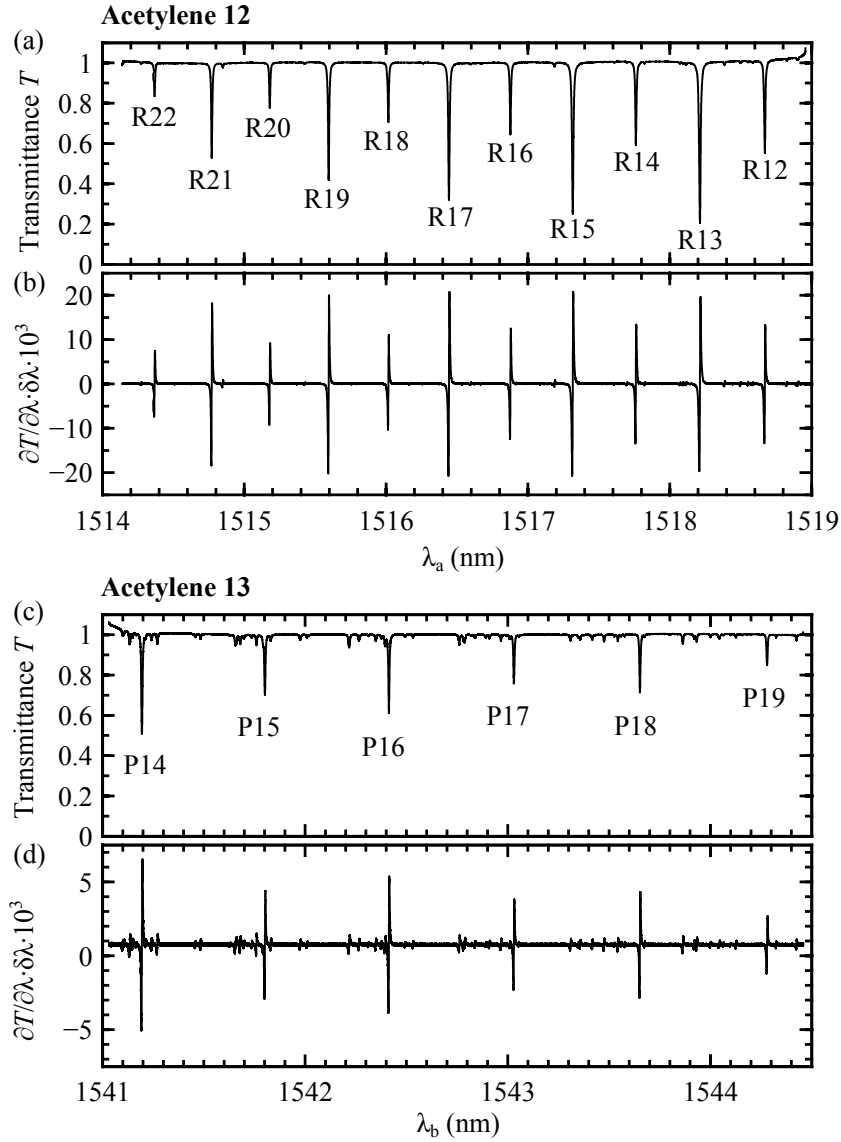


Figure 5.5: Spectroscopic data of Acetylene 12 and Acetylene 13 obtained by tuning the wavelength of the DFB laser. (a) and (c) show the gas cell normalized transmittance T of Acetylene 12 and 13, respectively. (b) and (d) show the wavelength demodulated signal of the gas cell transmittance of Acetylene 12 and 13, respectively.

generating a $\Lambda_s/2p = 25.484 \mu\text{m}$ long periodic beating interferometric pattern as a function of the target displacement for the folded cavity arrangement. The choice of convenient laser wavelengths is restricted by some conditions. The first condition is stated in equation 5.9 and sets a lower limit to the possible Λ_s . The second condition is stated in equation 5.12 and sets an upper limit to the possible Λ_s . The range of possible wavelengths λ_a and λ_b , which result in the beating wavelength Λ_s , is lim-

ited by the presence of absorption lines with sufficient depth and width to ensure a wavelength stability of about $\delta\lambda = 0.1$ pm.

5.3 Computation of absolute distance

The last section has demonstrated the full functionality of the measurement setup with a first data set taken from a displacing target in a vacuum. Both laser wavelengths were stabilized all the time. In this section, the robustness of the absolute distance measurement will be demonstrated at real conditions using a second data set taken from a similar cavity. Real conditions include cavity drifts which might affect the absolute distance measurement. For this reason, the absolute distance of a thermally drifting cavity in a vacuum is measured repeatedly (36 times) and the results are compared to each other by subtracting the measured displacement Δx which occurred since the start of the first measurement. The cavity displacement $\Delta x(t)$ is continuously tracked by Laser B. The computation of the absolute distance in the experiment includes several processes successively refining the result down to nanometer level.

In a preliminary process step, periodic phase nonlinearities are determined by linearly sweeping the wavelength of Laser A and B.

In the next process step, a coarse absolute distance x_{fti} is determined by sweeping the wavelength of Laser A. At the beginning of the measurement, λ_a is stabilized to $\lambda_{a,s}$ and is then repeatedly tuned between $\lambda_{a,e}$ and $\lambda_{a,s}$ by means of Control A, while λ_b remains stabilized in order to track target displacements. The time dependent phase change data $\Delta\Phi_a(t)$ and $\Delta\Phi_b(t)$ taken from the drifting cavity are shown in figure 5.6 (a), whereas the cavity displacement is shown in figure 5.6 (b). Since the laser heating process is much faster than the laser cooling, the transition from $\lambda_{a,e}$ to $\lambda_{a,s}$ leads to a temporary phase overshoot, which can be seen at the bottom of figure 5.6 (a) after each heating cycle. The setup includes a trigger for starting the frequency sweep operation of Laser A and for recording simultaneously Φ_a and Φ_b in processor P3. Using these phase change data, P3 calculates the phase differences $\Delta\Phi_a$ and $\Delta\Phi_b$ between start and end of the sweep. From the phase change $\Delta\Phi_a$ induced by the shift of the laser wavelength and the phase change $\Delta\Phi_b$ representing cavity drifts during the sweep, the absolute distance x_{fti} is derived using equation 5.5. The results x_{fti} for each of the sweeps 1 to 36 are shown in figure 5.7 (a). The graph shows

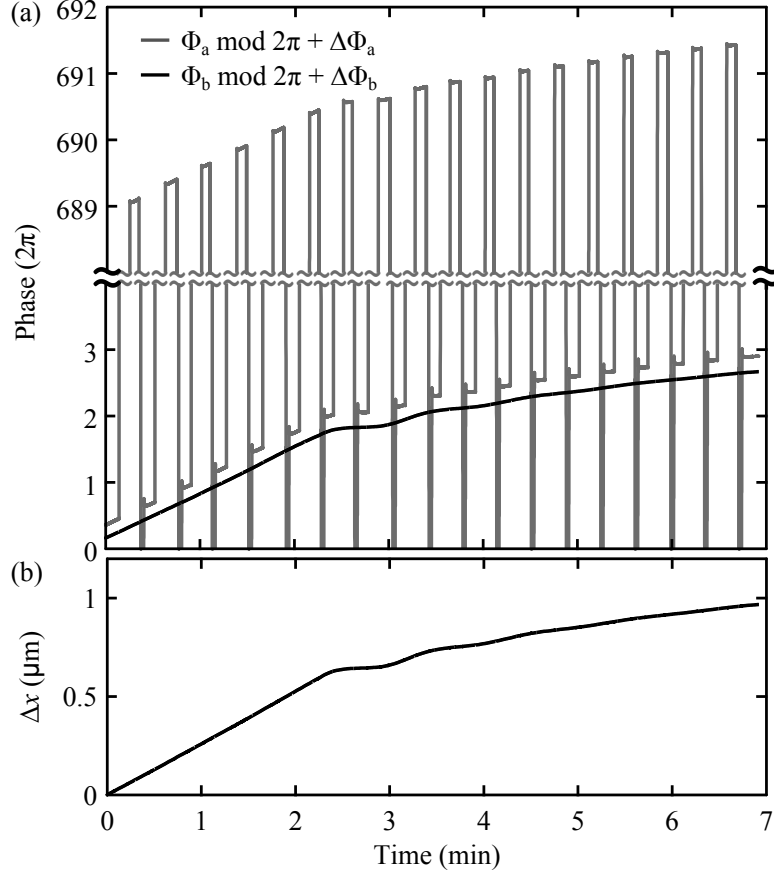


Figure 5.6: (a) Interference phase changes $\Delta\Phi_a(t)$ and $\Delta\Phi_b(t)$ measured with a drifting cavity in a vacuum. The wavelength of Laser A is periodically swept between Acetylene 12 lines R(13) and R(21). (b) Corresponding displacement Δx calculated from Φ_b .

that the uncertainty δx_{fti} of the absolute distance is in the order of 2 μm and fulfills therefore the inequality in equation 5.9, which requires $\delta x_{\text{fti}} < \Lambda_s/4 = 25.484 \mu\text{m}$. This means that the beating fringe number $N_{\Lambda,s}$ can be assigned unambiguously, in this case $N_{\Lambda,s} = 4511$. The following steps include only computations which are performed by processor P3. No more measurements are performed and both laser wavelengths are stabilized to a known wavelength in order to track displacements.

The result x_{fti} is used in the next step to calculate the beating wavelength fringe number $N_{\Lambda,s}$ based on the coarse distance x_{fti} and the fractional part of the start beating wavelength phase $\Phi_{\Lambda,s} = \Phi_{a,s} - \Phi_{b,s}$ using equation 5.6. Based on this fringe number, an intermediate coarse value of the absolute distance $x_{\Lambda,s}$ is calculated according to equation 5.10. The values of $x_{\Lambda,s}$ are all within an interval of $\lambda_{a,s}/4$, as shown in figure 5.7 (b), and therefore fulfill the condition stated in equation 5.12.

5.3. COMPUTATION OF ABSOLUTE DISTANCE

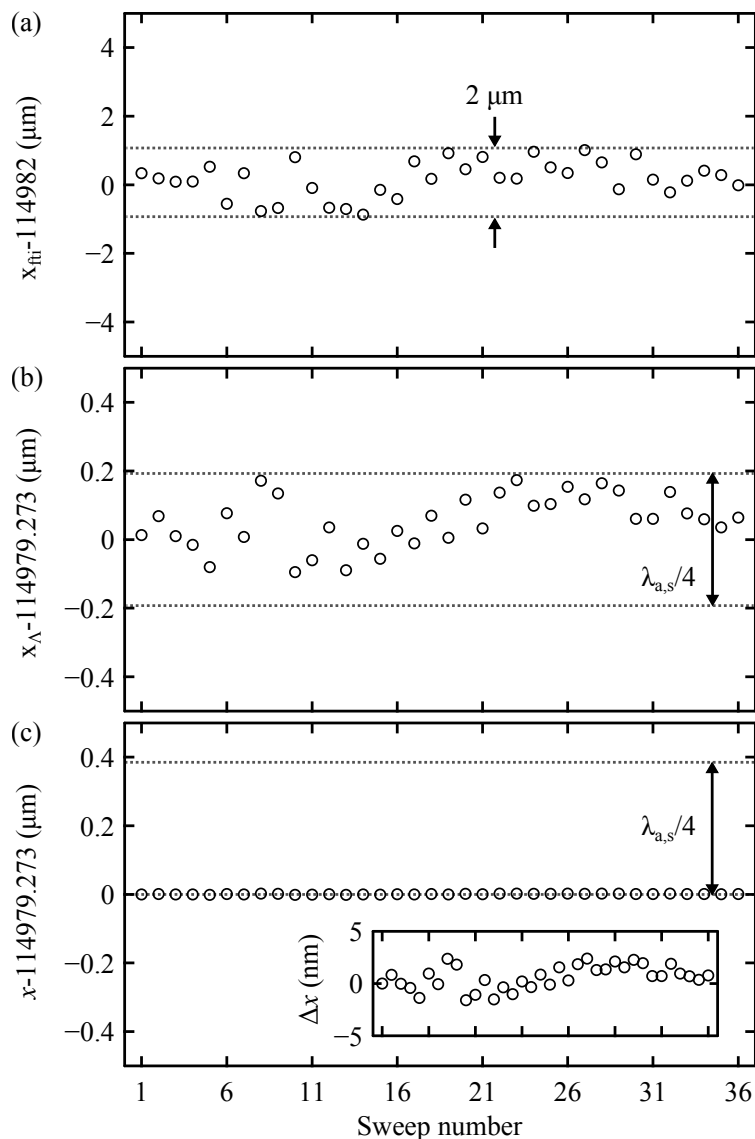


Figure 5.7: Absolute distances computation reproducibility derived from (a) frequency tuning, (b) beating wavelength phase $\Phi_{\Lambda,s}$ and (c) interference phase $\Phi_{a,s}$. The absolute distances are taken from a drifting cavity and are made comparable by subtracting the displacement Δx measured with Laser B.

In the last process, the final absolute distance x is determined with nanometer repeatability using equation 5.14, including $N_{\Lambda,s}$, the integer number of interference fringes $N_{a,s}^*$ within the fractional beating phase $\Phi_{\Lambda,s}$, expressed by the floor function, and the fractional part of the interference phase $\Phi_{a,s}$. The crucial point here is the assignment of the interference order $N_{a,s}^*$, which is necessary because of the residual nonlinearities of the synthetic wavelength phase, which are in the order of

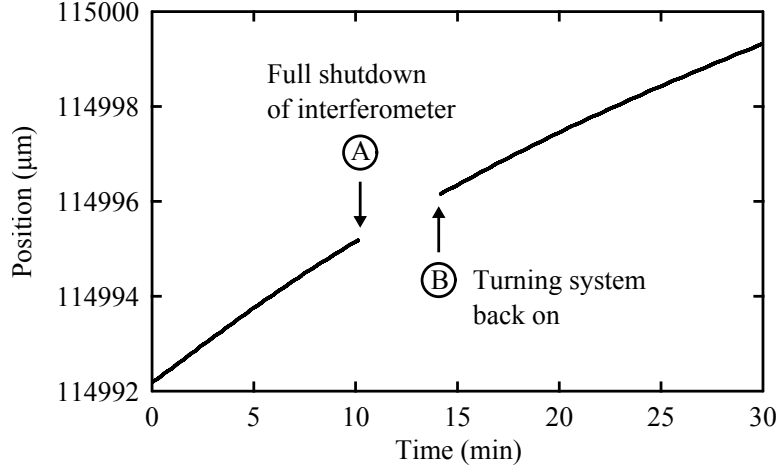


Figure 5.8: Interferometer shutdown during target displacement. The absolute position can be recovered with nanometer uncertainty.

$\delta\Phi_{\Lambda,s}/2\pi = 6 \cdot 10^{-3}$, as demonstrated in figure 5.4 (b). These nonlinearities would lead to an uncertainty of the absolute distance of $\delta x = \delta\Phi_{\Lambda,s}\Lambda_s/4p\pi = 0.2 \mu\text{m}$. The final absolute distance is $x = 114979.273 \pm 0.003 \mu\text{m}$ for all of the 36 data points, as shown in figure 5.7 (c). The inset shows a zoom around $x = 114979.273 \mu\text{m}$, revealing a maximum uncertainty of $\pm 3 \text{ nm}$. In the event that the uncertainty $\delta\Phi_{\Lambda,s}$ exceeds the condition stated in equation 5.12, the computed absolute distance would exhibit a quantized uncertainty jump of $\lambda_{a,s}/4$, which is also indicated in the graph.

The whole calculation process can now be repeated by using not the start values in equation 5.14, which refer to $\lambda_{a,s}$, but the end values which refer to $\lambda_{a,e}$ in order to improve statistics of the measurement. A further statistical improvement can be achieved by exchanging Laser A and B, i.e. sweeping the wavelength of Laser B while Laser A tracks displacement changes. As there is a tuning of both lasers at the start of the absolute distance measurement in order to determine nonlinearities, both tuning data could be used for the position calculation by default.

The measurements have demonstrated the robustness of this technique by repeatedly measuring the absolute distance. Now the reconstruction of the absolute distance after performing a complete shutdown of the interferometer will be demonstrated. Therefore, the position of a constantly drifting vacuum cavity is tracked, similar to the one presented before. This time, however, the interferometer is completely shut down during the measurement, while the cavity keeps on drifting. This is indicated by point A in the experimental data which are shown in figure 5.8. After 4 minutes,

the system is turned back on at point B and the absolute position could be recovered successfully. This result demonstrates that the position of a displacing stage can be known at any time with nanometer precision. Interruptions of the interferometer would cause a short waiting time of only a few seconds, after that time the absolute position is known again. This can help avoiding cumbersome alignment processes and enables multi-step processes with nanometer precision overlay.

5.4 Summary

In this chapter, a new method for measuring absolute distances in the sub-meter range using a fiber-optic interferometer has been established. In particular, the ambiguity of a single wavelength interferometer was eliminated by combining frequency tuning interferometry with dual wavelength interferometry. In this way, it has been shown that dual wavelength interferometry is well suited to increase the ambiguity range of a single wavelength interferometer. For unambiguous absolute distance measurements, however, the capabilities of the dual wavelength interferometer have been extended by tuning the emission frequency of one laser. Frequency tuning interferometry is well suited for measuring absolute distances at long range, but the accuracy is limited by different error sources, of which cavity drifts during the wavelength sweep due to the slow tuning speed predominate. By means of tracking cavity drifts during the wavelength sweep, the uncertainty of the frequency tuning could be kept below the unambiguity range of the dual wavelength interferometer. This enabled the elimination of the ambiguity of the interference beating pattern of the dual wavelength interferometer, thus allowing to determine absolute distances in the sub-meter range with a repeatability of ± 3 nm. It was further demonstrated that the wavelength modulation of both lasers with different frequencies enables easy separation of both interference phases and this without the use of optical filters, beam splitters or additional detectors, thus reducing the complexity of the system and making it robust against external influences. The computation of the absolute distance is performed without the use of any reference length or length standard which are sometimes required in other absolute distance interferometers. The operation of the system was demonstrated for one interferometric axis, but in principle, is also well suited for multi-channel applications.

The simple, robust and affordable technique will make absolute distance measure-

ments available for a large field of applications, and in this way, will enable positioning of objects with nanometer repeatability even in the harshest environments. So far, all tests were done in a vacuum, the air refractive index was not yet considered experimentally. Future work must take into account ambient conditions, as most of the measurements are performed in air. The coarse absolute distance measurement by wavelength tuning has already been implemented in the IDS3010 for automatic adjustment of the wavelength modulation amplitude and the demodulator phase and for automatic initialization of the air compensation unit. This innovation has already significantly simplified the operation of the interferometer.

6 Applications

The small fiber coupled sensor head and its robust all optical design makes the interferometer suitable for a wide range of applications including the most demanding environmental conditions. For example, it is used at synchrotrons for shaping of the particle beam and at their respective beamlines, e.g., for alignment of a test specimen with respect to the particle beam. At synchrotrons, the sensor heads are often exposed to ionizing radiation and ultra-high vacuum. The good adaptability of the sensor head to different surfaces makes the interferometer interesting for applications in the semiconductor industry, where displacement measurements directly on silicon wafers is required. In coordinate-measuring machines, the interferometer enables measurements on the sample level and provides additional information about the target yaw and pitch movement. Due to the high measurement bandwidth, the interferometer can also be used for contactless eccentricity measurements on all kind of bearings, e.g. in order to determine the runout of a hard drive.

In this chapter, two applications are presented by way of example. The first section demonstrates the operation of the interferometer at cryogenic temperatures. In the second section, a special setup for the measurement of the expansion of a piezoceramic is presented.

6.1 Low temperature applications

Some applications require keeping track of the target movement when the ambient temperature is changed by several hundreds Kelvin. This is probably the most critical process since deformations of the cavity might lead to a loss of position information. In order to demonstrate the immunity of the interferometer system against these temperature gradients, a titanium cavity was repeatedly cooled down from room temperature (297 K) to 79 K using liquid nitrogen. Figure 6.1 (a) shows the displacement measured with three different cavities and (b) the corresponding temperature.

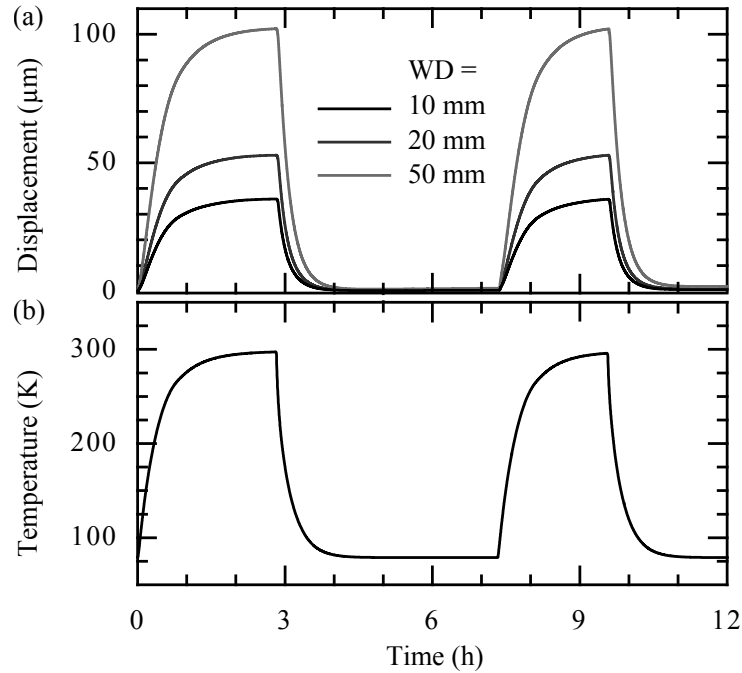


Figure 6.1: Demonstration of the robustness to large temperature gradients. (a) Cavity expansion and contraction as a function of time measured when heating and cooling a titanium cavity operated in double pass mode. (b) Corresponding temperature.

The cavity mirrors have a working distance of 10 mm, 20 mm and 50 mm. The measurement shows that the system is well suited to meet the requirement in low-temperature applications.

Microscopy applications at low temperatures rely on piezoelectric actuators which scan the sample under test. This requires actuators moving very linear and without any backlash, which, in practice, do not exist. In a further test, by way of example, the backlash of a piezoelectric positioner actuating at liquid helium temperature was characterized. For this purpose, a prototype positioner that moves in the Z direction was placed in a vacuum tube and equipped with three mirrors as depicted in figure 6.2 (a). Three independent interferometer axes are used to simultaneously track movements in the X, Y and Z direction. Because of the constrained space within the tube, two passive reflectors are necessary for tracking displacements in the X and Y direction. Plotting all three axes against each other reveals a hysteresis of the movement encountered when reversing the direction of motion. This is shown in figure 6.2 (b), where the gray curves show projections to the coordinate planes. The hysteresis shows up in a lateral backlash of about 1 μm . The measurement have been

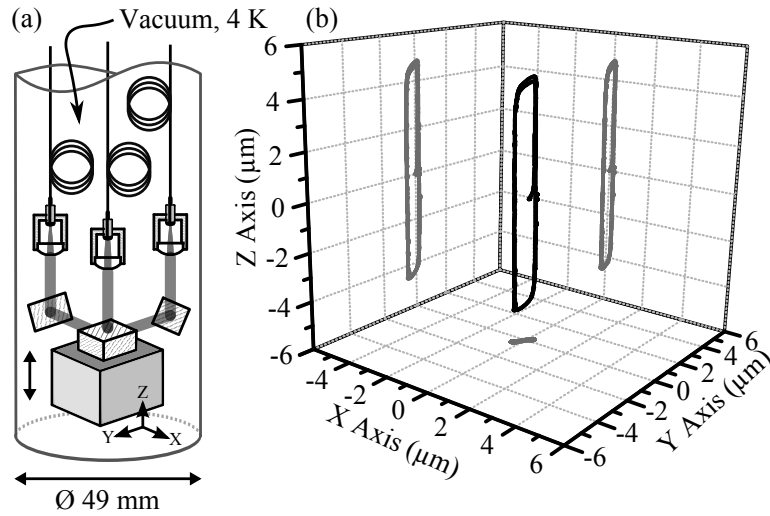


Figure 6.2: Measurement of the backlash of a positioner moving in the Z direction. The setup is placed in a vacuum tube and cooled down to liquid helium temperature (4 K).

performed by Dr. Claudio Dal Savio and Dr. Francesca Paola Quacquarelli in the attocube labs.

Such an interferometric system can be used in low-temperature microscopes to

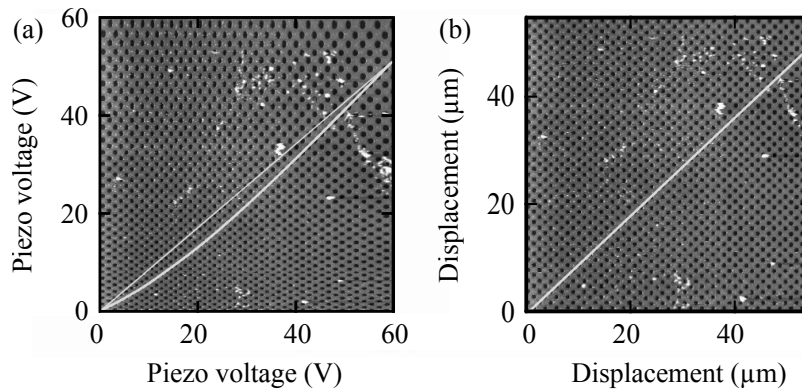


Figure 6.3: Image correction by interferometric piezo linearization. (a) AFM topography as a function of the voltage on the scanner piezo. (b) AFM topography as a function of the measured displacement of the scanner.

actively compensate for any unwanted mechanical nonlinearities during surface sampling by means of a feedback control. An example for this is the sampling of a probe by means of a piezoelectric scanner in atomic force microscopy (AFM). Figure 6.3 exemplary shows the linearization of the topography of a grating structure by post-processing of the data. As the piezo doesn't expand linear with the applied voltage,

plotting the height data against the applied piezo voltage leads to nonlinearities. This can be circumvented using the interferometric position information from both scan directions instead of the applied voltage. An adequate feedback control would make the post processing superfluous.

6.2 Differential interferometer

A different application is the measurement of the piezoelectric expansion of a piezoceramic with sub-nanometer resolution. When applying a voltage, the piezoceramic material expands and usually also bends. In order to eliminate the effect of bending, the expansion is measured in a differential configuration of two vertically aligned interferometer axes. The main difference between the measurement system that was presented so far and the system that is presented in this section is that this time not the laser wavelength is modulated, but the target position. The target position modulation is based on the displacement provided by piezoelectric actuators. The difficulty herein is to measure directly on the piezo surface in order not to affect the result. The setup is configured to operate the measuring system in two different modes providing different measurement precision and range. The first measurement method is very similar to the DC/ Ω quadrature detection scheme based on the direct and demodulated signals, with the difference that this time the position of the target rather than the wavelength is modulated. The second method theoretically provides a higher accuracy and is based on the demodulation of the signal around the maximum slope of the interference signal. Unfortunately, no measurement data can be shown for this method, therefore this section is limited to the description of the basic concept.

6.2.1 Vibrometer setup

The differential vibrometer setup is schematically shown in figure 6.4. Figure 6.5 shows the practical implementation. It allows measuring the displacement of the sample piezo from both the upper and the lower side. The sample is therefore placed on a middle table with a through-hole for the lower laser beam. The measurement is made directly on the sample surface which has a certain roughness and reflectivity. This is enabled by the use of two focusing sensor heads providing laser beams that

6.2. DIFFERENTIAL INTERFEROMETER

are focused to the respective sample surface. A specialty of the setup is that the upper sensor head, the sample table and the lower sensor head can be displaced in Z direction by means of the piezoelectric actuators Piezo U, Piezo M and Piezo L. The fiber circuit provides two outputs for the simultaneous measurement of the

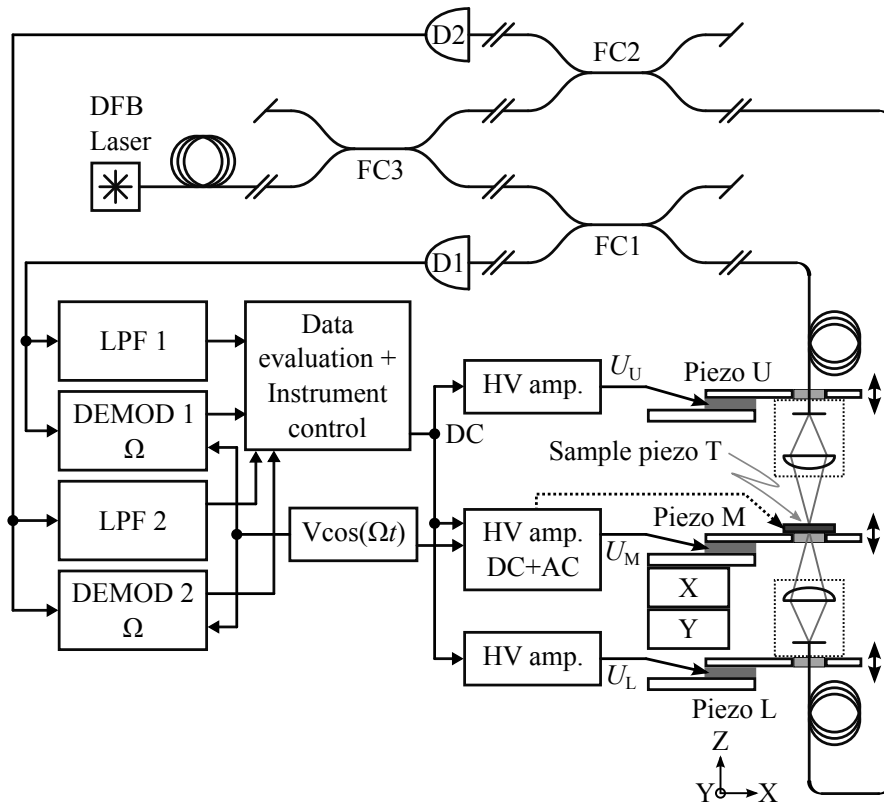


Figure 6.4: Differential vibrometer setup for the measurement of the piezoelectric expansion of different sample piezoceramics. The displacement is measured directly on the sample surface and from both sides of the sample. The measurement results of both channels are subtracted from each other in order to cancel the effect of sample bending. Due to the high surface roughness of the samples, two focusing sensor heads were used. As the laser wavelength is fixed in this setup, both sensor heads are mounted to piezoelectric actuators which are able to displace the sensor heads in Z direction. The electronic setup includes two demodulators DEMOD 1 and 2, two low-pass filters LPF 1 and 2, one oscillator providing a voltage $U \cos \Omega t$ and three high voltage amplifiers HV amp. The optical setup includes three fiber coupler FC1, FC2 and FC23 and two detectors D1 and D2.

displacement of two interferometric axes. The light from these outputs is routed to the sensor heads and the reflected interference signal is detected at the detectors D1 and D2. From there, the signal is input into a low-pass filter and a demodulator demodulating at the frequency Ω . A processor in the data evaluation unit then

converts the measurement signals into displacements. By subtracting the measured displacement of the upper sensor head from the displacement of the lower sensor head, the effect of sample bending is eliminated, thus revealing the actual piezo expansion. The data evaluation and instrument control unit further provides outputs for the control of the piezo bias voltage (DC) and for the high frequency modulation (AC) which provides a voltage $V \cos(\Omega t)$. In particular, it may provide a voltage ramp in order to scan over a desired voltage interval. The setup moreover includes high voltage amplifiers in order to cover voltages up to about 100 V, since usual control circuits only provide voltages with single digit amplitude. In the next two sections,

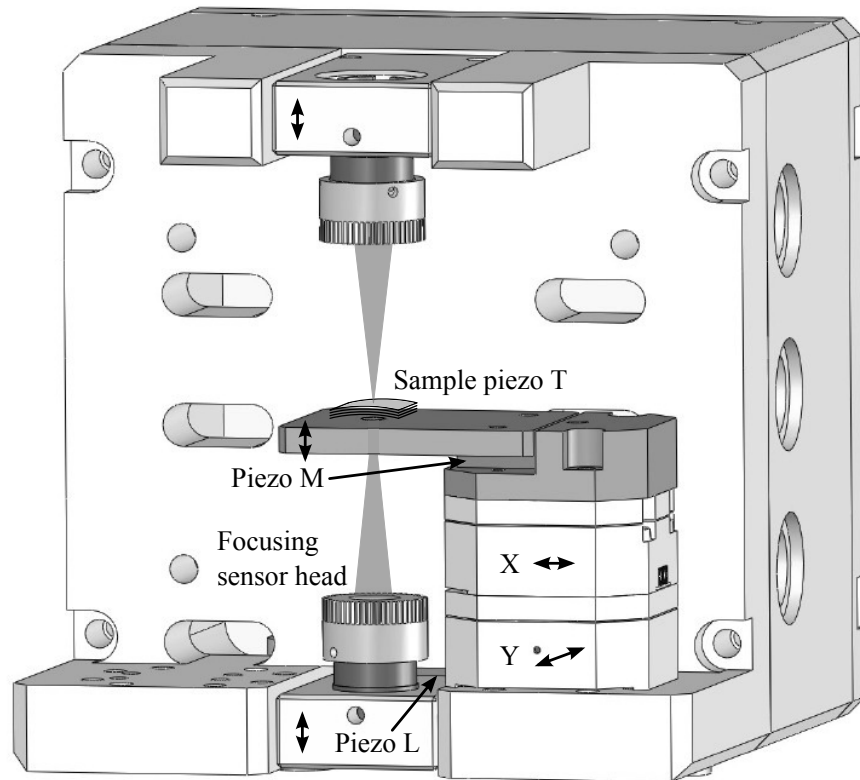


Figure 6.5: Technical drawing of the differential vibrometer setup. The two sensor heads are configured to focus the laser beam on the sample piezo surface.

the two different measurement methods are described.

6.2.2 Long range measurements

The first measurement method is well in accordance with the quadrature detection scheme which uses the direct and demodulated signal. In contrast to the wavelength

modulation technique used in the interferometer presented in the rest of this work, the interference intensity modulation originates this time from a modulation of the mirror distance δx , according to the first term in equation 2.27. The modulation of the mirror position, by the way, has the advantage that the modulation depth no longer depends on the cavity length, meaning that also ultra short short cavities are feasible. The modulation depth is in this case given by

$$\delta\Phi = \frac{4p\pi}{\lambda}\delta x \quad (6.1)$$

and is no longer a function of the fiber to mirror distance x .

Before each measurement, a calibration of both interferometric axes has to be performed. This is necessary in order to normalize the measurement data which will be taken from the test piezo. Therefore, both the AC and DC voltage are applied to the middle piezo and the DC bias voltage is scanned over a range which is large enough so that the shift of the interference phase angle is at least 2π . The data evaluation unit then determines both minimum and maximum of the direct and demodulated voltage provided by the filtered interference signal and the demodulator, respectively.

For the sample piezo measurement, the AC voltage is applied to the middle piezo whereas the DC voltage is applied to the test piezo. The DC voltage is then scanned over the desired voltage range and the direct and demodulated detector voltage is recorded from both interferometer channels. The data evaluation unit normalizes the test data by using the offset and scaling values from the calibration. Then, the phase angle change of each measurement value is calculated and summed up. A look-up table containing the phase deviations resulting from nonlinearities can be applied to the phase data in order to increase the measurement accuracy. The final displacement is calculated using equation 2.44.

The resulting hysteresis loop for an arbitrary piezoceramic stack is shown in figure 6.6. The voltage applied to the piezo was scanned between 0 and 45 V, resulting in an expansion of about 100 nm.

6.2.3 Short range measurements

The high position sensitivity around the maximum slope of the interference signal can be exploited in order to achieve a higher accuracy compared to the long range measurement method. When applying the AC voltage to the test piezo, the amplitude of the demodulated signal depends on the transfer function between input voltage

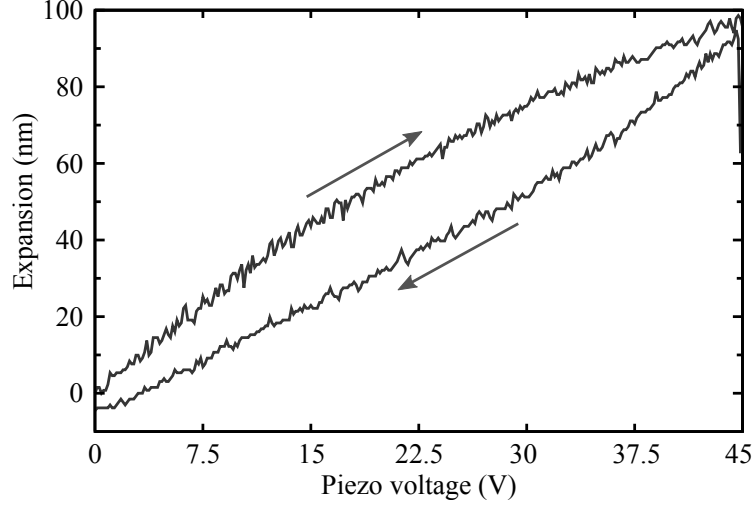


Figure 6.6: Piezo hysteresis of a piezo stack. The displacement was measured from two sides in a differential configuration allowing to eliminate the effect of bending.

and expansion and is a measure for the slope of the expansion-voltage characteristic. The recovery of the total piezo displacement is therefore based on locally deriving the slope of the expansion-voltage characteristics and subsequent integration of the result. Modulation of the test piezo around a certain bias voltage U_T and subsequent demodulation of the interference signal yields the derivative ds/dU of the expansion s of the test sample with respect to the applied DC voltage U_T . The total displacement can be calculated by integrating over the derivative ds/dU_T . The derivative ds/dU_T is measured by placing it between two vertical arranged interferometers and calculating the difference between the derivative dx_U/dU_T and dx_L/dU_T of the upper and lower interferometer, respectively. The differential configuration is again used in order to compensate the effect of sample bending.

In this measurement method, the differential expansion of the test piezo is measured as a function of the DC bias voltage applied to the test piezo. Therefore, the test piezo is modulated with the frequency $\delta U_T \sin(\Omega t)$ around the bias voltage U_T . If the displacement modulation amplitudes δx_U and δx_L are small with respect to $\lambda/4$ ($\delta x \ll \lambda/4$), then there is a linear correlation between the interference intensity modulation δI_U and δx_U and between δI_L and δx_L . The signal intensity of a Michelson interferometer (two beam interference) is given by

$$I(x) = \frac{I_0}{2} + C \frac{I_0}{2} \cos \{2kx\}. \quad (6.2)$$

The derivative of this function is

$$\frac{\partial I}{\partial x} = -CI_0k \sin(2kx), \quad (6.3)$$

which becomes

$$(\partial I/\partial x)_{\max} = \pm CI_0k \quad (6.4)$$

at the maximum slopes. This yields the linear correlation between the displacement modulation amplitudes δx and the modulated intensity δI according to

$$\delta x = \frac{\delta I}{CI_0k}. \quad (6.5)$$

This relation is valid for a very small voltage range of the test piezo, where the intensity is proportional to the displacement. Since it would be very troublesome to readjust both sensor heads to the maximum slope after each recorded value of δI , the following assumption can be made in order to extend the linearity range of equation 6.5. For higher voltages, $\sin(2kx)$ is approximated by using the direct signal I as follows:

$$\begin{aligned} I &= I_0 \frac{1 + C \cos(2kx)}{2} = I_0 \left(\frac{1 + C \sqrt{1 - \sin^2(2kx)}}{2} \right) \\ \Rightarrow \sin(2kx) &= \sqrt{1 - \left(\frac{2I - I_0}{CI_0} \right)^2} \end{aligned} \quad (6.6)$$

This means that the direct detector signal can provide information about the derivative, which can be used to linearize the demodulated signal around the point of maximum slope. In this way, the relation of equation 6.4 can be rewritten in terms of the direct detector signal I .

$$\delta x = -\frac{\delta I}{CI_0k \sin(2kx)} = -\frac{\delta I}{CI_0k \sqrt{1 - \left(\frac{2I - I_0}{CI_0} \right)^2}} \quad (6.7)$$

To obtain the final derivative dx/dU , δx has to be divided by the oscillation voltage δU_T . In this step, it is important to make sure to divide equal magnitudes, i.e. either the RMS amplitudes δx_{rms} and δU_{rms} or the peak-to-peak amplitudes δx_{pp} and δU_{pp} , which are related by $\delta x_{\text{pp}} = \sqrt{8} \cdot \delta x_{\text{rms}}$.

Before starting the actual measurement, the direct detector signal has to be normalized. This requires the determination of C and I_0 in both channels, which is achieved

by applying the AC modulation voltage and DC bias voltage to the middle piezo and scanning the DC voltage over a range large enough so that the interference signal goes at least through one full interference fringe. The measurement data are then used to determine I_{\min} and I_{\max} , from which I_0 and C are deduced according to equation 2.13 and 2.14. Furthermore, the position of both sensor heads must be adjusted in such a way that they operate at the same edge of the interference signal, i.e. either both operate at the rising edge or on the falling edge. If this step is not performed, both channels might show a different sign, thus providing a wrong measurement result. In the setup, the height of both sensor heads is adjusted by means of the upper and lower piezo, respectively. Both sensor heads are brought close to the maximum slope of the interference signal. When changing now the height of the middle piezo, the interference intensity in both channels must either increase or decrease. If this is not the case, one of both sensor heads must be displaced by $\lambda/4$.

For the actual test piezo measurement, the AC modulation voltage and DC voltage are applied to the test piezo and the DC voltage is scanned over the desired voltage range. The displacement should thereby not exceed about $\pm\lambda/16$ around the maximum slope.

Improvements could be achieved by adding a feedback loop that controls the position of both sensor heads so that they are continuously operating at the point of maximum slope. The short range post-processing program enables to measure the derivative of displacements of a piezo with respect to the applied voltage with a sensitivity of about 200 pm within a range of about 100 nm. Larger displacements can not be measured.

7 Conclusion and Outlook

In this work, a novel fiber-based low-finesse Fabry-Pérot interferometer system for the measurement of relative and absolute positions has been developed and investigated on its characteristics. It breaks through the limitations given by current laser interferometers in terms of compactness, robustness, usability, industry scalability and costs. The system consists of an all optical sensor head and a remote processing unit, including fiber optical circuit, position processing electronic and wavelength stabilization electronic.

The theoretical considerations at the beginning of this work provide the fundamentals of the interferometer, which help understanding the fundamental limitations of the interferometer system. A relativistic treatment of the interference phase demonstrated that the phase shift measured during target displacement is solely attributed to the Doppler effect. An important conclusion that can be drawn is that the time t must be separated from the place x when using the plane wave equation in order to describe the light reflected off a moving object. This means that expressions of the form $x = x(t)$ are invalid, i.e. the place mustn't be a function of time. This knowledge will avoid future misinterpretations with respect to calculations of the impact of moving objects on the interferometer position reading. Apart from that, a special quadrature detection scheme based on the wavelength modulation of light was introduced. Through demodulation of the wavelength modulated interference signal, a 90° phase shifted signal is created. Both the phase shifted demodulated and the low-pass filtered signal form a Lissajous figure whose angle represents the interference phase. Compared to other interferometers, this technique allows generating a quadrature signal without the use of optical components such as retardation plates. However, it was shown that this advantage is at the expense of the working range, which is limited to small and large distances, according to a range between few millimeters to several meters. It was further shown that the reflected signal of the fiber coupled Fabry-Pérot cavity depends on the target reflectivity and on the coupling efficiency

of the reflected light. In order to predict particular features such as the signal contrast or nonlinearities, a computational model based on an optical design software was developed. This model allows characterizing new sensor head configurations in advance, without the need for prototyping and extensive testing.

During this work, several prototypes of the interferometer system have successfully been realized. Different to most common laser interferometers, the system in this work uses a semiconductor diode laser operating in the telecom wavelength range. Optical components in this wavelength range are cost-effective and therefore well suited for industry applications, but the low frequency stability of the laser requires that its wavelength is actively locked to a reference molecular absorption gas cell. What in the beginning was considered as a disadvantage, soon emerged as a great opportunity for the implementation of a signal normalization procedure and of an absolute distance measurement, constituting a great innovation in the field of displacement interferometry. By actively locking the laser wavelength to a known reference, the laser stability becomes comparable with that of gas lasers used in commercial interferometers. The high bandwidth of the interferometer makes it well suited for high speed and vibrometry applications. The interferometer includes a real-time interface capable of running different protocols which were described in detail. This should help future users choosing the right protocol. As most interferometers are operated in ambient conditions, an algorithm based on the environmental data provided by a weather station was developed and its correct operation was verified experimentally in a closed chamber and by comparative measurements performed at the PTB.

The compactness and robustness of the interferometer system result mainly from the simple structure of the sensor head, which is remotely connected with the interferometer by means of an optical fiber. The sensor head includes nothing more than a titanium housing and a lens for beam shaping. Since the sensor head forms a Fabry-Pérot cavity with the target reflector, no reference arm, and as a consequence no beam splitter or wave plate, is required. This fact allows the miniaturization of the sensor head and its use in extreme environments. The sensor head has proven to be adaptable to a wide range of applications. Depending on the application, the light emitted by the fiber can be either collimated or focused. The focused beam is mainly used for measurements on small size or rough targets or on targets with a reflectivity lying between that of glass or aluminum. The collimated beam is used for measurements over large ranges and can be used with a retro reflector or a plane

glass target. It was shown that the collimated sensor head forms a double pass cavity when used in combination with a high reflective plane target and that this configuration has a large angular alignment tolerance. Simulations conducted in this work have shown that the angular alignment tolerance of the double pass sensor head is not constant as a function of the working distance, it rather decreases with increasing working distance. As a consequence, the permitted measurement range of this special configuration was limited to 100 mm.

A general limitation of displacement interferometry is the missing possibility for referencing to an absolute position. This problem was solved using a novel dual laser interferometer which eliminates the ambiguity of a single wavelength interferometer by combining frequency tuning interferometry with dual wavelength interferometry. This new approach builds on the fiber-optic displacement measuring system and is therefore compatible with the sensor head technology described in the last paragraph. The interferometric determination of the absolute position includes three steps: Performing a coarse absolute distance measurement by sweeping the wavelength of one laser and tracking cavity drifts with the other laser, assigning a fringe number to the beating wavelength created by the two wavelength stabilized lasers, and assigning a fringe number to one of the two laser wavelengths. In this way, an absolute distance in the sub-meter range can be measured with a repeatability of ± 3 nm, provided that the cavity is in a vacuum. The difference to the known wavelength tuning interferometry is the capability to track position changes during the wavelength sweep. Since cavity drifts contribute with an leverage factor of about 10^3 , the robustness and accuracy of this wavelength tuning measurement was significantly increased, thus making this process suitable for integration in an industrial environment. Another difference to known multiple wavelength interferometers is the elimination of the ambiguity by means of wavelength tuning interferometry. Information about the absolute position is not only useful for referencing of an moving object. It is also required for the refractive index compensation or can also be used for open loop control of internal parameters, such as the wavelength modulation amplitude. A cut-down version of this new technology, namely an absolute distance measurement by wavelength tuning, has already been successfully implemented in the IDS3010 where it is used for the ECU and for the control of internal parameters. This has significantly improved the user-friendliness and the robustness of the measurement.

In future, the key challenge of this technique and of interferometry in general will

be the direct measurement and compensation of the refractive index the light experiences on its way through the cavity. This work already includes an exemplary calculation for the use of a separate refractometer cavity. However, local air turbulence will introduce errors in the compensation process, making a direct measurement along the beam path necessary. Another future task will be the verification of the absolute distance measurement technique at ambient conditions. So far, all measurements were solely performed in a vacuum. Another topic that was not yet considered in this work is the investigation of parasitic cavities and the coupler crosstalk in the fiber circuit. The results might be helpful for the reduction of the position noise level. In the foreseeable future, one important topic will be the correction of periodic nonlinearities arising, for example, from multiple reflections in the cavity, enabling a measurement accuracy in the sub-nanometer range. This requires filling a look-up table located in the FPGA, containing information about the phase angles and their associated phase correction term. Part of the ongoing work targets the extension of the working range up to 30 m. The main problem that has to be solved is the limited speed which is associated with the filter settings at far positions. Since the phase noise scales linearly with the distance, the filter must have steeper edges the longer the cavity is. This, however, reduces the maximum speed the interferometer can track.

8 List of publications

This chapter lists all publications that originated from the work related to the topic of this thesis.

Contributions to journals

- Klaus Thurner, Pierre-François Braun, and Khaled Karrai, “Fabry-Pérot interferometry for long range displacement sensing,” *Review of Scientific Instruments*, 84, 095005 (2013), DOI: <http://dx.doi.org/10.1063/1.4821623>
- Klaus Thurner, Pierre-François Braun, and Khaled Karrai, “Absolute distance sensing by two laser optical interferometry,” *Review of Scientific Instruments*, 84, 115002 (2013), DOI: <http://dx.doi.org/10.1063/1.4831800>
- Klaus Thurner, Francesca Paola Quacquarelli, Pierre-François Braun, Claudio Dal Savio and Khaled Karrai, “Fiber-based distance sensing interferometry,” *Applied Optics*, Vol. 54, Issue 10, pp. 3051-3063 (2015), DOI: <http://dx.doi.org/10.1364/AO.54.003051>

Patents

- Klaus Thurner, Pierre-François Braun, and Khaled Karrai. EU Patent Application No. EP2806246 (A1), Application number: EP20130169159 20130524, published 2014/11/26, filed 2013/05/24. Page bookmark: http://worldwide.espacenet.com/publicationDetails/biblio?FT=D&date=20141126&DB=EP0DOC&locale=en_EP&CC=EP&NR=2806246A1&KC=A1&ND=4

Conference posters with proceedings

- Klaus Thurner, Pierre-François Braun, and Khaled Karrai, “Distance metrology using a low-finesse fiber-optic Fabry-Pérot interferometer,” Nanoscale 2013 Conference (Paris, France, April 2013)

- Klaus Thurner, Pierre-François Braun, and Khaled Karrai, “Distance metrology using an original fiber-optic interferometer,” Proceedings of the 13th Euspen International Conference (Berlin, Germany, May 2013)
- Klaus Thurner, Pierre-François Braun, and Khaled Karrai, “Absolute distance sensing by dual laser interferometry,” Proceedings of the 14th Euspen International Conference (Dubrovnik, Croatia, June 2014)

Conference talks

- Klaus Thurner, “3-axis fiber-based interferometry replacing glass scales,” Precision Fair 2014 (Veldhoven, Netherlands, November 2014)

Bibliography

- [1] J. Shieh, J. Huber, N. Fleck, and M. Ashby, “The selection of sensors,” *Prog. Mater. Sci.*, vol. 46, pp. 461 – 504, 2001.
- [2] A. J. Fleming, “A review of nanometer resolution position sensors: Operation and performance,” *Sensors and Actuators A: Physical*, vol. 190, no. 0, pp. 106 – 126, 2013.
- [3] K. Karrai, “Device for position detection,” 8 Apr. 2009. European Patent Application EP2045572 (A1).
- [4] K. Karrai and P.-F. Braun, “Positioning device with confocal fabry-perot interferometer,” 7 Sept. 2011. European Patent EP2363685 (B1).
- [5] A. Pogačnik, T. Požar, M. Kalin, and J. Možina, “A homodyne quadrature laser interferometer for micro-asperity deformation analysis,” *Sensors*, vol. 13, no. 1, p. 703, 2013.
- [6] J. R. Lawall, “Fabry-perot metrology for displacements up to 50 mm,” *J. Opt. Soc. Am. A*, vol. 22, pp. 2786–2798, Dec 2005.
- [7] Y.-C. Wang, L.-H. Shyu, and C.-P. Chang, “The comparison of environmental effects on michelson and fabry-perot interferometers utilized for the displacement measurement,” *Sensors*, vol. 10, no. 4, pp. 2577–2586, 2010.
- [8] International Bureau of Weights and Measures (BIPM), International vocabulary of metrology: Basic and general concepts and associated terms (VIM), 3rd edition, 2012.
- [9] K. Thurner, F. P. Quacquarelli, P.-F. Braun, C. D. Savio, and K. Karrai, “Fiber-based distance sensing interferometry,” *Appl. Opt.*, vol. 54, pp. 3051–3063, Apr 2015.

BIBLIOGRAPHY

- [10] K. Thurner, P.-F. Braun, and K. Karrai, “Fabry-pérot interferometry for long range displacement sensing,” *Rev. Sci. Instrum.*, vol. 84, no. 9, pp. –, 2013.
- [11] K. Thurner, P.-F. Braun, and K. Karrai, “Absolute distance sensing by two laser optical interferometry,” *Rev. Sci. Instrum.*, vol. 84, no. 11, pp. –, 2013.
- [12] K. Thurner, P.-F. Braun, and K. Karrai, “Dual laser interferometer,” Nov. 26 2014. European Patent Application EP2806246 (A1).
- [13] J. D. Jackson, *Classical Electrodynamics Third Edition*. Wiley, third ed., Aug. 1998.
- [14] K. F. Herzfeld, “On the equations of laplace and maxwell,” *Phys. Rev.*, vol. 39, pp. 497–503, Feb 1932.
- [15] W. F. G. Swann, “Relativity and electrodynamics,” *Rev. Mod. Phys.*, vol. 2, pp. 243–304, Jul 1930.
- [16] W. Nolting, *Grundkurs Theoretische Physik 3*. Grundkurs Theoretische Physik, Springer, 2011.
- [17] M. Bass, *Handbook of Optics, Vol. II: Devices, Measurements, and Properties, Second Edition*, vol. 2 of *Handbook of Optics*. New York, NY, USA: McGraw-Hill, Inc., 2 ed., 1995.
- [18] R. H. Belansky and K. H. Wanser, “Laser doppler velocimetry using a bulk optic michelson interferometer: A student laboratory experiment,” *Am. J. Phys.*, vol. 61, no. 11, pp. 1014–1019, 1993.
- [19] W. B. Allan, *Fibre optics, theory and practice, by W. B. Allan*. Plenum Press London, New York, 1973.
- [20] A. Snyder and J. Love, *Optical Waveguide Theory*. Science paperbacks, Springer, 1983.
- [21] D. Rugar, H. J. Mamin, and P. Guethner, “Improved fiber-optic interferometer for atomic force microscopy,” *Appl. Phys. Lett.*, vol. 55, no. 25, pp. 2588–2590, 1989.

BIBLIOGRAPHY

- [22] D. T. Smith, J. R. Pratt, and L. P. Howard, “A fiber-optic interferometer with subpicometer resolution for dc and low-frequency displacement measurement,” *Rev. Sci. Instrum.*, vol. 80, no. 3, p. 035105, 2009.
- [23] L. Meade, *Lock-in Amplifiers: Principles and Applications*. IEE electrical measurement series, P. Peregrinus, 1983.
- [24] P. K. Dixon and L. Wu, “Broadband digital lock-in amplifier techniques,” *Rev. Sci. Instrum.*, vol. 60, no. 10, pp. 3329–3336, 1989.
- [25] M. Abramowitz and I. A. Stegun, *Handbook of Mathematical Functions with Formulas, Graphs, and Mathematical Tables*. New York: Dover Publications, 1964.
- [26] A. Dandridge, A. Tveten, and T. Giallorenzi, “Homodyne demodulation scheme for fiber optic sensors using phase generated carrier,” *IEEE J. Quantum. Electron.*, vol. 18, no. 10, pp. 1647–1653, 1982.
- [27] M. A. Kramer, R. W. Boyd, L. W. Hillman, and C. R. Stroud, “Propagation of modulated optical fields through saturable-absorbing media: a general theory of modulation spectroscopy,” *J. Opt. Soc. Am. B*, vol. 2, pp. 1444–1455, Sep 1985.
- [28] A. Perot and C. Fabry, “On the application of interference phenomena to the solution of various problems of spectroscopy and metrology,” *Astrophys. J.*, vol. 9, p. 87, Feb. 1899.
- [29] J. F. Mulligan, “Who were Fabry and Pérot?,” *Am. J. Phys.*, vol. 66, pp. 797–802, Sept. 1998.
- [30] M. Born and E. Wolf, *Principles of optics*. Cambridge University Press, 1999.
- [31] R. E. Wagner and W. J. Tomlinson, “Coupling efficiency of optics in single-mode fiber components,” *Appl. Opt.*, vol. 21, pp. 2671–2688, Aug 1982.
- [32] Y. St-Amant, D. Gariépy, and D. Rancourt, “Intrinsic properties of the optical coupling between axisymmetric gaussian beams,” *Appl. Opt.*, vol. 43, pp. 5691–5704, Oct 2004.

BIBLIOGRAPHY

- [33] P. Nachman and A. C. Bernstein, “Scanning, spherical-mirror fabry–perot interferometer: An upper-division optics laboratory experiment,” *Am. J. Phys.*, vol. 65, no. 3, pp. 202–213, 1997.
- [34] B. N. Taylor and C. E. Kuyatt, “Guidelines for evaluating and expressing the uncertainty of nist measurement results,” *NIST Technical Note*, vol. 1297, September 1994.
- [35] N. Bobroff, “Recent advances in displacement measuring interferometry,” *Meas. Sci. Technol.*, vol. 4, no. 9, p. 907, 1993.
- [36] J. Crisp and B. Elliott, *Introduction to Fiber Optics*. Introduction to Fiber Optics Series, Elsevier Science, 2005.
- [37] H. J. Eichler and J. Eichler, *Laser*. Springer, 2010.
- [38] W. Zeller, L. Naehle, P. Fuchs, F. Gerschuetz, L. Hildebrandt, and J. Koeth, “Dfb lasers between 760 nm and 16 μm for sensing applications,” *Sensors*, vol. 10, no. 4, pp. 2492–2510, 2010.
- [39] S. L. Gilbert and W. C. Swann, “Acetylene 12c2h2 absorption reference for 1510 nm to 1540 nm wavelength calibration - srm 2517a 2001,” *NIST Spec. Publ. 260-133*, 2001.
- [40] N. Inami, Y. Takeichi, and K. Ono, “Real-time motion control and data acquisition system for scanning x-ray microscopy using programmable hardware,” *J. Phys. Conf. Ser.*, vol. 502, no. 1, p. 012011, 2014.
- [41] J. Burke, J. F. Moynihan, and K. Unterkofler, “Extraction of high resolution position information from sinusoidal encoders,” *Proc. PCIM 1999*, pp. 217–222, 1999.
- [42] M. Zech and K. Thurner, “Interferometric displacement sensor for integration into machine tools and semiconductor lithography systems,” Nov. 5 2015. European Patent Application WO2015165587 (A1).
- [43] D. Rugar, H. J. Mamin, R. Erlandsson, J. E. Stern, and B. D. Terris, “Force microscope using a fiber-optic displacement sensor,” *Rev. Sci. Instrum.*, vol. 59, no. 11, pp. 2337–2340, 1988.

BIBLIOGRAPHY

- [44] J. Ahn, J.-A. Kim, C.-S. Kang, J. W. Kim, and S. Kim, “A passive method to compensate nonlinearity in a homodyne interferometer,” *Opt. Express*, vol. 17, pp. 23299–23308, Dec 2009.
- [45] P. Gregorčič, T. Požar, and J. Možina, “Quadrature phase-shift error analysis using a homodyne laser interferometer,” *Opt. Express*, vol. 17, pp. 16322–16331, Aug 2009.
- [46] N. Bobroff, “Residual errors in laser interferometry from air turbulence and non-linearity,” *Appl. Opt.*, vol. 26, pp. 2676–2682, Jul 1987.
- [47] C. ming Wu, J. Lawall, and R. D. Deslattes, “Heterodyne interferometer with subatomic periodic nonlinearity,” *Appl. Opt.*, vol. 38, pp. 4089–4094, Jul 1999.
- [48] C. ming Wu and C. shen Su, “Nonlinearity in measurements of length by optical interferometry,” *Measurement Science and Technology*, vol. 7, no. 1, p. 62, 1996.
- [49] P. E. Ciddor, “Refractive index of air: new equations for the visible and near infrared,” *Appl. Opt.*, vol. 35, pp. 1566–1573, Mar 1996.
- [50] B. Edlén, “The refractive index of air,” *Metrologia*, vol. 2, no. 2, p. 71, 1966.
- [51] W. T. Estler, “High-accuracy displacement interferometry in air,” *Appl. Opt.*, vol. 24, pp. 808–815, Mar 1985.
- [52] P. Schellekens, G. Wilkening, F. Reinboth, M. J. Downs, K. P. Birch, and J. Spronck, “Measurements of the refractive index of air using interference refractometers,” *Metrologia*, vol. 22, no. 4, p. 279, 1986.
- [53] T. Li, “Design principles for laser interference refractometers,” *Measurement*, vol. 16, no. 3, pp. 171 – 176, 1995.
- [54] Zerodur product catalogue, SCHOTT AG.
- [55] J. Ekin, *Experimental Techniques for Low-Temperature Measurements : Cryostat Design, Material Properties and Superconductor Critical-Current Testing: Cryostat Design, Material Properties and Superconductor Critical-Current Testing*. OUP Oxford, 2006.

BIBLIOGRAPHY

- [56] H. Bosse and G. Wilkening, “Developments at ptb in nanometrology for support of the semiconductor industry,” *Meas. Sci. Technol.*, vol. 16, no. 11, p. 2155, 2005.
- [57] P. Henshaw and S. Lis, “Economic impact of a new interferometer providing improved overlay for advanced microlithography,” *Proc. ASMC 95*, pp. 81–88, 1995.
- [58] J. E. Griffith and D. A. Grigg, “Dimensional metrology with scanning probe microscopes,” *J. Appl. Phys.*, vol. 74, no. 9, pp. R83–R109, 1993.
- [59] W. Estler, K. Edmundson, G. Peggs, and D. Parker, “Large-scale metrology - an update,” *CIRP Annals - Manufacturing Technology*, vol. 51, no. 2, pp. 587 – 609, 2002.
- [60] S. Redaelli, “Dynamic alignment in particle accelerators,” *CAS - CERN Accelerator School: Course on Beam Diagnostics, Dourdan, France*, p. pp.535, 2008.
- [61] C. K. Kirkendall and A. Dandridge, “Overview of high performance fibre-optic sensing,” *J. Phys. D: Appl. Phys.*, vol. 37, no. 18, p. R197, 2004.
- [62] Zemax optical design software, Version Zemax 12 R2 SE, Radiant Zemax, LLC.
- [63] Corning SMF-28 Optical Fiber. Product Information. Corning Inc. (2002).
- [64] S. Feng and H. G. Winful, “Physical origin of the gouy phase shift,” *Opt. Lett.*, vol. 26, pp. 485–487, Apr 2001.
- [65] B. W. Hoogenboom, P. L. T. M. Frederix, J. L. Yang, S. Martin, Y. Pellmont, M. Steinacher, S. Zäch, E. Langenbach, H.-J. Heimbeck, A. Engel, and H. J. Hug, “A fabry–perot interferometer for micrometer-sized cantilevers,” *Appl. Phys. Lett.*, vol. 86, no. 7, p. 074101, 2005.
- [66] J. Kim, K. Lauer, H. Yan, Y. S. Chu, and E. Nazaretski, “Compact prototype apparatus for reducing the circle of confusion down to 40 nm for x-ray nanotomography,” *Rev. Sci. Instrum.*, vol. 84, no. 3, p. 035006, 2013.
- [67] C. C. Williams and H. K. Wickramasinghe, “Absolute optical ranging with 200-nm resolution,” *Opt. Lett.*, vol. 14, pp. 542–544, Jun 1989.

- [68] R. Dändliker, Y. Salvadé, and E. Zimmermann, “Distance measurement by multiple-wavelength interferometry,” *Journal of Optics*, vol. 29, no. 3, p. 105, 1998.
- [69] Y.-Y. Cheng and J. C. Wyant, “Two-wavelength phase shifting interferometry,” *Appl. Opt.*, vol. 23, pp. 4539–4543, Dec 1984.
- [70] P. J. de Groot, “Extending the unambiguous range of two-color interferometers,” *Appl. Opt.*, vol. 33, pp. 5948–5953, Sep 1994.
- [71] N. Schuhler, Y. Salvadé, S. Lévêque, R. Dändliker, and R. Holzwarth, “Frequency-comb-referenced two-wavelength source for absolute distance measurement,” *Opt. Lett.*, vol. 31, pp. 3101–3103, Nov 2006.
- [72] I. Coddington, W. C. Swann, L. Nenadovic, and N. R. Newbury, “Rapid and precise absolute distance measurements at long range,” *Nat. Photonics*, vol. 3, pp. 351 – 356, 2009.
- [73] J. A. Stone, A. Stejskal, and L. Howard, “Absolute interferometry with a 670-nm external cavity diode laser,” *Appl. Opt.*, vol. 38, pp. 5981–5994, Oct 1999.
- [74] T. Kinder and K.-D. Salewski, “Absolute distance interferometer with grating-stabilized tunable diode laser at 633 nm,” *J. Opt. A: Pure Appl. Opt.*, vol. 4, no. 6, p. S364, 2002.
- [75] K.-H. Bechstein and W. Fuchs, “Absolute interferometric distance measurements applying a variable synthetic wavelength,” *J. Opt.*, vol. 29, no. 3, p. 179, 1998.
- [76] K. Meiners-Hagen, R. Schödel, F. Pollinger, and A. Abou-Zeid, “Multi-wavelength interferometry for length measurements using diode lasers,” *Meas. Sci. Rev.*, vol. 9(1), pp. 16–26, 2009.
- [77] L. Hartmann, K. Meiners-Hagen, and A. Abou-Zeid, “An absolute distance interferometer with two external cavity diode lasers,” *Meas. Sci. Technol.*, vol. 19, no. 4, p. 045307, 2008.
- [78] B. L. Swinkels, N. Bhattacharya, and J. J. M. Braat, “Correcting movement errors in frequency-sweeping interferometry,” *Opt. Lett.*, vol. 30, pp. 2242–2244, Sep 2005.

BIBLIOGRAPHY

- [79] H. Kikuta, K. Iwata, and R. Nagata, “Distance measurement by the wavelength shift of laser diode light,” *Appl. Opt.*, vol. 25, pp. 2976–2980, Sep 1986.
- [80] K. Falaggis, D. P. Towers, and C. E. Towers, “Method of excess fractions with application to absolute distance metrology: theoretical analysis,” *Appl. Opt.*, vol. 50, pp. 5484–5498, Oct 2011.
- [81] P. L. M. Heydemann, “The exact fractions interferometer,” in *1976 Ultrasonics Symposium*, pp. 649–652, 1976.
- [82] J. D. Tobiasson and D. W. Sesko, “Dual laser high precision interferometer,” Nov. 6 2007. US Patent 7,292,347.
- [83] P. R. Wilkinson and J. R. Pratt, “Analytical model for low finesse, external cavity, fiber fabry–perot interferometers including multiple reflections and angular misalignment,” *Appl. Opt.*, vol. 50, pp. 4671–4680, Aug 2011.
- [84] C. Edwards, H. Margolis, G. Barwood, S. Lea, P. Gill, and W. Rowley, “High-accuracy frequency atlas of $^{13}\text{C}2\text{H}_2$ in the $1.5\ \mu\text{m}$ region,” *Appl. Phys. B*, vol. 80, no. 8, pp. 977–983, 2005.

Acknowledgement

A very special word of thanks goes to Prof. Dr. Khaled Karrai who supervised my work with enormous commitment and who gave me an insight not only into Fabry-Pérot interferometry, but also into the company attocube. I very much enjoined his open-minded personality. I want to thank Prof. Dr. Paolo Lugli for giving me the opportunity to work in the IGSSE project team within his institute for nanoelectronics and for giving me the necessary freedom to fulfill my work at attocube. I also want to thank Prof. Dr. Giuseppe Scarpa who supervised my work. He was leader of the IGSSE project 4.08, Nanoimprint and Nanotransfer, from which I received funding.

I want to thank all my colleagues at attocube. Special thanks goes to Dr. Pierre-François Braun, who supervised my work during the time at attocube. I am very thankful for the good ideas he shared with me and for all the time he invested in me. It was a great time working together with him. A special thank goes to Dr. Dirk M. Haft and Dr. Martin Zech for supporting my work and for financial support. Also I want to thank them for providing me the unique opportunity to join attocube as a full-time employee in November 2013. I would like to thank Claudio Dal Savio and Francesca Paola Quacquarelli for conducting the backlash measurements of the low-temperature actuator. The measurements were partially funded by the European Union, project Diadems. Also I would like to thank my colleague Dr. Thomas Hirschmann for fruitful discussion about interferometry.

I thank Ivan Favero for fruitful discussion about Doppler effects in our interferometer and Stephan Manus (Chair of Solid State Physics, Ludwig-Maximilians-Universität München) for developing the detector circuit of the attoFPSensor.

I want to thank my wife Marita and my parents Johanna Thurner and Martin Thurner for supporting me over all that time.

This work was financially supported by the Deutsche Forschungsgemeinschaft (DFG) through the Technische Universität München - International Graduate School of Science and Engineering (IGSSE), by the Technische Universität München - Institute

BIBLIOGRAPHY

for Advanced Studies (IAS), funded by the German Excellence Initiative (focus group Nanoimprint and Nanotransfer), and by attocube systems AG.